# Single hole dynamics in the $t$-$J$ model

Von der Fakultät für Physik der Universität Stuttgart

zur Erlangung der Würde eines

Doktors der Naturwissenschaften (Dr. rer. nat.)

genehmigte Abhandlung

Vorgelegt von

**Michael Brunner**

aus Würzburg

Hauptberichter: Prof. Dr. Alejandro Muramatsu

Mitberichter: Prof. Dr. Ulrich Weiss

Tag der mündlichen Prüfung: 31. Januar 2000

Institut für Theoretische Physik der Universität Stuttgart

2000

# Contents

# Abstract

In this work, we present results for the dynamics of a single hole in the $t$-$J$ model. These results stem from a new quantum Monte Carlo algorithm, which is capable to evaluate the single particle Green's function in imaginary time for one hole in the $t$-$J$ model at half filling. The Green's function can then be used to evaluate the lower edge of the spectrum and the quasiparticle weight directly. One can further calculate the complete spectral function and the density of states using the *Maximum Entropy* method. We have performed simulations for the $t$-$J$ model in one and two dimensions, as well as for two- and three-leg ladders.

In one dimension we find, that the results are consistent with a simple charge-spin separation *Ansatz* for the considered values of $J/t$, with a minimum of the dispersion at $k = \pi/2$. At the supersymmetric point $J/t = 2$ we observe a vanishing quasiparticle weight, consistent with analytical calculations. In two dimensions we observe a dispersion as predicted by self consistent Born approximation and series expansion. We observe flat bands around $\mathbf{k} = (\pi, 0)$ and a minimum at $\mathbf{k} = (\pi/2, \pi/2)$. The quasiparticle weight is finite in the thermodynamic limit for the considered values of $J/t$ at these two points in the Brillouin zone. The two ladder systems show a substantially different behavior. It is known, that the two-leg ladder has a spin gap, whereas the three-leg ladder has a gapless spin excitation spectrum like a one-dimensional chain. This leads to differences in the spectral function of these two quasi one-dimensional systems. The dispersion of the two-leg ladder up to the isotropic case can be well described starting from the limit of strong coupling along the rungs. We further observe a finite and large quasiparticle weight. The strong coupling limit of the three-leg ladder leads to an effective low-energy model, that is equivalent to the one-dimensional $t$-$J$ model. This effective model is consistent with our results, when the coupling along the chain is smaller than the inter-chain coupling, whereas this cannot be clarified in the isotropic case. At the supersymmetric point, our data for the three-leg ladder is consistent with a vanishing quasiparticle weight in the thermodynamic limit.

# Zusammenfassung

Seit der Entdeckung der Hochtemperatur-Supraleiter im Jahr 1986 durch G. J. Bednorz und K. A. Müller [1] erfährt das Gebiet hochkorrelierter Elektronensysteme enormes Interesse. Die einfachsten Prototypen für die Beschreibung der relevanten niederenergetischen Prozesse innerhalb der Kupferoxidebenen, die allen Hochtemperatur-Supraleitern gemein sind, sind durch das Hubbard-Modell [2, 3]

$$H_{\mathrm{Hub}} = -t \sum_{<i,j>,\sigma} c^{\dagger}_{i,\sigma} c_{j,\sigma} + U \sum_{i} n_{i,\uparrow} n_{i,\downarrow}, \tag{1}$$

und durch dessen effektives Modell im Grenzfall unendlich starker Coulomb-Abstoßung $U/t \to \infty$ [4, 5] das $t$-$J$-Modell

$$H_{t-J} = -t \sum_{<i,j>,\sigma} \tilde{c}^{\dagger}_{i,\sigma} \tilde{c}_{j,\sigma} + J \sum_{<i,j>} \left( \vec{S}_i \cdot \vec{S}_j - \frac{1}{4} \tilde{n}_i \tilde{n}_j \right) \tag{2}$$

gegeben. Hierbei erzeugt $c^{\dagger}_{i,\sigma}$ ein Elektron am Gitterplatz $i$ mit $z$-Komponente des Spins $\sigma$, wobei $n_{i,\sigma} = c^{\dagger}_{i,\sigma} c_{i,\sigma}$ der zugehörige Teilchenzahloperator ist. Weiter sind $\tilde{c}^{\dagger}_{i,\sigma} = (1 - c^{\dagger}_{i,-\sigma} c_{i,-\sigma}) c^{\dagger}_{i,\sigma}$ und $\tilde{n}_i = \sum_{\alpha} \tilde{c}^{\dagger}_{i,\alpha} \tilde{c}_{i,\alpha}$ die entsprechenden Operatoren, wenn eine Projektion auf den Hilbertraum ohne Doppelbesetzung eines Gitterplatzes erfolgt. $\vec{S}_i = (1/2) \sum_{\alpha,\beta} c^{\dagger}_{i,\alpha} \vec{\sigma}_{\alpha,\beta} c_{i,\beta}$ ist der Spinoperator am Gitterplatz $i$, die Summe $< i, j >$ wird nur über nächste Nachbarn auf einem Quadratgitter durchgeführt. Der sogenannte *three site term* $J/4 \sum_{<i,j,k>,\sigma} (c^{\dagger}_{k\sigma} n_{j-\sigma} c_{i\sigma} - c^{\dagger}_{k\sigma} c^{\dagger}_{j-\sigma} c_{j\sigma} c_{i-\sigma})$ wird in obiger Formulierung des $t$-$J$-Modells vernachlässigt, da sein Beitrag im Vergleich zum Spinaustauschterm wie die Dotierung mit Löchern $\delta$ verschwindet. Bei exakt halber Füllung ist der erste Term in Gleichung (2) irrelevant, wodurch das $t$-$J$-Modell äquivalent zum bekannten Heisenberg-

Modell [6]

$$H_{\text{Heis}} = J \sum_{<i,j>} \left( \vec{S}_i \cdot \vec{S}_j - \frac{1}{4} \right) \tag{3}$$

wird, das einen Quanten-Antiferromagneten beschreibt. Abseits halber Füllung kann das $t$-$J$-Modell als ein mit Löchern dotierter Antiferromagnet verstanden werden. F. C. Zhang und T. M. Rice [3, 7] konnten zeigen, dass das $t$-$J$-Modell an sich als korrektes effektives Modell für die Physik bei kleinen Energien dienen kann, indem sie das realistischere Mehr-Band-Emery-Modell [8] auf die relevanten niederenergetischen Freiheitsgrade reduzierten. Wird dieser Ansatz verwendet, so sind $t$ und $J$ zwei grundsätzlich frei zu wählende Parameter im Gegensatz zur Herleitung aus dem Hubbard-Modell, bei der $t$ und $J$ durch $J = 4t^2/U$ miteinander verbunden sind. Die typischen Werte für $t$ und $J$ in Materialien liegen in der Größenordnung $t \approx 500\text{meV}$ und $J \approx t/3$ [9].

Die Frage, ob der Grundzustand des repulsiven Hubbard-Modells ($U > 0$) oder des $t$-$J$-Modells Supraleitung zeigt konnte bisher noch nicht schlüssig beantwortet werden. Für Quadratgitter ist bei genau halber Füllung bekannt, dass das repulsive Hubbard-Modell und das $t$-$J$-Modell Isolatoren sind, die antiferromagnetische Ordnung aufweisen. In diesem Grenzfall zeigen die beiden einfache Modelle daher eine der auffälligsten Eigenschaften der undotierten Hochtemperatur-Supraleiter. Dieser isolierende Grundzustand ist nicht durch konventionelle Bandstrukturrechnungen erklärbar, da diese ein halbgefülltes Band und daher einen metallischen Zustand im Hubbard-Modell vorhersagen. Daraus folgt direkt, dass Viel-Teilchen-Korrelationen eine entscheidende Rolle für das Verständnis der Niederenergiephysik spielen. Materialien und Modelle, die aufgrund starker Korrelationseffekte zu Isolatoren werden, werden gemeinhin Mott-Isolatoren genannt. Teilweise wird der Begriff Mott-Isolatoren auf Systeme eingeschränkt, in denen der isolierende Zustand direkt auf die Coulombwechselwirkung zurückgeführt werden kann, wie dies im Hubbard-Modell der Fall ist. Anders als bei exakt halber Füllung, wirft das dotierte System noch eine Vielzahl von ungelösten Problemen auf. Ein natürlicher Ausgangspunkt für das Verständnis des dotierten Falls ist die Untersuchung der Dynamik des einzelnen Lochs in einem antiferromagnetischen Hintergrund. Darüber hinaus ist diese

Ein-Loch-Dynamik an sich ein wichtiger Punkt, da sie direkt durch Experimente erfassbar ist. In diesem Zusammenhang ist winkelaufgelöste Photoemmissionsspektroskopie (ARPES) (eine Übersicht kann z.B. in Ref. [10] gefunden werden) eine besonders erfolgreiche Methode. Vor kurzem wurden ARPES-Experimente für Mott-Isolatoren auf verschiedenen Topologien wie Ketten (z.B. $SrCuO_2$ [11, 12]), Leitern (z.B $Sr_{14}Cu_{24}O_{41}$ [13]) und zweidimensionale Ebenen (z.B. $Sr_2CuO_2Cl_2$ [14, 15]) durchgeführt.

In einer Dimension wurde eine Vielzahl an Resultaten, darunter die Ein-Loch-Dynamik, durch exakte Lösungen mit Hilfe des Bethe-Ansatzes sowohl für das Hubbard-Modell [16], das für $U \to \infty$ dem $t$-$J$-Modell mit $J/t \to 0$ entspricht, als auch für das supersymmetrische $t$-$J$-Modell ($J/t = 2$) [17] ermittelt. Zusätzlich wurden zahlreiche exakte Diagonalisierungen für beide Modelle durchgeführt. Bedauerlicherweise ist diese numerische Methode auf kleine Systeme beschränkt, so dass im Hubbard-Modell nur etwa 18 und im $t$-$J$-Modell nur etwa 30 Gitterplätze berücksichtigt werden können. Während die analytischen Rechnungen zeigen, dass obige Modelle zu einer Luttinger-Flüssigkeit skalieren, konnte die wichtige Konsequenz der Spin-Ladungs-Trennung in numerischen Rechnungen hingegen bisher nicht klar aufgelöst werden. Dies kann zuächst auf die kleinen Gittergrößen bei exakten Diagonalisierungen zurückgeführt werden. Quanten Monte Carlo (QMC) Simulationen des $t$-$J$-Modells [18–22], die für weit größere Gitter anwendbar sind, konnten andererseits bisher nicht zur Berechnung dynamischer Observablen genutzt werden, die jedoch für einen direkten Nachweis der Spin-Ladungstrennung nötig sind.

Trotzdem war die Vielzahl an QMC-Algorithmen (für eine Übersicht siehe z.B. den Artikel von W. von der Linden [23]), die prinzipiell in allen Dimensionen anwendbar sind eine Quelle neuer und wichtiger Ergebnisse. Die Gitter, die mit Hilfe dieser Methoden untersucht werden können sind bei weitem größer, als diejenigen der exakten Diagonalisierungen. Allerdings entstehen andere Problem durch den inhärenten statistischen Fehler aller Monte-Carlo-Methoden. Ein Hauptproblem von QMC ist das sogenannte Vorzeichenproblem (*minus-sign problem*), welches typischerweise dazu führt, dass der statistische Fehler exponentiell mit Gittergröße und inverser Temperatur wächst [24].

Abhängig vom im Einzelfall verwendenten QMC-Algorithmus gibt es zuätzlich häufig einschneidende Einschränkungen der berechenbaren Observablen. Besonders die Bestimmung von dynamischen Observablen eines Systems, wie der Spektralfunktion $A(k,\omega) = (1/\pi)\mathrm{Im}G(k,\omega)$ (hierbei ist $G(k,\omega)$ die Einteilchen-Greensfunktion) oder der Zustandsdichte $N(\omega) = \sum_k A(k,\omega)$, die bei vielen Experimenten bestimmt werden, kann in den allermeisten Fällen nicht direkt durchgeführt werden. Eine Lösung dieses Problems ist die Berechnung von Korrelationsfunktionen in imaginärer Zeit und deren analytische Fortsetzung auf reelle Frequenzen mit Hilfe einer inversen Laplace-Transformation. Diese inverse Laplacetransformation ist allerdings extrem schlecht konditioniert, falls die Daten fehlerbehaftet oder unvollständig sind. R. S. Silver *et al* [25] bemerkten zuerst, dass diese Invertierungsaufgabe einem Bild-Rekonstruktionsproblem entspricht, und daher mit Hilfe der *Maximum Entropy*-Methode [26, 27] gelöst werden kann. Mittlerweile wurde diese Methode erfolgreich verwendet, um die Spektralfunktion des halbgefüllten Hubbard-Modells aus der Greensfunktion in imaginärer Zeit zu berechnen. Die Greensfunktion wiederum wurde sowohl mit Hilfe eines Projektor- [28,29] als auch eines großkanonischen QMC-Algorithmus [30, 31] berechnet. Bei starker Coulomb-Abstoßung zeigen diese Rechnungen in zwei Dimensionen flache Bänder bei den Wellenvektoren $\mathbf{k} = (\pi, 0)$, die annähernd entartet mit $\mathbf{k} = (\pi/2, \pi/2)$ sind. Für das $t$-$J$-Modell war bisher kein Algorithmus verfügbar, der Einteilchen-Greensfunktionen in imaginärer Zeit mit der für die *Maximum Entropy*-Methode benötigten Qualität, berechnen konnte, so dass keinerlei nicht-approximativen numerischen Resultate für die komplette Spektralfunktion in großen Gittern vorliegen. Nur die Unterkante des Spektrums konnte mit Hilfe von *Green function Monte Carlo* [32, 33], bestimmt werden. Die komplette Spektralfunktion liegt nur bei kleinen Gittern aus exakten Diagonalisierungen vor. All diese Resultate zeigen eine qualitative Übereinstimmung mit den Ergebnissen des Hubbard-Modells bei starker Wechselwirkung $U$. Im $t$-$J$-Modell konnte eindeutig aufgelöst werden, dass das Minimum der Dispersion in zwei Dimensionen bei Wellenvektor $\mathbf{k} = (\pi/2, \pi/2)$ liegt.

In dieser Arbeit zeigen ich Ergebnisse für die Ein-Loch-Dynamik des $t$-$J$-Modells in einer und zwei Dimensionen, sowie für die Leiter mit zwei Wangen (Leiter oder Dop-

pelleiter) und drei Wangen (Dreifachleiter)[1]. Die Einteilchen-Greensfunktion in imaginärer Zeit wird durch einen neuentwickelten QMC-Algorithmus berechnet. Bei exakt halber Füllung ist der Algorithmus nicht mit dem Vorzeichenproblem behaftet, wodurch es möglich wird, Daten von sehr hoher Genauigkeit zu erhalten. Die Greensfunktion wird anschließend verwendet, um die Zustandsdichte und die Spektralfunktion mit Hilfe der *Maximum Entropy*-Methode zu ermitteln. Die Unterkante des Spektrums, die der Quasiteilchendispersion entspricht und das Quasiteilchengewicht dieser niedersten Anregung bei gegebenem Wellenvektor kann direkt aus den Daten der Greensfunktion ermittelt werden. Diese dynamischen Messgrößen lassen sich anschließend mit Experimenten (z.B. ARPES) vergleichen.

Die einzelnen Kapitel dieser Arbeit lassen sich wie folgt zusammenfassen:

Dieser deutschen Einleitung und Zusammenfassung schließt sich in Kapitel 1 die englischsprachige Einleitung an. Diese stimmt weitestgehend mit der deutschsprachigen überein.

In Kapitel 2 wird kurz der allgemeine Ansatzpunkt von World-Line-QMC erläutert. Weiterhin werden die Grundlagen des sogenannten Cluster- oder Loopalgorithmus [34,35] dargestellt. Es hat sich gezeigt, dass diese Methode besonders für Spinmodelle auf nichtfrustrierten Gittern ausgesprochen effizient ist [36,37]. Im Folgenden wird eine kanonische Transformation eingeführt durch die sich das $t$-$J$-Modell in einer anderen Form [38, 39]

$$\tilde{H}_{t-J} = +t \sum_{<i,j>} P_{ij} f_i^\dagger f_j + \frac{J}{2} \sum_{<i,j>} \Delta_{ij}(P_{ij} - 1), \tag{4}$$

darstellen lässt. Die Definition der Operatoren ist hierbei durch $P_{ij} = (1 + \vec{\sigma}_i \cdot \vec{\sigma}_j)/2$, $\Delta_{ij} = (1 - n_i - n_j)$ und $n_i = f_i^\dagger f_i$ gegeben. Die Transformation ist weiterhin durch die Identitäten

$$c_{i\uparrow}^\dagger = \gamma_{i,+} f_i - \gamma_{i,-} f_i^\dagger\,, \quad c_{i\downarrow}^\dagger = \sigma_{i,-}(f_i + f_i^\dagger) \tag{5}$$

definiert. Die neu eingeführten spinlosen Fermionenoperatoren erfüllen die kanonischen Vertauschungsrelationen $\{f_i^\dagger, f_j\} = \delta_{i,j}$, und $\sigma_{i,a}\,,\ a = x, y,$ oder $z$ sind die Paulimatrizen.

[1] im Englischen *two-* und *three-leg ladder*

Die Projektion auf den Hilbertraum ohne Doppelbesetzung kann durch die erhaltene und holonome Zwangsbedingung $\sum_i \gamma_{i,-} f_i^\dagger f_i = 0$ ersetzt werden. Wie aus Gleichung (4) hervorgeht, erscheinen Fermionen nun nur noch in bilinearer Form im Hamiltonoperator. Falls eine Konfiguration von Spins vorgegeben ist, kann dies dazu benutzt werden die Einteilchen-Greensfunktion in imaginärer Zeit exakt zu berechnen. Die Monte Carlo Summation über alle möglichen Spinkonfigurationen wird effizient mit Hilfe des zuvor erläuterten Loopalgorithmus durchgeführt. Die Daten der Greensfunktion können anschließend genutzt werden, um mit Hilfe der *Maximum Entropy*-Methode die Spektralfunktion und die Zustandsdichte zu berechnen. Weiterhin kann aus den Daten direkt das Quasiteilchengewicht und die untere Kante des Spektrums bestimmt werden.

In Kapitel 3 konzentrieren wir uns auf den eindimensionalen Fall. Es wird gezeigt, dass ein einfaches Hilfsteilchen- (*slave particle*) Bild [3, 40–43] sowohl die Eigenschaften der Zustandsdichte, als auch der Spektralfunktion des $t$-$J$-Modells bei halber Füllung beschreibt. Weiter wird dargestellt, dass das Quasiteilchengewicht für $J = 2t$ und Wellenvektor $k = \pi/2$ mit der Systemlänge $L$ wie $L^{-1/2}$ verschwindet. Dieses Ergebnis steht in Übereinstimmung mit analytischen Berechnungen [44]. Teile dieses Kapitels wurden bereits zur Veröffentlichung eingereicht [45].

In Kapitel 4 werden zweidimensionale Systeme betrachtet. Es wird die Zustandsdichte, die Unterkante des Spektrums, und die komplette Spektralfunktion berechnet. Diese Ergebnisse werden mit denen exakter Diagonalisierungen [46–49], variationeller QMC-Simulationen [50], *Green function* Monte Carlo [32, 33] und Reihenentwicklung um den Grenzfall der Néelordnung eines Ising-Antiferromagneten [51] verglichen. Die einzigen Ergebnisse in großen Gittern, die mit Hilfe der nicht-approximativen *Green function* Monte Carlo Methode ermittelt wurden, schließen nur die Unterkante des Spektrums ein. Für diese Größe finden wir eine gute Übereinstimmung unserer Resultate mit denen der *Green function* Monte Carlo-Simulationen und der Reihenentwicklung. Es zeigt sich, dass die Reihenentwicklungen sehr genaue Ergebnisse produzieren, falls $J/t \geq 1$. Insgesamt wird deutlich, dass die Physik für $J/t < 1$ gut mit Hilfe selbstkonsistenten Born-Approximation (SCBA) [52, 53] beschrieben werden kann, welche Fluktuationen

des Spinhintergrunds im Rahmen einer Spinwellennäherung einbezieht.
Die Ergebnisse in zwei Dimensionen können wie folgt zusammengefasst werden. Zunächst wird gezeigt, dass der Einfluss des Verhältnisses $J/t$ auf die Spektralfunktion und die Zustandsdichte im Vergleich zum eindimensionalen Fall relativ klein ist. Anschließend wird die Unterkante des Spektrums betrachtet. Es zeigen sich zunächst flache Bänder bei den Wellenvektoren $\mathbf{k} = (\pm\pi, 0)$ und $\mathbf{k} = (0, \pm\pi)$. Das Minimum der Dispersion liegt bei $\mathbf{k} = (\pm\pi/2, \pm\pi/2)$, wobei die Energiedifferenz zu $\mathbf{k} = (\pi, 0)$ ungefähr $0.2t$ beträgt und für die von uns betrachteten $J/t$ ($0.4 \leq J/t \leq 4$) innerhalb der Fehlerbalken weitgehend konstant ist. Anschließend wird die kompletten Spektralfunktion diskutiert. Man beobachtet zunächst eine Verschiebung von spektralen Gewicht zu niederen Energien wenn sich $J/t$ erhöht. Weiter wird das Vorhandensein von Stringanregungen gezeigt, indem die Anregungen knapp oberhalb des Quasiteilchenpeaks genau untersucht werden. Diese Stringanregungen skalieren wie $J^{2/3}$, genau wie die Zustände mit minimaler Energie. Dies unterstützt das einfache String-Bild für die Bewegung eines Loches in einem antiferromagnetischen Hintergrund [54–56], welches aus dem Grenzfall eines statischen Néel-Spinhintergrundes gewonnen wird. Am Ende dieses Kapitels zeigen wir numerische Ergebnisse, aus denen hervorgeht, dass das Quasiteilchengewicht in zwei Dimensionen für die von in dieser Arbeit betrachteten Werte von $0.4 \leq J/t \leq 4$ im thermodynamischen Limes endlich ist. Die qualitative Übereinstimmung unserer Ergebnisse für das Quasiteilchengewicht mit SCBA legt nahe, dass das Quasiteilchengewicht für alle $J > 0$ endlich ist, wie dies von SCBA erhalten wird.

In den folgenden beiden Kapiteln 5 und 6 werden Doppel- und Dreifachleitern untersucht. Diese stehen zwischen den ein- und zweidimensionalen Systemen, die oben diskutiert wurden. Frühere Arbeiten haben gezeigt, dass die Anzahl der Wangen (*legs*) einen überraschend starken Einfluss auf die physikalischen Eigenschaften der Leitern bei niederen Energien hat [57–59]. Bei halber Füllung ist der auffälligste Punkt das Vorhandensein einer Lücke im Spinanregungsspektrum von Leitern mit einer geraden Anzahl an Wangen, während dieser *spin gap* bei Leitern mit einer ungeraden Anzahl an Wangen inklusive der einzelnen Kette nicht auftritt. Der größte Unterschied in dieser Hinsicht

wird zwischen der Doppel- und der Dreifachleiter erwartet, die im folgenden untersucht werden. Die Auswirkungen dieses unterschiedlichen Spinanregungsspektrums auf die Ein-Loch-Dynamik ist eine interessante, aber auch schwierige Frage.

In Kapitel 5 wird zunächst die Doppelleiter behandelt. Als Ausgangspunkt unserer Überlegungen wird zu Beginn der Grenzfall starker Kopplung entlang der Holme (*rungs*) der Leiter[2]. genauer untersucht. In Anlehnung an die Literatur [60–63] zeigen wir, wie die beiden Bänder (bindend und antibindend) aus diesem Grenzfall ermittelt werden können. Wir überprüfen die analytischen Vorhersagen mit Hilfe unserer Simulationen, wobei die Kopplung quer zur Leiter ($y$-Richtung) wesentlich größer ist als entlang der Leiter ($x$-Richtung). Die Ergebnisse unserer Simulationen stimmen in diesem Limes in hervorragender Weise mit obiger Rechnung überein. Anschließend werden die Resultate im isotropen Fall, d.h die Kopplung entlang der Leiter ist gleich der Kopplung quer zur Leiter, vorgestellt. In diesem Fall ändert sich die Form des Bandes, also der Verlauf der Unterkante des Spektrums deutlich. Allerdings ist es noch möglich, diese Bänder mit Hilfe von Rechnungen zu beschreiben, die als Ausgangspunkt den Limes starker Kopplung haben [64]. Kürzlich veröffentliche Reihenentwicklungen [65], die ebenfalls um den Limes starker Kopplung durchgeführt wurden, zeigen im Parameterbereich wo sie gute Konvergenz zeigen eine sehr genaue Übereinstimmung mit unseren exakten Ergebnissen, wie dies bereits im zwei Dimensionen der Fall war. Weiterhin beobachten wir sowohl im Grenzfall starker Kopplung, als auch im isotropen Fall *shadow bands*, für die in Anhang C eine einfache Erklärung vorgestellt wird. Diese *shadow bands* können sowohl im antibindenden Band bei niederen Energien, als auch im bindenen Band bei hohen Energien beobachtet werden. Die *shadow bands* im bindenen Band haben allerdings deutlich weniger spektrales Gewicht als diejenigen im antibindenden Band. Am Ende dieses Kapitels werden numerische Ergebnisse vorgestellt, die deutlich machen, dass das Quasiteilchengewicht für die Doppelleiter endlich und darüberhinaus relativ groß ist. Dies ist weitgehend das erwartete Ergebnis, da die Doppelleiter für alle Werte von $J_y/J_x$ bei halber Füllung einen Spingap aufweist, von dem allgemein erwartet wird, dass er Spin-Ladungstrennung wie

[2]Dieser Grenzfall wird im Folgenden als *starke Kopplung* bezeichnet

im eindimensionalen $t$-$J$-Modell verhindert.

Im anschließenden Kapitel 6 wird die Dreifachleiter diskutiert. Eine der auffälligsten Eigenschaften der Dreifachleiter gegenüber der Doppelleiter ist das Fehlen eines Spingaps bei halber Füllung. Darüber hinaus besteht eine große Ähnlichkeit der niederenergetischen Spinanregungen zum eindimensionalen Fall. Zu Beginn definieren wir die drei Bänder der Dreifachleiter anhand des freien Teilchens auf drei Gitterplätzen und offenen Randbedingungen. Wie in der Doppelleiter betrachten wir weiterhin den Limes starker Kopplung entlang der Holme [66]. Es zeigt sich, dass zwei Bänder (bindend und antibindend) gerade Parität unter Spiegelung an der mittleren Wange habe, während das dritte, nichtbindende Band ungerade Parität besitzt. Störungsrechnungen um den Limes des isolierten Holms deuten an, dass die Niederenergiephysik des nichtbindenen Bandes derjenigen der einzelnen Kette ähnelt, während die beiden geraden Bänder besser durch die Anregungen einer Doppelleiter beschrieben werden. Die Ergebnisse exakter Diagonalisierungen [67] scheinen eine Fortsetzung dieses Bildes starker Kopplung bis zum isotropen Fall wie in der Doppelleiter anzudeuten. Unsere Simulation im Limes starker Kopplung unterstützen das einfache Bild des obigen Ansatzes, und zeigen dass der effektive, aus diesem Ansatz gewonnene Hamiltonoperator die niederen Anregungen gut beschreibt. Wie erwartet liegen die niedersten Anregungen im Band mit ungerader Parität, dessen Dispersion durch den eindimensionalen *slave particle*-Ansatz beschrieben wird. Die beiden symmetrischen Bänder wiederum sind dem bindenen und antibindenden Band der Doppelleiter sehr ähnlich, was besonders durch einen Vergleich mit den analytischen Quasiteilchenbändern deutlich wird, die O. P. Sushkov [68] für die Doppelleiter erhalten hat. Betrachtet man hingegen den isotropen Fall, so zeigt sich, dass hier der Ausgangspunkt starker Kopplung nicht zu einer ebenso guten Beschreibung der numerischen Ergebnisse führt wie dies in der Doppelleiter der Fall war. Auch Strukturen bei niederen Energien können nicht mehr durchgehend mit Hilfe effektiver Hamiltonoperatoren, die durch die einzelne Kette bzw. durch die Doppelleiter gegeben sind, erklährt werden. Für eine kleine Spinaustauschwechselwirkung zeigen die numerischen Ergebnisse, dass die Spektralfunktion eher dem zweidimensionalen Fall ähnelt. Zum Abschluss dieses

Kapitels wird dargestellt, dass unsere Daten für die Greensfunktion in imaginärer Zeit für $J/t = 2$ und Wellenvektor $k_x = \pi/2$ für alle drei Bänder mit einem verschwindenden Quasiteilchengewicht übereinstimmt. Die Skalierung dieses Quasiteilchengewicht $Z$ gegen die Systemlänge $L$ ist wie in einer Dimension durch $Z \sim L^{-1/2}$ gegeben.

Am Ende dieser Arbeit wird in Kapitel 7 eine kurze Zusammenfassung der Ergebnisse vorgenommen.

# Chapter 1

# Introduction

Highly correlated electrons have attracted renewed interest since the discovery of high-temperature superconductivity in 1986 by G. J. Bednorz and K. A. Müller [1]. The prototype models for the description of the relevant physics of the copper oxide planes common to all high-temperature superconductors is argued to be the Hubbard hamiltonian [2, 3]

$$H_{\mathrm{Hub}} = -t \sum_{<i,j>,\sigma} c^{\dagger}_{i,\sigma} c_{j,\sigma} + U \sum_{i} n_{i,\uparrow} n_{i,\downarrow}, \tag{1.1}$$

along with its strong coupling version in the limit $U/t \to \infty$ [4, 5], the $t$-$J$ model:

$$H_{t-J} = -t \sum_{<i,j>,\sigma} \tilde{c}^{\dagger}_{i,\sigma} \tilde{c}_{j,\sigma} + J \sum_{<i,j>} \left( \vec{S}_i \cdot \vec{S}_j - \frac{1}{4} \tilde{n}_i \tilde{n}_j \right). \tag{1.2}$$

Here $c^{\dagger}_{i,\sigma}$ creates an electron on site $i$ with $z$-component of spin $\sigma$, $n_{i,\sigma} = c^{\dagger}_{i,\sigma} c_{i,\sigma}$, and $\tilde{c}^{\dagger}_{i,\sigma} = (1 - c^{\dagger}_{i,-\sigma} c_{i,-\sigma}) c^{\dagger}_{i,\sigma}$, $\tilde{n}_i = \sum_{\alpha} \tilde{c}^{\dagger}_{i,\alpha} \tilde{c}_{i,\alpha}$ are the respective operators, projected onto the Hilbert space without double occupancy. $\vec{S}_i = (1/2) \sum_{\alpha,\beta} c^{\dagger}_{i,\alpha} \vec{\sigma}_{\alpha,\beta} c_{i,\beta}$ is the spin operator at site $i$, and the sum $< i, j >$ runs over nearest neighbors only, where the topology is taken as a square lattice. The so called three site term $J/4 \sum_{<i,j,k>,\sigma} (c^{\dagger}_{k\sigma} n_{j-\sigma} c_{i\sigma} - c^{\dagger}_{k\sigma} c^{\dagger}_{j-\sigma} c_{j\sigma} c_{i-\sigma})$ has been neglected in the above formulation of the $t$-$J$ model, since its contribution vanishes like the hole doping $\delta$ compared to the spin exchange term. At half filling, the $t$-$J$ model is equivalent to the Heisenberg model [6]

$$H_{\mathrm{Heis}} = J \sum_{<i,j>} \left( \vec{S}_i \cdot \vec{S}_j - \frac{1}{4} \right), \tag{1.3}$$

describing a quantum antiferromagnet. Away from half filling the $t$-$J$ model can be understood as an antiferromagnet doped with holes. F. C. Zhang and T. M. Rice were

able to show [3,7], that the $t$-$J$ model can serve as the correct effective model for the low-energy physics of the copper oxide planes on its own right by reducing the more realistic multi-band Emery model [8] to the relevant low-energy degrees of freedom. When using this approach, $t$ and $J$ are two basically free parameters, in contrast to the derivation from the Hubbard model, where $t$ and $J$ are connected by $J = 4t^2/U$. The typical values of $t$ and $J$ in materials are of the order $t \approx 500\text{meV}$ and $J \approx t/3$ [9].

The question, whether the ground state of the repulsive Hubbard model ($U > 0$) or of the $t$-$J$ model can be superconducting, is still unanswered. At exactly half filling, it is well known, that the repulsive Hubbard model and the $t$-$J$ model on square lattices are insulators with antiferromagnetic order. In this limit, these two simple models thus describe one major property of the undoped high-temperature superconductor materials. The insulating state at half filling cannot be explained by conventional band structure calculations, which would predict a normal metallic state in the Hubbard model at half filling. Therefore one can conclude, that the many-particle correlations play a crucial role for the understanding of the low-energy physics. Materials, that become insulating due to strong coupling effects are commonly called Mott insulators. Sometimes the term Mott insulator is restricted to systems, where the insulating state can be traced back to Coulomb interactions, as it is the case in the Hubbard model.

For the exactly half-filled case the major questions have already been addressed successfully. In contrast, there are still a large number of unresolved problems when the system is doped. One natural starting point for an understanding of the doped case is the investigation of the dynamics of a single hole in an antiferromagnetic background. Additionally this single hole dynamics is an important subject on its own, as it can be probed directly by experiments, where a particularly powerful method in this respect is angle resolved photoemission spectroscopy (ARPES) (for a review see e.g. Ref. [10]). Quite recently, ARPES experiments have been performed for Mott insulators on different topologies like chains (e.g. $SrCuO_2$ [11, 12]), two-leg ladders (e.g $Sr_{14}Cu_{24}O_{41}$ [13]), and two-dimensional plains (e.g. $Sr_2CuO_2Cl_2$ [14, 15]).

In one dimension many results, including single hole dynamics, were obtained by exact solutions from Bethe-*Ansatz* for the Hubbard model [16], which for $U \to \infty$ corresponds to the $t$-$J$ model with $J/t \to 0$, and for the supersymmetric $t$-$J$ model ($J/t = 2$) [17]. Additionally numerous exact diagonalizations which are restricted to small systems of

about 18 sites for the Hubbard model, and about 30 sites for the $t$-$J$ model, have been done for both Hamilton operators. Whereas the analytic approaches show, that the above models scale to a Luttinger liquid, one major consequence thereof, namely charge-spin separation, has not been resolved clearly in numerical calculations for all values of $J/t$. This can be traced back to the fact, that exact diagonalizations are restricted to small lattices, whereas quantum Monte Carlo (QMC) approaches for the $t$-$J$-model [18–22] were not able to obtain dynamical observables until now.

Nevertheless, the various QMC techniques (for a review see e.g. the article by W. von der Linden [23]), which are in principle applicable to any dimension, have been a big source of important results. Although the lattices that are accessible by these methods are by far bigger than those with exact diagonalization, problems can arise due to the inherent statistical errors of Monte Carlo techniques. One major problem of QMC is the so called minus-sign problem, which typically causes the statistical error to rise exponentially with inverse temperature and system size [24]. Depending on the actual QMC algorithm that is used, there are often drastic restrictions on the observables that can be addressed. Especially the calculation of dynamical quantities of a system, that are determined by many experiments, such as the the spectral function $A(k,\omega) = (1/\pi)\mathrm{Im}G(k,\omega)$ (here $G(k,\omega)$ is the single-particle Green's function) or the density of states $N(\omega) = \sum_k A(k,\omega)$, cannot be performed directly in most cases. A solution for this problem is the calculation of correlation functions in imaginary time and the analytic continuation of these data to real frequencies by an inverse Laplace transform. R. S. Silver *et al* [25] were the first to notice, that this transform, which is extremely ill posed when the data is noisy or incomplete, is equivalent to an image-reconstruction problem, and can thus be solved by the *Maximum Entropy* method [26, 27]. This method has been successfully used to evaluate the spectral function for the half filled Hubbard model from the imaginary time Green's function obtained by projector [28, 29] and grand canonical QMC [29–31] algorithms. For strong coupling these calculations in two dimensions show flat bands at wave vector $\mathbf{k} = (\pi, 0)$ nearly degenerate with $\mathbf{k} = (\pi/2, \pi/2)$. For the $t$-$J$ model, there was until now no QMC algorithm available, which was capable to produce the imaginary time data required for the full spectral function with sufficient accuracy. The only non-approximate results in two dimensions are the lower edge of the spectrum obtained by Green's function Monte Carlo [32, 33], and results obtained by exact diagonalizations

on small lattices. All these results show a qualitative agreement to the results for the Hubbard model at strong coupling $U$. For the $t$-$J$ model it was clearly resolved, that the minimum of the dispersion is at wave vector $\mathbf{k} = (\pi/2, \pi/2)$ in two dimensions.

In this work, we present results on the one- and two-dimensional $t$-$J$ model, and for the $t$-$J$ model on two- and three-leg ladders. The single-particle imaginary time Green's function is obtained by a newly developed QMC algorithm. When restricted to half filling, the algorithm is free of the minus sign problem, so that data of extremely high quality is obtained. The Green's function is used to calculate the density of states and the spectral function by the *Maximum Entropy* method. The lower edge of the spectrum, corresponding to the quasiparticle dispersion, and the quasiparticle weight of the lowest excitation can be obtained directly from the Green's function data. These dynamical quantities can then be compared to experiments such as angle resolved photoemission spectroscopy (ARPES).

In the following Chapter 2, we briefly explain the general approach of word line QMC on a discrete lattice. We further introduce the basics of the so called cluster or loop algorithm [34, 35], a method that has proven to be extremely powerful especially for spin models on non-frustrated lattices [36, 37]. Then we map the $t$-$J$ model via a canonical transformation to another form, where the hamiltonian is bilinear in fermions [38, 39]. Given a spin configuration, this can be exploited to calculate the one particle Green's function in imaginary time exactly. The Monte Carlo summation over all possible spin configurations is done with the loop algorithm. The Green's function data can be used to evaluate the spectral function and the density of states with the help of the *Maximum Entropy* method. The imaginary time Green's function can further be used to evaluate the quasiparticle weight and the lower edge of the spectrum directly.

In Chapter 3 we give results for the one-dimensional case. We show, that a simple slave particle picture [3, 40–43] is able to describe the overall features not only of the density of states but also of the spectral function of the $t$-$J$ model at half filling. We further show, that the quasiparticle weight vanishes like $L^{-1/2}$ for $J = 2t$ and $k = \pi/2$ consistent with analytic calculations [44]. Part of this discussion has been submitted for publication [45].

Chapter 4 concentrates on two-dimensional systems. We calculate the density of states, the lower edge of the spectrum and the complete spectral function and compare

our results with exact diagonalizations [46–49], variational results [50], Green's function Monte Carlo [32, 33], and series expansion around the Ising limit [51]. Up to now, exact results for large lattices by Green's function Monte Carlo only included the lower edge of the spectrum. We find good agreement with Green's function Monte Carlo and with series expansion, which prove to be extremely accurate for $J/t \geq 1$. Overall we find, that the physics for $J/t < 1$ is well described by the self-consistent Born approximation [52,53], where quantum fluctuations of the spin background are taken into account in the frame of a spin-wave approximation. The results in two dimensions can be summarized as follows. First we show, that the influence of $J/t$ on the spectral function and the density of states is rather small compared to the one-dimensional case. Next we concentrate on the lower edge of the spectrum. We observe flat bands at wave vector $\mathbf{k} = (\pm\pi, 0)$, $\mathbf{k} = (0, \pm\pi)$. The minimum of the dispersion is at $\mathbf{k} = (\pm\pi/2, \pm\pi/2)$, with the energy difference to $\mathbf{k} = (\pi, 0)$ being approximately $0.2t$ and staying constant with $J$ ($0.4 \leq J/t \leq 4$) within the error bars. When we consider the full spectral function, we observe a shift of weight to lower energies when $J/t$ increases. We show the existence of string excitations, by considering the excitations above the sharp quasiparticle peak. These string excitations scale as $J^{2/3}$, like the states with minimal energy, supporting the simple string picture for the motion of holes in an antiferromagnetic background [54–56], which is derived from the limit, where the spins form a static Néel background. Finally we present numerical evidence, that the quasiparticle weight in two dimensions remains finite for all considered values of $0.4 \leq J/t \leq 4$ in the thermodynamic limit.

The next two Chapters 5 and 6 concentrate on two- and three-leg ladders, which stand between the one- and two-dimensional systems discussed previously. The number of legs has a strong influence on the low-energy physics [57–59]. The most striking point at half filling is the absence of a spin gap in odd-leg ladders (including the single chain), whereas even-leg ladders show a fairly large gap in the spin excitations. The largest difference is seen between the two- and three-leg ladder, which are considered in this work. The effects of this substantially different spin excitation spectrum on the dynamics of a single hole, is a highly nontrivial question.

In Chapter 5 we discuss the two-leg ladder. As a starting point, we first consider the limit of strong coupling along the rungs (strong coupling limit). Following the literature [60–63], we show, how the two bands (commonly called bonding and antibonding)

can be derived starting from this limit. We check the analytical predictions by our simulations, with the coupling between the chains much larger than along the chain, i.e. $J_y \gg J_x$, and find the results expected from the above strong coupling calculation. Next we perform simulations for the isotropic case, where the bands change significantly from those at strong coupling. However we find, that analytical approaches which start from the strong coupling limit [64], are still capable to give a very good description for the low-lying excitations. Again, recent series expansion calculations around the isolated rung limit [65] prove to be extremely accurate for the parameter range where they are applicable. We observe shadow bands both in the strong coupling limit and for the isotropic case, and we give a simple picture for these structures in App. C. These shadow bands can be well observed in the antibonding band at low energies, but additionally we find evidence for shadows -with little weight- in the high energy spectrum of the bonding band. We further show, that the quasiparticle weight for two-leg ladders is finite and relatively large. This is the expected result, as two-leg ladders show a spin gap for all couplings, which is generally believed to prevent charge-spin separation as observed in the one-dimensional $t$-$J$ model.

In the following Chapter 6 we discuss the three-leg ladder. One striking property of three-leg ladders is the absence of a spin gap, and the resemblance of the low-lying spin excitations to the one-dimensional case. As a starting point, we consider again the limit of strong coupling [66], and derive the three bands in the three-leg ladder: the two bands with even parity with respect to reflection about the middle chain called bonding and antibonding, and the band with odd parity called nonbonding. The pertubative results around the isolated rung limit suggest, that the low-energy physics of the nonbonding band resembles the one of the single chain, whereas the two even parity channels behave more like the excitations of a two-leg ladder. Exact diagonalizations [67] indicate, that this strong rung coupling picture is valid up to the isotropic case. Our simulations in the strong coupling limit support the above *Ansatz* and the effective Hamilton operator obtained from it. We find, that the minimum of the dispersion is in the odd-parity band, and show, that the dispersion behaves as expected from the slave particle *Ansatz* for one dimension. The two symmetric bands resemble very much to the bonding and the antibonding band in the two-leg ladder. As opposed to the two-leg ladder the isotropic three-leg ladder does not seem to be well described by the strong coupling

limit. The structures can no longer be explained by an effective Hamiltonian given by a one-dimensional chain or a two-leg ladder. At least for weak spin exchange coupling ($J/t = 0.4$), the spectral function resembles more to the two-dimensional case. We finally demonstrate, that the data is consistent with a vanishing quasiparticle weight in the thermodynamic limit at wave vector $k_x = \pi/2$ along the chain for all three bands at the supersymmetric point $J/t = 2$.

In Chapter 7, we give a short summary and conclusions.

# Chapter 2

# Quantum Monte Carlo for a single hole in the $t$-$J$ model

## 2.1 Quantum Monte Carlo

Numerical methods applied to strongly correlated electron systems have shown an impressive development in the past years. Those developments included genuinely new algorithms, like density matrix renormalization group (DMRG) [69] for (quasi-) one-dimensional systems, as well as dramatic improvements of existing algorithms. Particularly in the field of quantum Monte Carlo algorithms, recent developments opened up new applications, that entailed new insight for exciting physical problems, which were out of reach just a few years ago.

### 2.1.1 Classical Monte Carlo

The Monte Carlo method is a way to calculate high dimensional integrals and sums. According to the central limit theorem, the error always scales like $\mathcal{O}(N^{-1/2})$. In high dimensions this is superior to analytic approaches like Simpson's rule, where the error scales like $\mathcal{O}(N^{-4/d})$ [70]. Here $N$ ($N \gg 1$) is the number of lattice points $n$ used for the approximation. In Monte Carlo, the points $n$ have to be sampled stochastically. A common approach to do so are Markov chains (i.e the probability to reach $n_{i+1}$ in the sampling is only dependent upon $n_i$). In order to obtain the correct probability distribution, it is sufficient, that the probability of transition between two elements $x, y$

of the Markov chain fulfills *detailed balance*:

$$\frac{P(x \to y)}{P(y \to x)} = \frac{W(y)}{W(x)}. \tag{2.1}$$

Here $x$ and $y$ are two possible points $n$, and $W(n)$ is the weight of these points.

Classical Monte Carlo showed up to be a very efficient tool. Many classical problems, which were not accessible by analytic or other numerical tools, like percolation or the spread of forest fires, could be easily addressed. However Monte Carlo techniques cannot be directly applied to quantum systems. For a quantum mechanical system, it is not sufficient, or more precise due to Heisenberg's uncertainitys principle, not possible to store momentum and location of each particle, but a full wave function has to be considered.

### 2.1.2 The Trotter formula

The Trotter formula [71] is given by

$$e^{A_1+A_2+\ldots+A_p} = \lim_{N\to\infty} (e^{\frac{A_1}{N}} e^{\frac{A_2}{N}} \ldots e^{\frac{A_p}{N}})^N, \tag{2.2}$$

where $A_i$ can be any quantum operator. We now use the Trotter formula to split up the partition function

$$\begin{aligned} \mathbf{Z} = \mathrm{Tr}[e^{-\beta\mathcal{H}}] = \mathrm{Tr}\left[\lim_{N\to\infty} (e^{\frac{-\beta\mathcal{H}_1}{N}} e^{\frac{-\beta\mathcal{H}_2}{N}} \ldots e^{\frac{-\beta\mathcal{H}_p}{N}})^N\right] = \\ = \mathrm{Tr}\Big[\big(\underbrace{e^{-\Delta\tau\mathcal{H}_1}}_{\tilde{U}_1}\underbrace{e^{-\Delta\tau\mathcal{H}_2}}_{\tilde{U}_2}\ldots\underbrace{e^{-\Delta\tau\mathcal{H}_p}}_{\tilde{U}_p}\big)^N\Big] + O\left(\Delta\tau^2\right). \end{aligned} \tag{2.3}$$

The error, that arises as $[H_i, H_j] \neq 0$ in general, can be systematically controlled by taking $\beta/N = \Delta\tau \ll 1$. At the end, we introduce complete sets of states to obtain

$$\begin{aligned} \mathbf{Z} &= \mathrm{Tr}\left[(\tilde{U}_1\tilde{U}_2\ldots\tilde{U}_p)^N\right] = \\ &= \sum_{i_{1,1},\ldots,i_{1,p},\ldots,i_{N,p}} \langle\, i_{1,1} \,|\, \tilde{U}_1 \,|\, i_{1,2} \,\rangle \langle\, i_{1,2} \,|\, \tilde{U}_2 \,|\, i_{1,3} \,\rangle \ldots \\ &\qquad \ldots \langle\, i_{N,p-1} \,|\, \tilde{U}_{p-1} \,|\, i_{N,p} \,\rangle \langle\, i_{N,p} \,|\, \tilde{U}_p \,|\, i_{1,1} \,\rangle . \end{aligned} \tag{2.4}$$

At a first glance, the problem has become even more complicated, as we added an additional dimension. However, if we chose $H_i$ in such a way, that each $H_i$ can be diagonalized, the problem is mapped onto a classical system.

At the end of the above procedure, the $d$-dimensional quantum system is mapped onto a $(d+1)$-dimensional classical systems. One should however notice, that in contrast to a classical system, the terms contributing to eq.(2.4) are not always positive definite. One consequence thereof is the notorious sign problem in fermionic or in frustrated spin systems.

### 2.1.3 World line Quantum Monte Carlo

In general, depending on the problem under consideration, the intermediate states in eq. (2.4) can be conveniently chosen. Often used is the insertion of states in occupation number representation. This leads to the so called world line representation of the partition function.

The second remaining question in this context is the way how one decomposes the hamiltonian. In our case (only nearest neighbor interaction), we use the so called checkerboard decomposition, where the Hamiltonian is split up in $2d$ terms, such that each term only consists of a two-site interaction (see Fig. 2.1). The partition sum is defined on a hypercubic lattice with $2dN$ partial time steps. A full time step consists of $2d$ partial

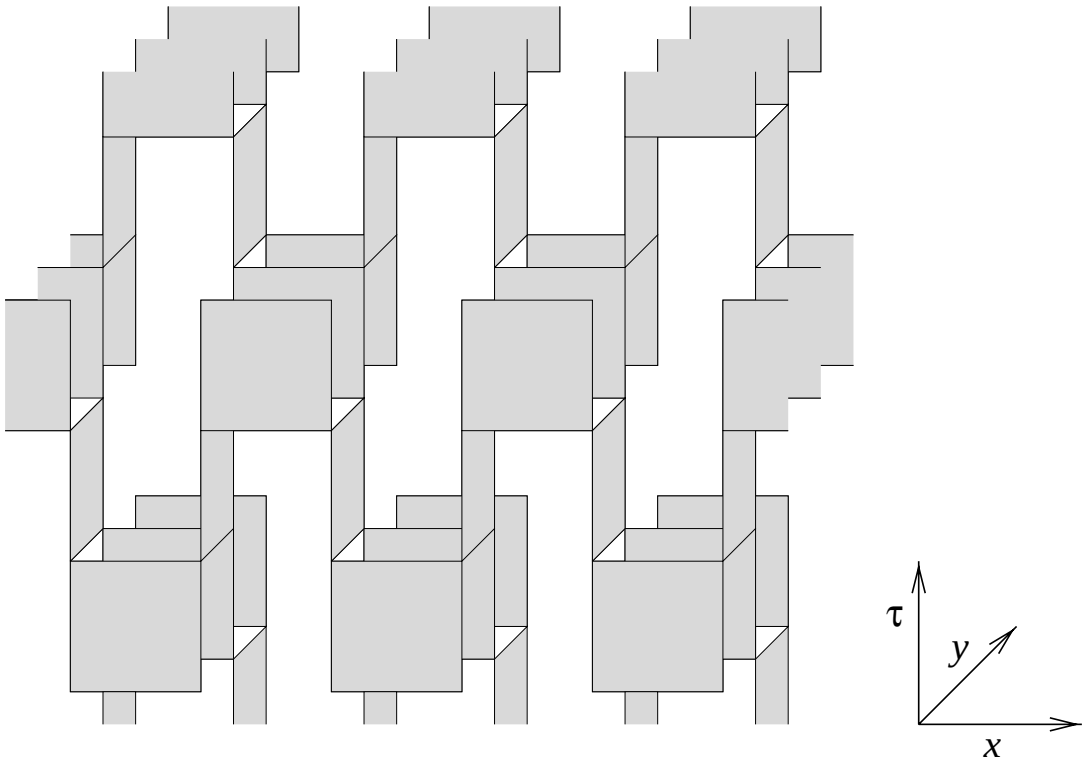


Figure 2.1: Checkerboard decomposition of a two-dimensional system with nearest neighbor interaction only.

time steps. The propagation of the global configuration is only done on connected sites of the plaquettes. In a graphical representation for two spatial dimensions the plaquettes correspond to the shaded squares in Fig. 2.1.

## 2.2 The loop algorithm for the Heisenberg model

The extension of the Swendsen-Wang algorithm [72], a Monte Carlo algorithm with global updating, to the loop algorithm [34] for quantum spin systems was a significant advance in QMC on discrete lattices. The loop algorithm has proven to be extremely efficient for systems without minus-sign problem and short range interactions [36,37]. An extension to fermionic systems such as the Hubbard model (1.1) [35] or the $t$-$J$ model (1.2) [20–22,73] has also been made, however the notorious minus-sign problem hinders simulations in more than one dimension except at half filling, where the $t$-$J$ model reduces to the Heisenberg model (2.5), or at high temperatures. Recently the loop algorithm has been improved in spin systems to work in continuous time [74] without the systematic *Trotter* error of eq.(2.4).

We now construct the loop algorithm for the Heisenberg antiferromagnet. Its Hamilton operator is given by

$$H_{\text{Heis}} = J \sum_{<i,j>} \left( \vec{S}_i \cdot \vec{S}_j - 1/4 \right), \tag{2.5}$$

where $\vec{S}_i = (1/2) \sum_{\alpha,\beta} c^\dagger_{i,\alpha} \vec{\sigma}_{\alpha,\beta} c_{i,\beta}$, $c^\dagger_{i,\beta}$ are fermion operators, and $\vec{\sigma}_{\alpha,\beta}$ are Pauli matrices. The sum runs over nearest neighbors only, and every site is occupied by a single electron. Following Sec. 2.1 the partition function is given by

$$\mathbf{Z} = \text{Tr}\Big[\exp\big(-\beta \mathcal{H}_{\text{Heis}}\big)\Big] = \text{Tr}\Big[\prod_{\tilde{p}=1}^{P} U_{\tilde{p}}\Big] = \sum_{\vec{\sigma}} \prod_{p=1}^{P} w(p,q), \tag{2.6}$$

where $\vec{\sigma}$ denotes one possible realization of the overall spin configuration, $P$ is the number of 2-site plaquettes, $U_{\tilde{p}} = \exp(-\Delta\tau \mathcal{H}^{1,2}_{\text{Heis}})$ is the transfer matrix on a single plaquette, and $w(p,q)$ is the weight on a single plaquette given a specific spin configuration $p, q$.

The transfer matrix $U_{\tilde{p}}$ is a $4 \times 4$ matrix given by

$$\underbrace{\begin{pmatrix} \uparrow\uparrow & \uparrow\downarrow & \downarrow\uparrow & \downarrow\downarrow \end{pmatrix}}_{p} \begin{pmatrix} 1 & 0 & 0 & 0 \\ 0 & \mathcal{C} & \mathcal{S} & 0 \\ 0 & \mathcal{S} & \mathcal{C} & 0 \\ 0 & 0 & 0 & 1 \end{pmatrix} \underbrace{\begin{pmatrix} \uparrow\uparrow \\ \uparrow\downarrow \\ \downarrow\uparrow \\ \downarrow\downarrow \end{pmatrix}}_{q} . \tag{2.7}$$

The abbreviations $\mathcal{C}$ and $\mathcal{S}$ in eq.(2.7) stand for $\mathcal{C} = \exp(\Delta\tau J/2)\cosh(\Delta\tau J/2)$ and $\mathcal{S} = \exp(\Delta\tau J/2)\sinh(\Delta\tau J/2)$[1]. The entries of $U_{\tilde{p}}$ equal the quantities $w(p,q)$.

In a next step we expand

$$\begin{aligned} U_{\tilde{p}} &= \alpha_1 g_1 + \alpha_2 g_2 + \alpha_3 g_3 = \\ &= \alpha_1 \begin{pmatrix} 1 & 0 & 0 & 0 \\ 0 & 1 & 0 & 0 \\ 0 & 0 & 1 & 0 \\ 0 & 0 & 0 & 1 \end{pmatrix} + \alpha_2 \begin{pmatrix} 1 & 0 & 0 & 0 \\ 0 & 0 & 1 & 0 \\ 0 & 1 & 0 & 0 \\ 0 & 0 & 0 & 1 \end{pmatrix} + \alpha_3 \begin{pmatrix} 0 & 0 & 0 & 0 \\ 0 & 1 & 1 & 0 \\ 0 & 1 & 1 & 0 \\ 0 & 0 & 0 & 0 \end{pmatrix} = \end{aligned}$$

$$= \alpha_1 \left| \quad \right| + \alpha_2 \; \diagup\!\diagdown \; + \alpha_3 \; \overline{\phantom{xx}} \; . \tag{2.8}$$

As one can see in the last line of the above equation, the matrices $g_1$, $g_2$ and $g_3$ can be identified with a graphical representation connecting the sites of the plaquette, a graph, with $\alpha_n$ being the respective weight of the graph. In the case of the Heisenberg antiferromagnet, the parameters $\alpha$ are given by

$$\alpha_1 = 1 \;,\; \alpha_2 = 0 \;,\; \alpha_3 = 1/2\big(\exp(\Delta\tau J) - 1\big) = \exp(\Delta\tau J/2)\sinh(\Delta\tau J/2). \tag{2.9}$$

The second graph corresponding to $\alpha_2$ has no weight and should therefore not be considered further. In the following we use the parameters $\alpha_n$ to assign to each graph $g_n$ a probability $P(g_n|p,q) = \big(\alpha_n/w(p,q)\big)\delta(g_n,p,q)$ given a spin configuration $(p,q)$. Here $\delta(g_n,p,q) = 1$, if the corresponding entry in the matrices of eq. (2.8) are 1, and

[1] In principle it is $\mathcal{S} = -\exp(\Delta\tau J/2)\sinh(\Delta\tau J/2)$, however one can show, that the number of these terms in a nonfrustrated Heisenberg antiferromagnet is always even [20,70], leading to a positive definite global weight.

$\delta(g_n, p, q) = 0$ when the entries are 0. One obtains:

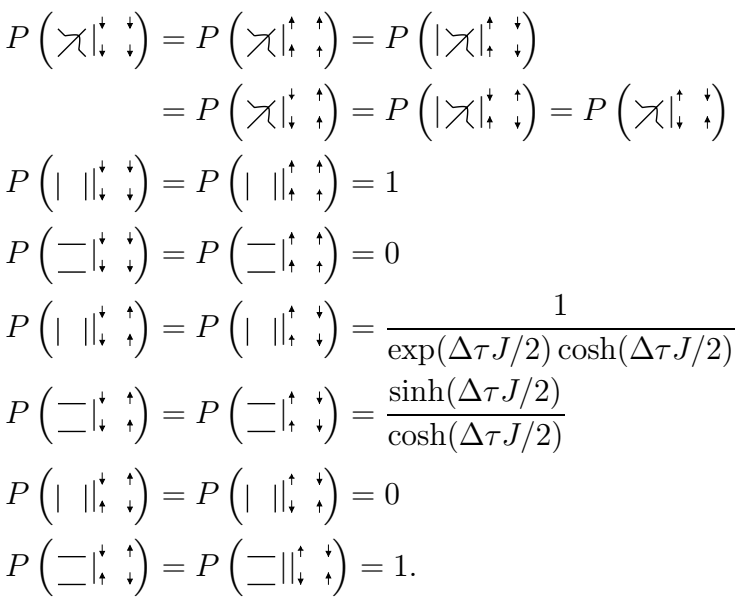

$$
\begin{aligned}
P\left(\times|^{\downarrow\ \downarrow}_{\downarrow\ \downarrow}\right) &= P\left(\times|^{\uparrow\ \uparrow}_{\downarrow\ \uparrow}\right) = P\left(|\times|^{\uparrow\ \downarrow}_{\uparrow\ \downarrow}\right) \\
&= P\left(\times|^{\downarrow\ \uparrow}_{\downarrow\ \uparrow}\right) = P\left(|\times|^{\downarrow\ \uparrow}_{\uparrow\ \downarrow}\right) = P\left(\times|^{\uparrow\ \downarrow}_{\downarrow\ \uparrow}\right) = 0 \\
P\left(|\ \ |^{\downarrow\ \downarrow}_{\downarrow\ \downarrow}\right) &= P\left(|\ \ |^{\uparrow\ \uparrow}_{\downarrow\ \uparrow}\right) = 1 \\
P\left(=|^{\downarrow\ \downarrow}_{\downarrow\ \downarrow}\right) &= P\left(=|^{\uparrow\ \uparrow}_{\downarrow\ \uparrow}\right) = 0 \\
P\left(|\ \ |^{\downarrow\ \uparrow}_{\downarrow\ \uparrow}\right) &= P\left(|\ \ |^{\uparrow\ \downarrow}_{\downarrow\ \uparrow}\right) = \frac{1}{\exp(\Delta\tau J/2)\cosh(\Delta\tau J/2)} \\
P\left(=|^{\downarrow\ \uparrow}_{\downarrow\ \uparrow}\right) &= P\left(=|^{\uparrow\ \downarrow}_{\downarrow\ \uparrow}\right) = \frac{\sinh(\Delta\tau J/2)}{\cosh(\Delta\tau J/2)} \\
P\left(|\ \ |^{\downarrow\ \uparrow}_{\uparrow\ \downarrow}\right) &= P\left(|\ \ |^{\uparrow\ \downarrow}_{\downarrow\ \uparrow}\right) = 0 \\
P\left(=|^{\downarrow\ \uparrow}_{\uparrow\ \downarrow}\right) &= P\left(=||^{\uparrow\ \downarrow}_{\downarrow\ \uparrow}\right) = 1.
\end{aligned}
\tag{2.10}
$$

A closer look at the properties of the graphs reveals, that on each plaquette allowed graphs with $P\big(g|(p,q)\big) \neq 0$ connect possible spin configurations on the plaquette. Whenever a line of a graph is flipped ($\uparrow \longrightarrow \downarrow$ and $\downarrow \longrightarrow \uparrow$) the resulting configuration is an allowed one. If one flips a closed line (*loop*) on the overall system, the resulting configuration is again an allowed one. An example of this procedure can be seen in Fig. 2.2.

Now the exact proceeding for a Monte Carlo update in a loop algorithm can be given:

1. Start with an arbitrary spin configuration.
2. Draw a graph on each plaquette according to the probabilities in eq. (2.10).
3. Connect all graphs and form loops.
4. Flip all loops with probability 1/2 to obtain a new configuration.
5. Calculate observables.
6. Go back to Step 2.

The only two conditions, that have to be proven is the ergodicity of the algorithm, and that the algorithm fulfills detailed balance.

To show ergodicity, we assume, that the starting configuration is given by a classical Ising state, every site has opposite spin direction to its neighbor. When the system is in this configuration, a single step can bring each plaquette to any other configuration

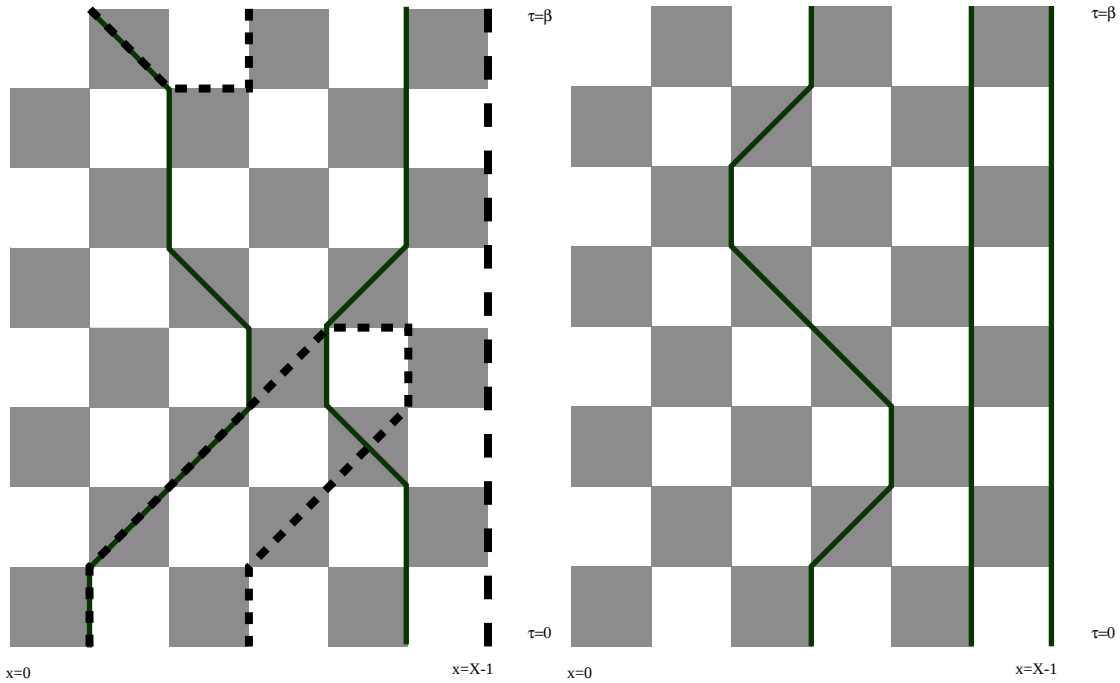


(a) Word line configuration before the loops (broken lines) are flipped

(b) Worldling configuration after flipping the loops

Figure 2.2: Effect of flipping loops on the worldling configuration. It can be seen, that the configuration changes completely, above all the number of world lines has increased by one. Here the full lines represent world-lines corresponding to spin ↑, and the broken lines represent the loops. The world-lines corresponding to spin ↓ are not shown explicitly and thus correspond to the empty sites.

and therefore the complete system. If we assume for the moment, that the algorithm fulfills detailed balance (2.1), every configuration can evolve to the Ising configuration in a single step. Therefore the system can in principle reach any state in only two steps, and is therefore ergodic.

The second requirement to check is detailed balance. This is done as follows:

$$\frac{W(y)}{W(x)} \equiv \frac{P(x \to y)}{P(y \to x)} = \frac{P(G(x \leftrightarrow y)|x)}{P(G(x \leftrightarrow y)|y)} = \frac{\prod_{\tilde{p}} \frac{\alpha_{\tilde{p}}}{w(q(x),r(x))}}{\prod_{\tilde{p}} \frac{\alpha_{\tilde{p}}}{w(q(y),r(y))}} = \frac{W(y)}{W(x)}, \tag{2.11}$$

where $\tilde{p}$ are all plaquettes that belong to the relevant graph connecting the two configurations $x$ and $y$. The probability $P(G(x \leftrightarrow y)|x)$ is given by eq.(2.10), where $G(x \leftrightarrow y)$ corresponds to the graph connecting the two configurations $x$ and $y$.

## 2.3 A single hole in the $t$-$J$ model

In this section we will develop the algorithm on which the numerical results in this work are based on. It allows the calculation of one-particle Green's functions in imaginary time for the $t$-$J$ model at half filling. An extension of the algorithm to higher doping will be published elsewhere [75].

### 2.3.1 The mapping to a bilinear form

Our starting point is the $t$-$J$ model, with next-neighbor interaction only,

$$H_{t-J} = -t \sum_{<i,j>,\sigma} \tilde{c}^{\dagger}_{i,\sigma} \tilde{c}_{j,\sigma} + J \sum_{<i,j>} \left( \vec{S}_i \cdot \vec{S}_j - \frac{1}{4} \tilde{n}_i \tilde{n}_j \right). \tag{2.12}$$

Here $\tilde{c}^{\dagger}_{i,\sigma}$ are projected fermion operators $\tilde{c}^{\dagger}_{i,\sigma} = (1 - c^{\dagger}_{i,-\sigma} c_{i,-\sigma}) c^{\dagger}_{i,\sigma}$ , $\tilde{n}_i = \sum_{\alpha} \tilde{c}^{\dagger}_{i,\alpha} \tilde{c}_{i,\alpha}$, $\vec{S}_i = (1/2) \sum_{\alpha,\beta} c^{\dagger}_{i,\alpha} \vec{\sigma}_{\alpha,\beta} c_{i,\beta}$, and the sum runs over nearest neighbors. After a canonical transformation this model is cast into the form [38, 39]:

$$\tilde{H}_{t-J} = +t \sum_{<i,j>} P_{ij} f^{\dagger}_i f_j + \frac{J}{2} \sum_{<i,j>} \Delta_{ij} (P_{ij} - 1), \tag{2.13}$$

where $P_{ij} = (1 + \vec{\sigma}_i \cdot \vec{\sigma}_j)/2$, $\Delta_{ij} = (1 - n_i - n_j)$ and $n_i = f^{\dagger}_i f_i$. In this mapping, one uses the following identities for the standard creation ($c^{\dagger}_{i,\sigma}$) and annihilation ($c_{i,\sigma}$) operators

$$c^{\dagger}_{i\uparrow} = \gamma_{i,+} f_i - \gamma_{i,-} f^{\dagger}_i \,, \quad c^{\dagger}_{i\downarrow} = \sigma_{i,-} (f_i + f^{\dagger}_i) \,, \tag{2.14}$$

where $\gamma_{i,\pm} = (1 \pm \sigma_{i,z})/2$ and $\sigma_{i,\pm} = (\sigma_{i,x} \pm i\sigma_{i,y})/2$. The spinless fermion operators fulfill the canonical anticommutation relations $\{f^{\dagger}_i, f_j\} = \delta_{i,j}$, and $\sigma_{i,a}$ , $a = x, y,$ or $z$ are the Pauli matrices. The constraint to avoid doubly occupied states transforms to the conserved and holonomic constraint $\sum_i \gamma_{i,-} f^{\dagger}_i f_i = 0$. This constraint simply means, that a spinless fermion and a pseudospin $\downarrow$ are not allowed to be on the same site.

The kinetic and potential terms of eqs (2.12) and (2.13) lead to exactly the same absolute weights for a world line algorithm in the physical subspace with no double occupancy. To construct a loop algorithm for the Hamiltonian (2.13) [20, 22] one can simply use the weights of the $t$-$J$ model in the common representation (2.12). At half filling, there is no spinless fermion present, and thus the weights for the graphs in a loop algorithm reduce to those of the Heisenberg model, which are given in eq.(2.10).

### 2.3.2 The evaluation of the Green's function

We are interested in the propagation of a single hole in imaginary time. This quantity is described by the single-particle Green's function in imaginary time, given by

$$G_\uparrow(i-j,\tau) = \langle T\tilde{c}_{i,\uparrow}(\tau)\tilde{c}^\dagger_{j,\uparrow}\rangle = \langle T f^\dagger_i(\tau) f_j\rangle \tag{2.15}$$

where $T$ corresponds to the time ordering operator. Next we perform a Trotter decomposition and insert complete sets of spin states in a basis where $\sigma_z$ is diagonal (see eq.(2.4)). Then the quantity above is given by

$$\begin{aligned} -G(i-j,-\tau) &= \frac{\sum_{\sigma_1}\langle v|\otimes\langle\sigma_1|e^{-(\beta-\tau)\tilde{H}_{t-J}} f_j e^{-\tau\tilde{H}_{t-J}} f_i^\dagger|\sigma_1\rangle\otimes|v\rangle}{\sum_{\sigma_1}\langle\sigma_1|e^{-\beta\tilde{H}_{t-J}}|\sigma_1\rangle} = \\ &= \sum_{\vec{\sigma}} P(\vec{\sigma}) \times \frac{\langle v|f_j e^{-\Delta\tau\tilde{H}(\sigma_n,\sigma_{n-1})}\dots e^{-\Delta\tau\tilde{H}(\sigma_2,\sigma_1)} f_i^\dagger|v\rangle}{\langle\sigma_n|e^{-\Delta\tau\tilde{H}_{t-J}}|\sigma_{n-1}\rangle\dots\langle\sigma_2 e^{-\Delta\tau\tilde{H}_{t-J}}|\sigma_1\rangle} + \mathcal{O}(\Delta\tau^2) = \\ &= \sum_{\vec{\sigma}} P(\vec{\sigma}) G(i,j,\tau,\vec{\sigma}) + \mathcal{O}(\Delta\tau^2). \end{aligned} \tag{2.16}$$

Here $m\Delta\tau = \beta$, $n\Delta\tau = \tau$, $\Delta\tau t \ll 1$ and $\exp\big(-\Delta\tau\tilde{H}(\sigma_1,\sigma_2)\big)$ is the evolution operator for the holes, given the spin configuration $(\sigma_1,\sigma_2)$. In the case of single hole dynamics $|v\rangle$ is the vacuum state for holes, and $P(\vec{\sigma})$ is the probability distribution of a Heisenberg antiferromagnet for the configuration $\vec{\sigma}$, where $\vec{\sigma}$ is a vector containing all intermediate states $(\sigma_1,\dots\sigma_n,\dots\sigma_m,\sigma_1)$. The sum over spins is performed in a very efficient way by using a world-line loop-algorithm with discretized imaginary time (see Sec. 2.2). The systematic error due to the discretization of imaginary time vanishes as $\Delta\tau^2$ [76], as the propagators in $P(\vec{\sigma})$ and the observable $G(x,-\tau)$ are real numbers at the same time. As the evolution operator for the holes is a bilinear form in the fermion operators, $G(x,\tau,\vec{\sigma})$ can be calculated exactly. $G(x,\tau,\vec{\sigma})$ contains a sum over all possible fermion paths between $(i,0)$ and $(j,\tau)$, where $i-j=x$. This stands in contrast to the worm approach [77], or to the approach where the imaginary time Green's function is measured directly from the constructed loops [78], where the fermion paths are only sampled stochastically. The numerical effort to calculate $G(x,\tau,\vec{\sigma})\,\forall\, x,\tau$ scales as $N\tau$, where N is the number of lattice points in real space.

With the representation (2.13), the propagation of down spin electrons cannot be easily considered, since the operators $\sigma_{i,\pm}$ cut world-lines. This is certainly not a problem

for finite-size systems, where no spontaneous symmetry breaking can occur. Therefore the SU(2) symmetry is conserved, and it is sufficient to concentrate on electrons with spin $\uparrow$. As $P(\vec{\sigma})$ is the probability distribution for the quantum antiferromagnet, and is therefore positive definite, the algorithm does not suffer from sign problems on bipartite lattices and next-neighbor interactions in any dimension. An extension to next-nearest (or higher) neighbor interaction is straightforward, as long as the resulting spin model is not frustrated.

### 2.3.3 The calculation of $G(x, \tau, \vec{\sigma})$

We now address the calculation of $G(x, \tau, \vec{\sigma})$. The Green's function, given a spin configuration, can be written as

$$G(x, \tau + \Delta\tau_1, \vec{\sigma}) = \sum_i G(i, \tau, \vec{\sigma}) \frac{\langle v| f_x e^{-\Delta\tau \tilde{H}(\sigma_n, \sigma_{n-1})} f_i^\dagger |v\rangle}{\langle \sigma_n | e^{-\Delta\tau \tilde{H}_{t-J}} | \sigma_{n-1} \rangle}. \tag{2.17}$$

We first consider only a single propagation step, denoted by $\Delta\tau_1$, such that $x$ and $i$ can only be connected by $e^{-\Delta\tau \tilde{H}(\sigma_n, \sigma_{n-1})}$ if they are on the same plaquette, such that all terms, where $x$ and $i$ belong to different plaquettes are 0. The fraction on the right hand side of eq.(2.17) can be expanded in a product over all plaquettes of this time step, and it can be easily seen, that all terms in the nominator and denominator are equal, except the term, that belongs to the plaquette of site $x$. We arrive at

$$\begin{aligned} G(x, \tau + \Delta\tau_1, \vec{\sigma}) = G(x, \tau, \vec{\sigma}) \frac{\langle v| f_x e^{-\Delta\tau \tilde{H}(\sigma_n, \sigma_{n-1})} f_x^\dagger |v\rangle}{\langle \sigma_n | e^{-\Delta\tau \tilde{H}_{t-J}} | \sigma_{n-1} \rangle} + \\ + G(x + \vec{\delta}, \tau, \vec{\sigma}) \frac{\langle v| f_x e^{-\Delta\tau \tilde{H}(\sigma_n, \sigma_{n-1})} f_{x+\vec{\delta}}^\dagger |v\rangle}{\langle \sigma_n | e^{-\Delta\tau \tilde{H}_{t-J}} | \sigma_{n-1} \rangle}, \end{aligned} \tag{2.18}$$

where $\vec{\delta}$ is a vector connecting $x$ to its neighbor site on the plaquette. As can be seen from eq.(2.18), the Green's function at imaginary time $\tau + \Delta\tau_1$ can be derived from the Green's function at imaginary time $\tau$. By a repeated application of eq.(2.18) we can thus calculate the imaginary time Green's function for any imaginary time. At $\tau = 0$, the Green's function, given a spin configuration, is set to $G(x, 0, \vec{\sigma}) = \delta(x - x_0)$, unless the constraint is violated. In this case we set $G(x, 0, \vec{\sigma}) = 0$. The value for the *real* equal time Green's function is given by

$$G(x, x, 0) = \sum_{\vec{\sigma}} P(\vec{\sigma}) G(x, x, 0, \vec{\sigma}) = 1/2\delta(x - x_0), \tag{2.19}$$

as the probability to have a pseudospin $\uparrow$ at site $x_0$ is equal to that of having pseudospin $\downarrow$. This is in contrast to models of unconstrained fermions like the Hubbard model, where $G(x, x, 0) = \delta(x - x_0)$. The factor of two in the weight can be led back to the missing of the upper Hubbard band in the $t$-$J$ model.

The above considerations lead to the conclusion, that the propagation of the Green's function can be calculated by propagating the relevant contributions on a single plaquette, leading to the four different weights, when respecting the constraint, that are given in Table 2.1. The relevant parts of the Green's function are $G(x, \tau, \vec{\sigma})$ and $G(x + \vec{\delta}, \tau, \vec{\sigma})$, whereas the fractions in eq. (2.18) correspond to the weights in Table 2.1.

| $x \to x$ | $x + \vec{\delta} \to x$ | spin configuration |
|---|---|---|
| 0 | 0 | $\uparrow\uparrow$ / $\uparrow\uparrow$ |
| $\cosh(\Delta\tau t)$ | $-\sinh(\Delta\tau t)$ | $\downarrow\downarrow$ / $\downarrow\downarrow$ |
| $\frac{\cosh(\Delta\tau t)}{\exp(\Delta\tau J/2)\cosh(\Delta\tau J/2)}$ | 0 | $\uparrow\downarrow \quad \downarrow\uparrow$ / $\uparrow\downarrow, \downarrow\uparrow$ |
| 0 | $\frac{\sinh(\Delta\tau t)}{\exp(\Delta\tau J/2)\sinh(\Delta\tau J/2)}$ | $\downarrow\uparrow \quad \uparrow\downarrow$ / $\uparrow\downarrow, \downarrow\uparrow$ |

Table 2.1: Contributions for the propagation of the hole in one time step.

The numerical effort to propagate all Green's functions $G(x, \tau, \sigma)$ scales linearly with system size. Therefore the method is more efficient for large systems than for example the projector algorithms for the Hubbard model (see e.g. Ref. [29,79]), which scales with the system size cubed.

## 2.4 The *Maximum Entropy* method

Actually until now, no QMC algorithm such as the loop algorithm or related ones as the one presented in Sec. 2.3 are able to give real time or real frequency results directly, which are of experimental interest. Instead an analytic continuation of the data in imaginary time to real frequence has to be performed. Only for a few rather simple model Hamiltonians a direct computation of real time quantities has been successfully performed [80–82]. At a first glance, the analytic continuation is not of a serious problem, as the Green's function in imaginary time is connected to the spectral function at $T = 0$

$$A(k, \omega) = \sum_{f,\sigma} \left| \langle\, f, N-1 \,|\, c_{k,\sigma} \,|\, 0, N \,\rangle \right|^2 \delta\left(\omega - E_0^N + E_f^{N-1}\right), \tag{2.20}$$

and to the density of states

$$N(\omega) = \sum_k A(k,\omega) \tag{2.21}$$

via the spectral theorem

$$G(k,\tau) = \int_{-\infty}^{\infty} d\omega \frac{\exp(-\tau\omega)}{\pi} A(k,\omega), \tag{2.22}$$

and

$$G(x=0,\tau) = \int_{-\infty}^{\infty} d\omega \frac{\exp(-\tau\omega)}{\pi} N(\omega), \tag{2.23}$$

respectively. At finite temperatures the spectral function is expressed as

$$A(k,\omega) = \frac{1}{\mathbf{Z}} \sum_{i,f,\sigma} \big|\langle\, f, N-1 \,|\, c_{k,\sigma} \,|\, i, N \,\rangle\big|^2 \delta\big(\omega - E_i^N + E_f^{N-1}\big) \exp(-\beta E_i^N), \tag{2.24}$$

and the spectral theorem goes over to

$$G(k,\tau) = \int_{-\infty}^{\infty} d\omega \frac{\exp(-\tau\omega)}{\pi\big(1+\exp(-\beta\omega)\big)} A(k,\omega), \tag{2.25}$$

and

$$G(x=0,\tau) = \int_{-\infty}^{\infty} d\omega \frac{\exp(-\tau\omega)}{\pi\big(1+\exp(-\beta\omega)\big)} N(\omega), \tag{2.26}$$

respectively. Here $|\, f, N \,\rangle$ and $|\, f, N-1 \,\rangle$ represent states at half filling and at doping with one hole respectively, and $E_f^N$, $E_f^{N-1}$ are the corresponding energies. The ground state is given by $|\, 0, N \,\rangle$.

However, the QMC data on the left hand side ($G(k,\tau)$) is not exact nor continuous, but has an intrinsic statistical error, leaving an extremely ill defined problem. The number of solutions for $A(k,\omega)$ given $G(k,\tau)$ is infinite.

One possibility to solve this problem is the *Maximum Entropy* method [26, 27]. The goal is to maximize the conditional probability $P(A|G)$ of the spectral function $A(k,\omega)$, given the Green's function $G(k,\tau)$. By using Bayes theorem (see e.g Ref. [83]), this is put into the form

$$P(A|G) = \frac{P(G|A)P(A)}{P(G)}. \tag{2.27}$$

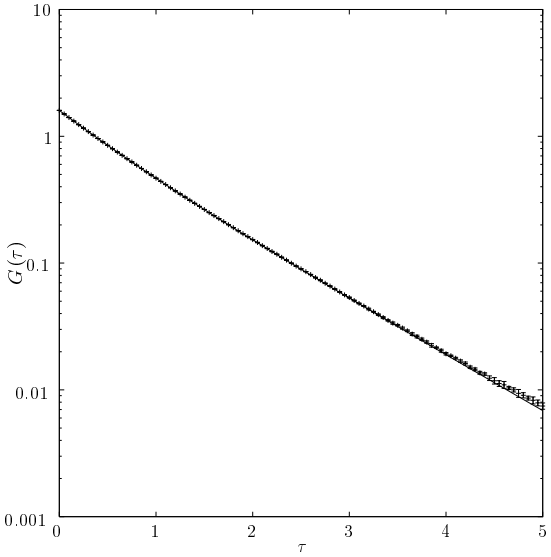


(a) Data with relatively small errors

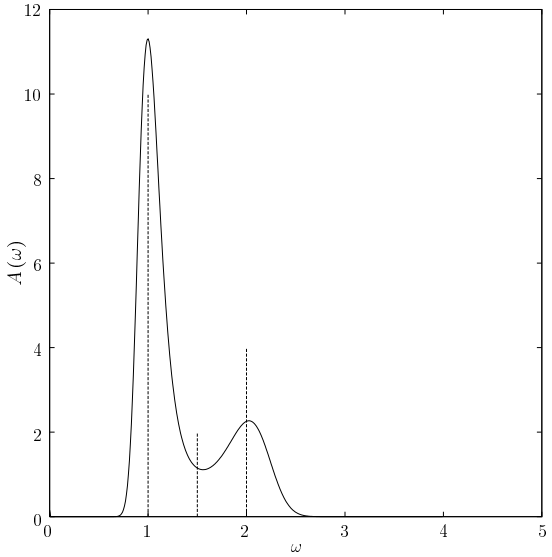


(b) *Maximum Entropy* result with data given by (a)

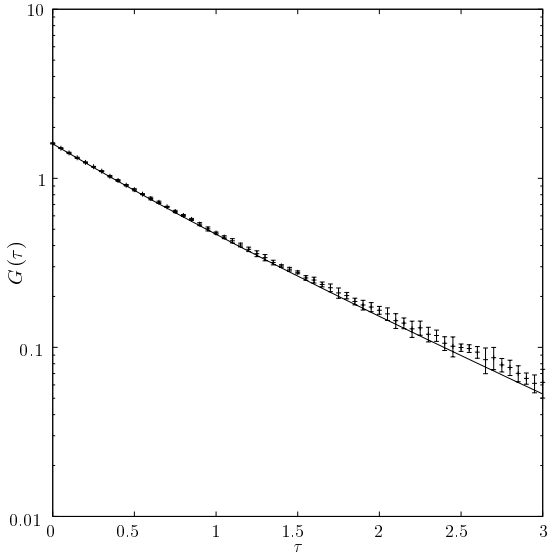


(c) Data with relatively big errors

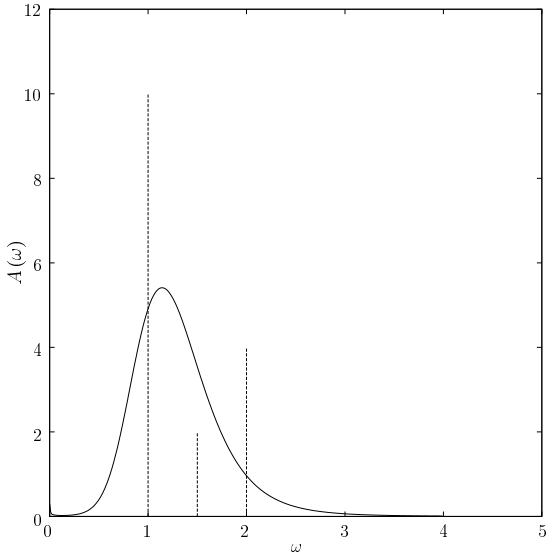


(d) *Maximum Entropy* result with data given by (c)

Figure 2.3: Results of the *Maximum Entropy* method for different data qualities. The three original $\delta$-Peaks are at $\omega_1 = 1$, $\omega_2 = 2$, and $\omega_3 = 1.5$ have weights $\alpha_1 = 1$, $\alpha_2 = 0.4$, and $\alpha_3 = 0.2$ and are indicated in the results.

The probability $P(G)$ is known, the probability $P(A)$ can be used to take into account prior knowledge (e.g $A(k,\omega) \geq 0$) and $P(G|A)$ is maximized. The word *Maximum Entropy* comes from the entropic regularization, given by

$$P(A) \sim \exp\Big[\alpha \int d\omega \Big(A(\omega) \ln\big[A(\omega)/m(\omega)\big] - A(\omega) + m(\omega)\Big)\Big], \tag{2.28}$$

where $m(\omega)$ is a function called the default model, and $\alpha$ is chosen by maximimizing

$P(\alpha|G)$. In the absence of any information given by $G$, the *Maximum Entropy* method gives the default model as the most probable answer.

In this work, we use an existing *Maximum Entropy* code of Fakher F. Assaad, which is applied without major changes.

The typical QMC data $G(k,\tau)$, that were used as input for *Maximum Entropy* are as follows:

- About 100-1000 independent QMC runs are performed to obtain 100-1000 independent samples for each $G(k,\tau)$.
- The covariance matrix in the *Maximum Entropy* analysis is considered.
- The default model of the *Maximum Entropy* analysis is flat.
- In order to check the reliability of our *Maximum Entropy* results, we add white noise to the data in a basis, where the covariance matrix is diagonal.

We now give an example of the reliability and resolution of the *Maximum Entropy* method. We take a function $f(\omega) = \pi\big(\alpha_1\delta(\omega-\omega_1)+\alpha_2\delta(\omega-\omega_2)+\alpha_3\delta(\omega-\omega_3)\big)$, which consists of three $\delta$-peaks. With the help of eq. (2.22) we obtain $G(\tau) = \alpha_1\exp(-\tau\omega_1) + \alpha_2\exp(-\tau\omega_2)+\alpha_3\exp(-\tau\omega_3)$. To this data we add white noise and then use it as an input of our *Maximum Entropy* algorithm. An example for this is given in Fig. 2.3. Obviously the *Maximum Entropy* method has a tendency to broaden all peaks. Moreover one needs very good input data, to separate two peaks which are not far apart. The small $\delta$-peak in the middle has not been resolved even by the very good data of Fig. 2.3.a. The resolution of two peaks, which are nearby and which are of small weight is an extremely difficult task with *Maximum Entropy*.

# Chapter 3

# A single hole in the one-dimensional $t$-$J$ model

## 3.1 Charge-spin separation in one dimension

One-dimensional electron systems show special and exciting properties. In the presence of gapless excitations these systems form non-Fermi liquids called Luttinger liquids [84]. The key features of these Luttinger liquids are anomalous dimensions of operators producing correlation functions with non-universal power laws, and charge-spin separation [43, 85]. Charge-spin separation leads to the factorization of an electron into charged spinless and neutral, spin 1/2 excitations (see Fig. 3.1). This feature leads to the absence of quasiparticle excitations.

A simple description of the low-energy physics of a system which shows charge-spin separation are free holons and spinons described by [3, 40, 41]

$$H_{CS} = -\frac{t_h}{2} \sum_{<i,j>} h_i^\dagger h_j - \frac{J_s}{2} \sum_{<i,j>} s_{i,\sigma}^\dagger s_{j,\sigma}. \tag{3.1}$$

Here the electron operator $c_{i,\sigma}$ is given by the product of a holon ($h_i$) and a spinon ($s_{i,\sigma}$) operator, $c_{i\sigma} = s_{i,\sigma} h_i^\dagger$, the holon being a boson and the spinon a spin-1/2 fermion. As a consequence of the above charge spin separation *Ansatz* (CSSA), the dispersion relations of the free holons and spinons are given by $\epsilon_h = -t_h \cos q_h$ and $\epsilon_s = -J_s \cos q_s$, respectively, whereas the energy of the hole is $E(k) = \epsilon_h - \epsilon_s$ and by momentum conservation $k = q_h - q_s$. We take $t_h$ and $J_s$ as two free parameters in contrast to a mean-field approximation, where they have to be calculated self-consistently. The spectral function is

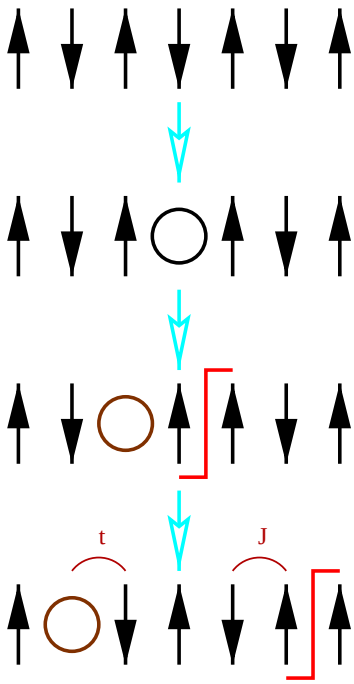


Figure 3.1: Charge-spin separation in one dimension. Starting from the Néel state (first line) one removes one electron. This hole splits up into two particles (third line), a holon (circle) and a spinon (kink) moving independently with $t$ and $J$ respectively (bottom line)

then given by a convolution of the spinon and holon Green's functions. The lowest attainable energy $(-t_h)$ and highest one $(t_h + J_s)$ define the bandwidth of the hole, $2t_h + J_s$. The support of the spectral function is given in Fig. 3.2. Under support we denote the region in energy and momentum where $A(k,\omega)$ is defined. Outside this region, which is enclosed in Fig. 3.2 $A(k,\omega) \equiv 0$. In the following we elucidate whether we can find a sign of charge-spin separation in our numerical results for the $t$-$J$ model. For this purpose, we first check, if the overall density of states scales like $4t + J$, as predicted by the CSSA. We further investigate, whether the support given by CSSA corresponds to the actual spectral function. Furthermore, we search for a splitting of the low-energy peaks predicted in the Luttinger liquid theory [43, 86, 87] and if we can see any numerical evidence for nonanalyticities, which scale with $t$ inside the support.

We further calculate the quasiparticle weight for lattices up to $L = 128$ at the minimum of the spectrum, which is at $k = \pi/2$, and obtain the quasiparticle weight in the thermodynamic limit by a finite-size scaling, which according to Luttinger liquid theory, should vanish.

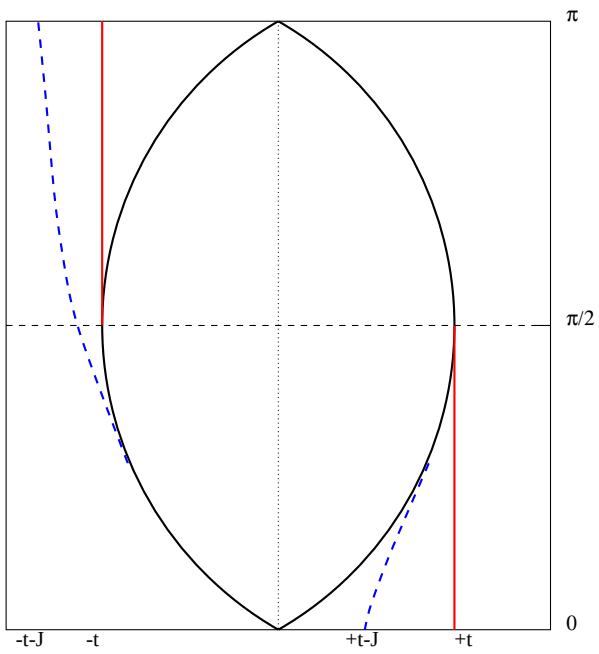


Figure 3.2: Support of the spectral function given by the CSSA (3.1) [41]. The spectral function is vanishing outside the area enclosed by the lines. The inner full lines correspond to a nonanalyticity of the spectral function having a dispersion $\sim t$. The outer full lines and the dotted lines correspond to the edge of the support and have a dispersion $\sim J$.

The simulations were performed at temperatures $T \leq \min(J,t)/15$, such that no appreciable changes with a further decrease in temperature can be seen: the results correspond to the zero temperature limit

## 3.2 The density of states

We start our comparison of the CSSA (3.1) with the density of states. Since the full bandwidth obtained by considering the compact support of the spectral function at $J = 0$ is known to be exactly $4t$ [88], we take $t_h = 2t$. In order to determine $J_s$, we consider the overall bandwidth, as obtained from the simulation. As can be seen in Fig. 3.3, for all values of $J$, the width of the density of states $N(\omega)$ scales approximately as $4t + J$ in the parameter range considered, leading to $J_s = J$.

The simple CSSA predicts a square root singularity along the lines, which have a dispersion $\sim J$ (the dotted line and the straight line in Fig. 3.3, respectively). The main characteristic of the density of states obtained from our simulations is an accumulation of a significant part of the weight both in a peak at low energies, and in a second peak

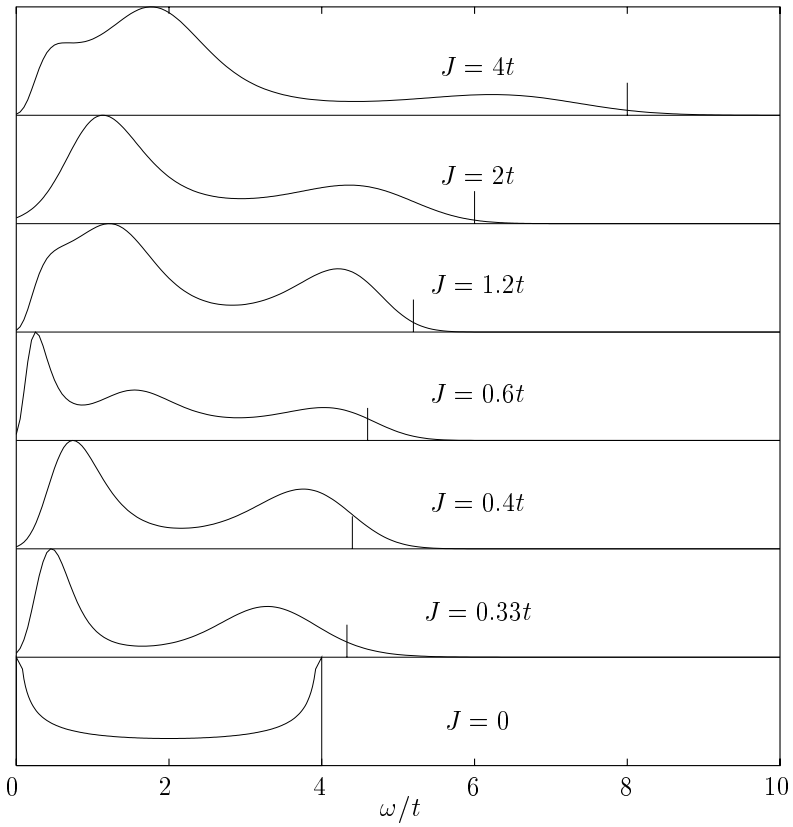


Figure 3.3: The density of states in one dimension in chain of length $L = 64$. The vertical bar indicates $4t + 2J$, the higher edge for the density of states predicted by the charge spin separation *Ansatz*. The density of states for $J/t = 0$ is taken from Ref. [88, 89].

at high energies. Similar to the behavior of the overall bandwidth, the distance between these two peaks increases linearly with $J$. These two outer peaks can be identified with the singularities of the CSSA. For $0.33 \leq J/t \leq 2$, there is no clear indication for a transfer of weight from high to low energies or vice versa.

## 3.3 The spectral function

Beyond predicting bandwidths, the CSSA in one dimension describes accurately the support of the spectral function in the case $J = 0$, when compared with exact results [41, 88, 90]. In the limit of infinite strong correlations ($U = \infty$ or $J = 0$), where the complete spectral function is available, additional singularities along all the *holon* lines of Fig. 3.3 (inner full lines) have been observed. These structures can be repro-

duced, when phase string effects [41, 91] are taken into account in the CSSA. In this case, spinon and holon are not independent from each other, but are coupled by a non-local phase string of the form $\exp(\Theta^h + \Theta^s)$, where $\Theta^h$ and $\Theta^s$ are phases corresponding to the spinon and holon respectively. For finite $J$, the minimal (maximal) possible energy of a hole in CSSA is given by $E(k) = -F_k$ ($E(k) = F_k$) for $k < k_0$ ($k > k_0$), where $F_k \equiv \sqrt{J^2 + 4t^2 - 4tJ\cos(k)}$ contains both holon and spinon contributions, and $k_0$ is determined by $\cos(k_0) = J/(2t)$. The remaining parts of the compact support are given by $E(k) = \mp 2t\sin(k)$ for $k > k_0$ (lower edge) and $k < k_0$ (upper edge) respectively. Such dispersions correspond to holons with momentum $k + q_s$, and a spinon with $q_s = \mp\pi/2$ [41, 44]. As $J \to 2t$, $k_0 \to 0$ and the lower edge of the compact support is entirely determined by the dispersion of the holon.

We now compare the above predictions with our QMC data. Fig. 3.4 shows the spectral function for values of $J/t$ ranging from $J/t = 0.4$ to $J/t = 4$. In all cases the compact support is reproduced very well by the CSSA. The *Ansatz* also predicts singularities at the lower (upper) edge for $k < k_0$ ($k > k_0$), when phase strings are taken into account. The singularities along the lower holon line are also supported by a recent low energy theory combining bosonization and conformal field theory [44], which predicts a branch cut singularity. For all parameter values we observe dominant weight along the above mentioned lines. For $J/t = 0.4$ and $J/t = 0.6$ we have checked that the results

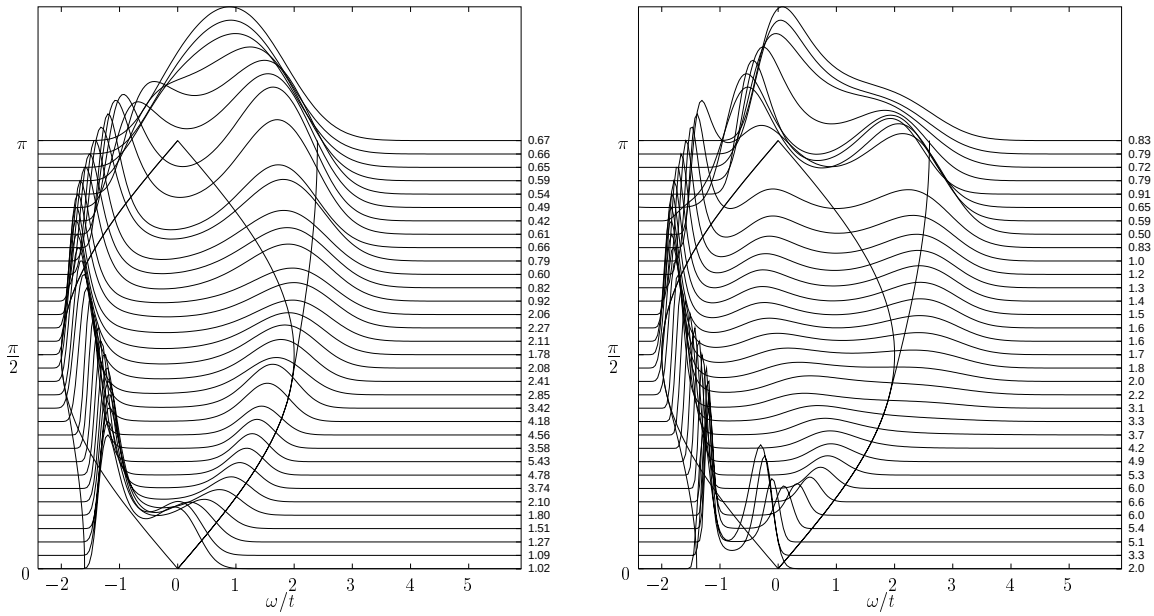


(a) $J = 0.4t$ (b) $J = 0.6t$

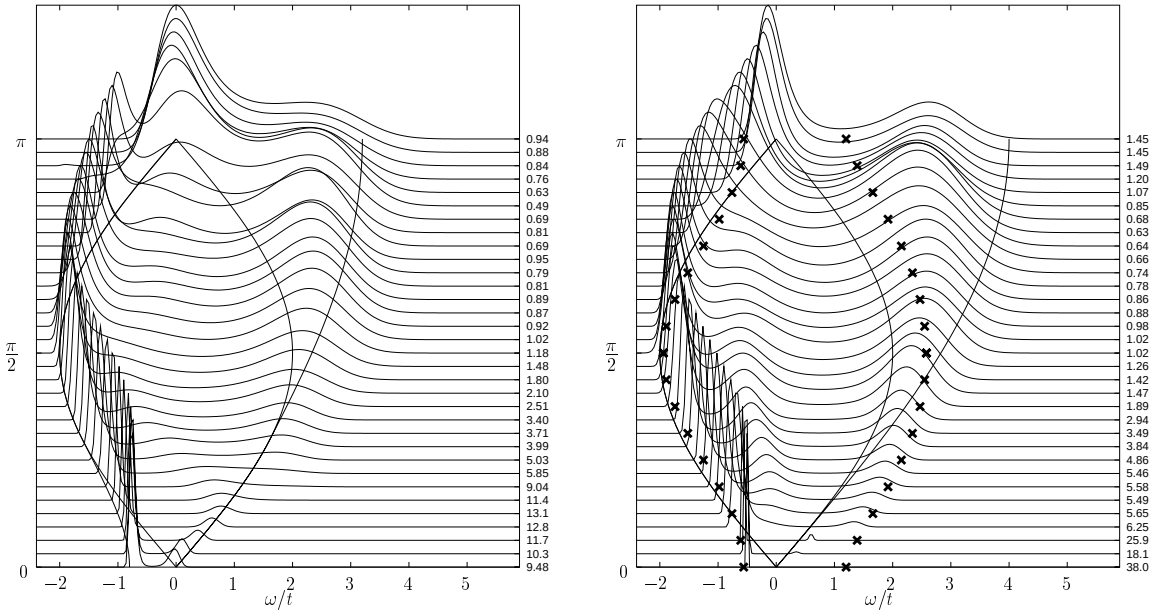


(c) $J = 1.2t$ (d) $J = 2t$

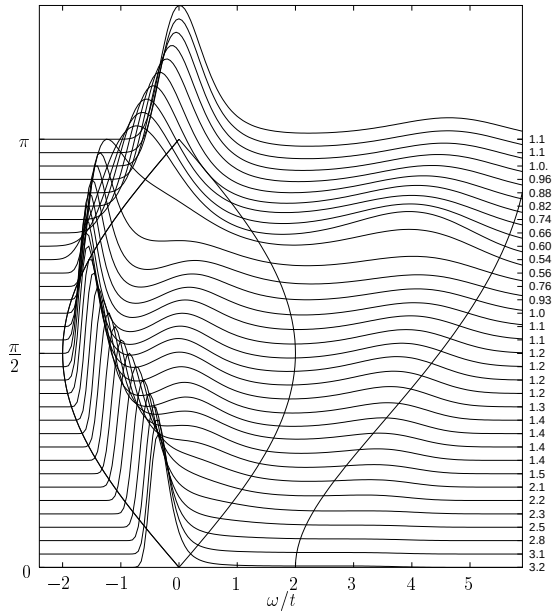


(e) $J = 4t$

Figure 3.4: The spectral function for various values of $J/t$. The lines correspond to the dispersion of the CSSA. The crosses for $J/t = 2$ corresponds to a CSSA using Bethe-*Ansatz* spinons and holons.

are consistent within the uncertainties of *Maximum Entropy* with a peak along the edges and a further peak along the holon lines, signaled by a broad structure between the edges and the holon lines (Fig. 3.4). This topic is discussed in more detail in Sec. 3.4

We observed such a behavior for $0.33 \leq J/t \leq 0.6$. For $J/t > 0.6$ the structure at the lower edge narrows considerably and the data are not any more consistent with an

additional structure along the lower holon line for $k < k_0$, but only with a singularity for $k > k_0$. At $J/t = 2$ the exact holon and spinon dispersions can be obtained by BA. [92].

Fig. 3.4.d shows the comparison with the CSSA, where on the one side the original dispersions are used (full line) and on the other side, with the dispersions as given by Bethe-*Ansatz* (crosses). Whereas the Bethe-*Ansatz* holon dispersion reproduces very well the lower edge, showing that as anticipated by the CSSA, at the supersymmetric point that edge is completely determined by the holon dispersion, the full bandwidth is better described with the original dispersions. We assign the additional weight in the region $k > \pi/2$ to processes involving one holon and more than one Bethe-*Ansatz* spinon. In fact, that portion resembles the difference between the supports for one-holon/one-spinon and one-holon/three-spinon processes in the inverse square root exchange $t$-$J$ model [93]. In our case, no limitation on the possible number of spinons exists, such that in principle all odd number of them are allowed. It is interesting to notice that using a fermionic spinon one is able to describe both the case $J = 0$ and $J = 2t$. In the first case, the spinon in the exact solution is a fermion. At the supersymmetric point it is expected to be a semion [93,94] and on the basis of our results, we conclude that the fermionic spinon contains all possible states with an odd number of semionic spinons.

## 3.4 The low-lying holon dispersion

The peak at the lower edge of the excitations spectrum accumulates appreciable weight. As both the weight and the exponential in the imaginary time Green's function corresponding to that peak can be measured with relatively good accuracy, one can remove this part from the Green's function, and use this modified Green's function as an input for *Maximum Entropy*, to obtain a possibly better resolution at higher energies. As we have seen in Sec. 2.4, large peaks tend to mask small peaks in their vicinity, such that removing the exponential corresponding to the low-lying excitation with large weight can possibly help to resolve excitations with little weight. The exact procedure will be demonstrated in detail in Sec. 4.3.3 on page 63 for the two-dimensional case, where this method allows the resolution of little structures, that are not visible, when the full Green's function is used for *Maximum Entropy*.

For the one-dimensional case, the problem, that we address is, whether two or three

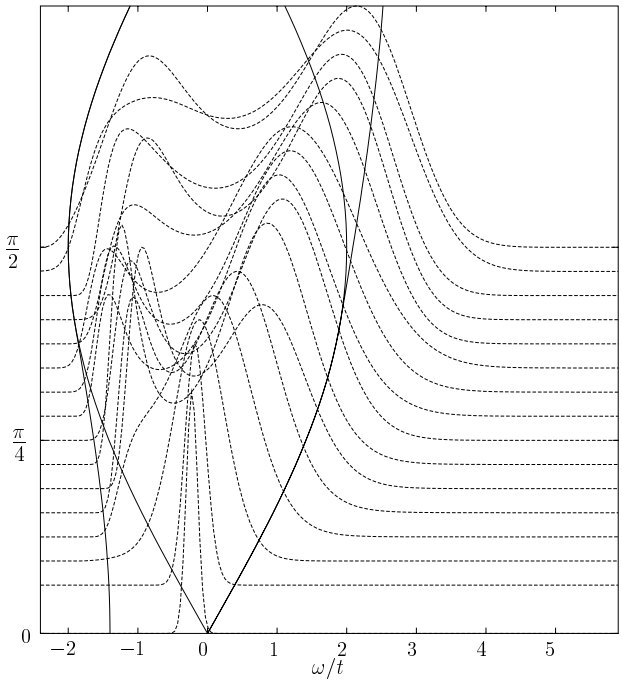


Figure 3.5: The spectral function for $J/t = 0.6$, when weight corresponding to the lower edge of the spectral function is removed from the Green's function.

separated peaks exist in the spectral function for $0 \leq k \leq \pi/2$. We apply the method to the case $J/t = 0.6$ (see Fig. 3.5). The figure first shows, that the low energy peak along the lower spinon line has vanished. This is the expected result, as we have subtracted the exponential which corresponds to this excitation. Further we observe weight along the low-lying holon line, as predicted from the CSSA. However, we cannot definitely conclude, whether this weight corresponds to some singularity, as predicted by calculations, which include phase-string effects [41], or if it rather corresponds to an incoherent background.

One has to notice at this point, that the above procedure is not very well defined in the one-dimensional case. The main reason being that we subtract a single exponential corresponding to a $\delta$-like excitation from the Green's function. On the other hand we now, that this quasiparticle weight vanishes in the thermodynamic limit, and is therefore very small in the relatively large lattice ($L = 64$) we consider here. This is different from the two-dimensional case, were the above procedure is much better defined, and the results are thus more reliable.

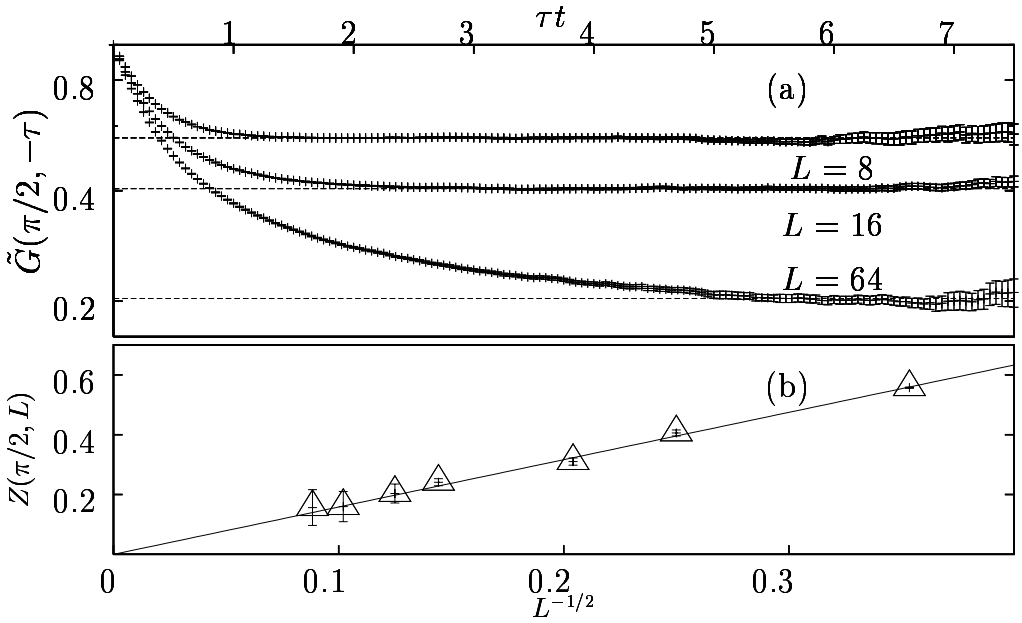


Figure 3.6: Quasiparticle weight in one dimension at $J/t = 2$. $\beta J = 30$ for $L \leq 48$, $\beta J = 60$ for $48 < L \leq 96$ and $\beta J = 90$ for $L = 128$ to guarantee convergence in $\tau$. In (b) we show the finite size scaling of the intersects from (a).

## 3.5 The quasiparticle weight

Finally, we consider the quasiparticle residue $Z_k = \left|\langle \Psi_0^{L-1} | \tilde{c}_{k\sigma} | \Psi_0^L \rangle\right|^2$ at $k = \pi/2$ for $J = 2t$. As shown in Fig. 3.4, the lower edge is very sharp and without prior knowledge, the question may arise whether we are dealing with a quasiparticle. $Z_k$ is related to the imaginary time Green's function through

$$\lim_{\tau\to\infty} G(k, -\tau) \propto Z_k \exp\left[\tau\left(E_0^L - E_0^{L-1}(k)\right)\right], \tag{3.2}$$

and is thus the weight of the exponential corresponding to the excitation with minimal energy at the respective $k$-point. Fig. 3.6.a shows $2\Big[G(\pi/2, -\tau)\exp\Big(-\tau\big(E_0^L - E_0^{L-1}(\pi/2)\big)\Big)\Big]$ versus $\tau t$, where the energy difference is obtained by fitting the tail of $G(\pi/2, -\tau)$ to a single exponential form, for several sizes. The thus estimated $Z(\pi/2)$ (see Fig. 3.6.a) is plotted versus system size in Fig. 3.6.b, where the errors are given by the standard deviation of the least square fit. The normalization is chosen, such that the maximal possible quasiparticle weight is one. Our results are consistent with a vanishing quasiparticle weight $Z(\pi/2) \propto L^{-1/2}$ which is the scaling obtained by a combination of bosonization and conformal field theory [44].

# Chapter 4

# A single hole in the two-dimensional $t$-$J$ model

The problem of a single hole in a two-dimensional quantum antiferromagnet has attracted a lot of attention both from the analytical [53, 55, 95–102] and from the numerical side [32,33,46–53,103–106]. The interest has been renewed in recent years due to its relevance for the $CuO_2$-based high-temperature superconductors [3, 7].

Quite recently, angle resolved photoemission spectroscopy (ARPRES) experiments on under- and undoped CuO materials are available. Among others, ARPES experiments were performed on the quasi-two-dimensional materials $Sr_2CuO_2Cl_2$ [12, 14, 15] and $Ca_2CuO_2Cl_2$ [107]. These measurements provide an experimental realization of hole motion in an antiferromagnetic background.

## 4.1 Known results and established approximations

All results, both theoretical and experimental, show, that the propagation of the hole is strongly influenced by the spin background. If $J/t$ is not too small, the antiferromagnetic order remains stable around the hole [22]. In the limit $J/t \ll 1$, and $J_x = J_y = 0$ (classical Ising antiferromagnet, $t$-$J_z$ model), the dynamics of a single hole can be well understood by the string picture (see Fig. 4.1) [47, 53, 95, 108]. Here the hole moves in the spin background, which cannot be repaired, since the spin dynamics is absent, leading to a string of parallel spins along the path of the hole. To repair the unsatisfied bonds the

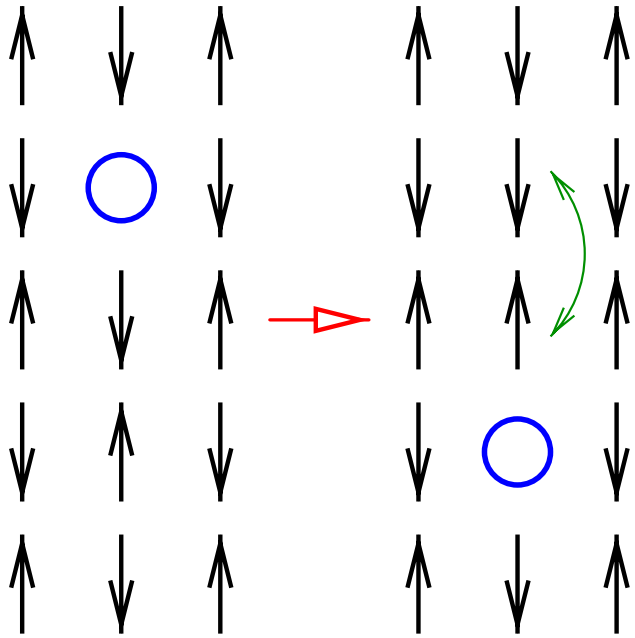

Figure 4.1: Effect of a hole moving in a Néel background in the limit $J \ll t$. The hopping of the hole creates two bonds with parallel spins. The system can reorder to the Néel state either when the hole traces back its original way, or by spin exchange. The latter process is excluded in the $t$-$J_z$ model .

hole has to trace back the old way. Without disturbing the spin background, the hole can only move via a process in 6th order in $t$, which moves it further one lattice site both in $x$ and $y$ direction [108]. The string contribution leads to an effective linear confining potential at short distances. For the $t$-$J_z$ model, a continuum limit can be obtained, where the hole can be taken as a particle moving in a one-dimensional linear potential ($x \geq 0$) described by the Hamiltonian (see App. B) [54–56]

$$H_{\mathrm{S}} = -t\frac{\partial^2}{\partial x^2} + J_z x - 2\sqrt{z-1}t, \tag{4.1}$$

with the eigenvalues (for the coordination number $z = 4$) given by

$$E_n = \left(\frac{J_z}{t}\right)^{2/3} t a_n - 2\sqrt{3}t, \tag{4.2}$$

where $a_n$ are the eigenvalues of the dimensionless Airy equation ($a_1 = 2.34, a_2 = 4.09, a_3 = 5.52, \ldots$). It should be noticed, that $x$ does not correspond to the two-dimensional distance of the hole to the minimum of the potential, but to the number of jumps (going one lattice point upward, and one to the right gives $x = 2$, and not $x = \sqrt{2}$). The corresponding eigenfunctions in space extend to the classical turning point $x_m = a_i \left(\frac{t}{J}\right)^{1/3} \approx a_i$ (see

App. B) [109]. When the distance is larger than the classical turning point, there is an exponential decay of weight with a typical lengthscale of $\xi = \sqrt{t/J} \approx 1$. The lowest possible string excitation always occurs, when the hole moves two sites, to stay in the same sublattice (see Fig. 4.1), the next two excitations correspond to cutting two and three additional bonds in the antiferromagnet, respectively. Although the length of the strings are too short to speak of a continuum, in the $t$-$J_z$ model very accurate results can be produced in that simple picture [56, 95].

At least for $J/t \ll 1$ a similar picture should apply to the $t$-$J$ model with the full spin dynamics at not too large distances, as the motion of the hole is much faster, than the exchange processes, which can repair the broken bonds. When $J/t$ increases, the maximal length of the string decreases, as the disturbed spin background can be readjusted by spin exchange. For $J \approx t$, as is the case in our simulations, it is not clear if the string effect is still visible, as spin relaxation and hole motion occur on the same time scale. This problem cannot be addressed by other QMC algorithms such as Green's function Monte Carlo, that can only evaluate the lower edge of the spectrum, and exact diagonalizations are problematic, since a string is of the same size as or larger than the considered systems.

Another prediction of approximative approaches, such as self consistent Born approximation (SCBA) [52, 53], are dispersing bands, which are flat around the $k$-points $(\pm\pi, 0)$ and $(0, \pm\pi)$ (often called $X$-point). Further a minimum of the dispersion at $\mathbf{k} = (\pm\pi/2, \pm\pi/2)$ ($\bar{M}$-point) is predicted.

Green's function QMC calculations (GFMC) [32, 33, 103] were able to verify both points. It was shown, that at $J/t = 0.4$ the single hole energy at the $k$-points $(\pm\pi/2, \pm\pi/2)$ is about $0.15t$ smaller than at $(\pm\pi, 0)$, $(0, \pm\pi)$, and they have confirmed the flat band structure. For $J/t \geq 1$ the complete lower edge of the spectral function was accurately obtained by series expansion [51]. As already stated above, higher excitations cannot be obtained by series expansion or GFMC.

Unfortunately exact diagonalizations were not able to clarify the points above. The reason is, that the $k$-points $(\pm\pi/2, \pm\pi/2)$ and $(0, \pm\pi)$ are identical in a $4 \times 4$ system [47]. In the largest system, that exact diagonalization can reach at the moment $(\sqrt{32} \times \sqrt{32})$, the wave vector $\mathbf{k} = (\pm\pi/2, \pm\pi/2)$ is not exactly an allowed $k$-point [49]. The next system size, which contains this momentum is $8 \times 8$, what is definitely not accessible to exact diagonalizations at the present time.

## 4.2 The density of states

For the density of states the only existing numerical results are those from exact diagonalizations [46–49]. They show a high density of excitations at low energies and a second accumulation of excitations about $4t$ higher in energy. As can be seen in Fig. 4.2, the results from our calculations are in agreement with those of exact diagonalizations. Finite-size effects are therefore not relevant, when only the overall shape of $N(\omega)$ is considered.

The first remarkable point is, that the peak at low energies remains unchanged in general for different $J/t$. The change is smaller than uncertainties introduced by *Maximum Entropy*. We further observe, that for all values of $J/t$ the overall bandwidth increases only little with $J$, in contrast to the one-dimensional case. The main effect is a shift of weight from high energies to the low-energy peak.

The question, whether excitations at high energies are gapped with respect to those at low energies cannot be addressed by the results of *Maximum Entropy* at this point, and will be addressed again in Sec. 4.3.3. Whereas at $J/t = 0.4$ and $J/t = 0.6$ the peaks seems to be separated, at $J/t = 0.8$ and $J/t = 2$ the peaks in the spectrum are clearly

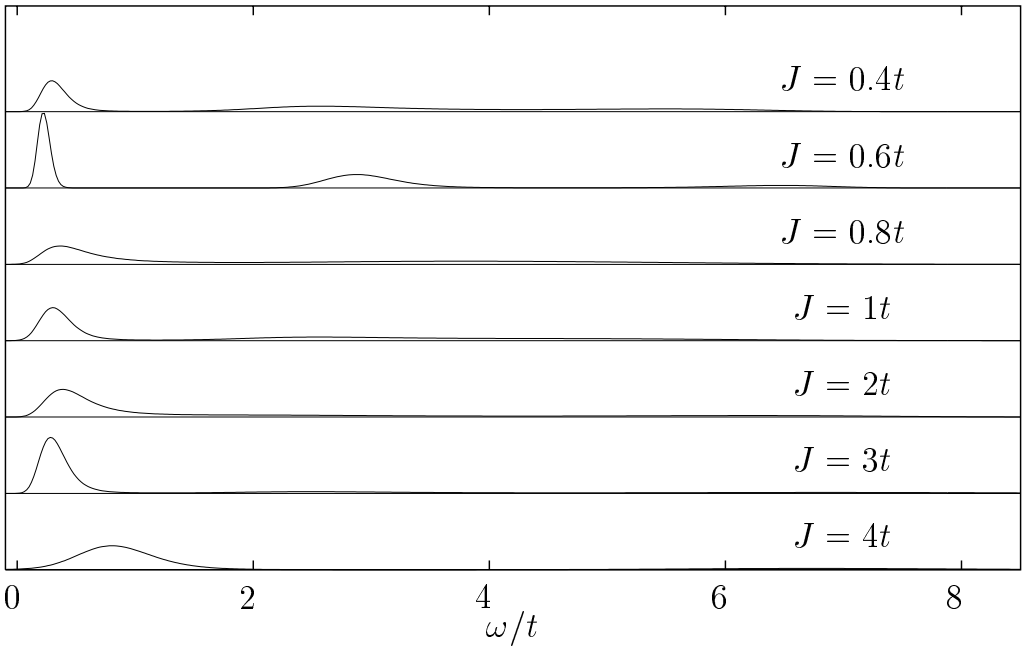


Figure 4.2: Density of states in two dimensions as obtained by eq. (2.23) for different values of $J/t$ on a $16 \times 16$ lattice. We shift the energy by $\tilde{\epsilon}$ in order to have all systems at the same range.

joint. At this point, we cannot clarify, whether this is a property of the system, or only an artefact of the *Maximum Entropy* method.

## 4.3 The momentum resolved spectrum

As for the density of states, most of the numerical results for the complete spectral function emerge from exact diagonalizations [46–49, 109]. Only for the lower edge of the spectrum calculations by series expansion [51], GFMC [32, 33] and by variational Monte Carlo [50] have been performed.

Analytic predictions about the spectral function emerge from the retraceable path approximation [95] and from perturbation theory [55] in the limit $J/t \to 0$. Whereas the retraceable path approximation, which only considers an Ising spin background does not produce a dispersing quasiparticle, the perturbational analysis in the Heisenberg limit gives a quasiparticle, with the minimum of the dispersion at $\mathbf{k} = (\pi/2, \pi/2)$. Further SCBA [52, 53], where the spin dynamics is treated in linear spin-wave theory, is able to derive results for the quasiparticle dispersion, higher excitations in the spectral function, and the quasiparticle weight.

### 4.3.1 The lower edge of the spectrum

In our case, the lower edge of the spectrum can directly be taken from the imaginary time Green's function as the slope at large $\tau$. The procedure and the quality of the data are demonstrated in Fig. 4.3. At a glance, one can see, that the accuracy of the result depends critically upon the value of $J/t$. The most accurate results are obtained, when $J/t$ approaches values between 1 and 2. For $J/t = 0.4$ we made additional calculations at $\Delta\tau t = 0.2$ (all other calculations are done at $\Delta\tau t = 0.05$), where the statistics is slightly better at large $\tau t$ (see Fig. 4.4). The resulting Green's functions are the same within the error bars, indicating a small $\Delta\tau$ effect. However, the number of points, that can be used to evaluate the slope is greatly reduced, leading to large error bars.

The lower edge of the spectrum was obtained for all points along the symmetry axes of the Brillouin zone as indicated in Fig. 4.5.

We compare our results (see Fig. 4.6) to results, obtained by GFMC where possible,

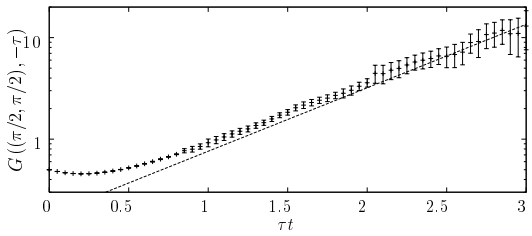


(a) $J = 0.4t$, $\mathbf{k} = (\pi/2, \pi/2)$

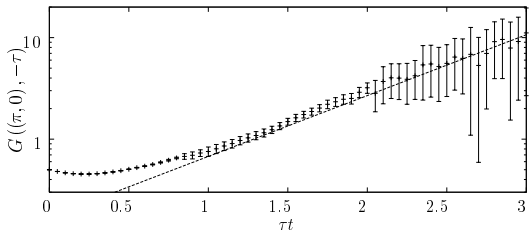


(b) $J = 0.4t$, $\mathbf{k} = (0, \pi)$

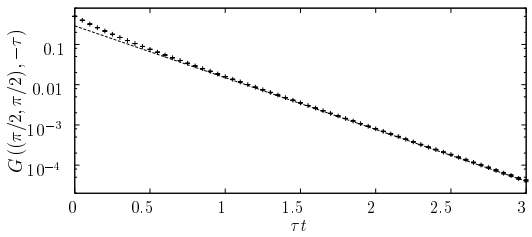


(c) $J = 2t$, $\mathbf{k} = (\pi/2, \pi/2)$

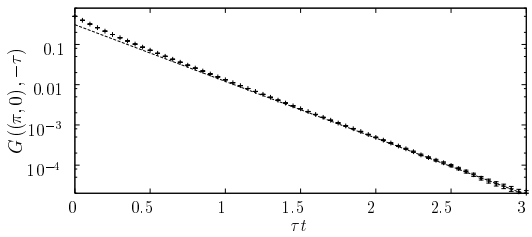


(d) $J = 2t$, $\mathbf{k} = (0, \pi)$

Figure 4.3: The energy of the lowest excitation can be obtained by the slope at high $\tau t$ on a logarithmic scale indicated by the straight line. This procedure becomes more accurate, when approaching $J \sim t$. The Green's functions were obtained by taking $\Delta\tau t = 0.05$

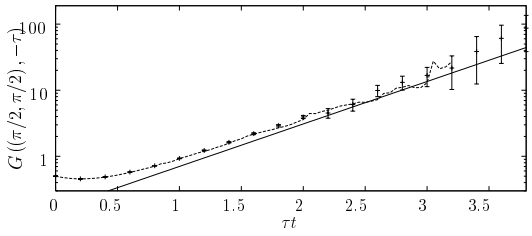


(a) $\mathbf{k} = (\pi/2, \pi/2)$

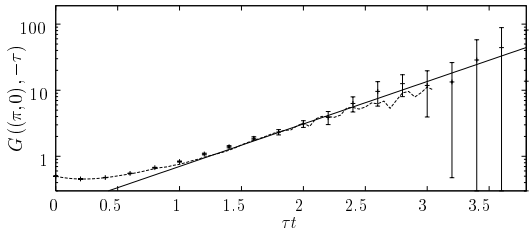


(b) $\mathbf{k} = (\pi/2, \pi/2)$

Figure 4.4: Green's function for $J/t = 0.4t$ and $\Delta\tau = 0.2$. It can be seen that only a few points can be considered to determine the slope at large $\tau$. The results for $\Delta\tau = 0.05$ are given by the thin line, and are within the error bars of $\Delta\tau = 0.2$.

and observe a good agreement of our results with GFMC at $J/t = 0.4$. For small values of $J/t$ the variational calculation [50], having an error of $0.02t$ for all $k$-points also appear to be very accurate concerning the lower edge. When its energies are compared to our calculations and the GFMC technique, we find , that their energies are within the error bars of the *exact* QMC calculations. At $J/t = 0.4$ and $\mathbf{k} = (0, 0)$, the variational result is at the lower edge of the error bars of our calculation, and the variational calculations have the smallest statistical error of all three approaches. At this specific $k$-point both GFMC and our approach have problems to reach the ground state. As already mentioned, we

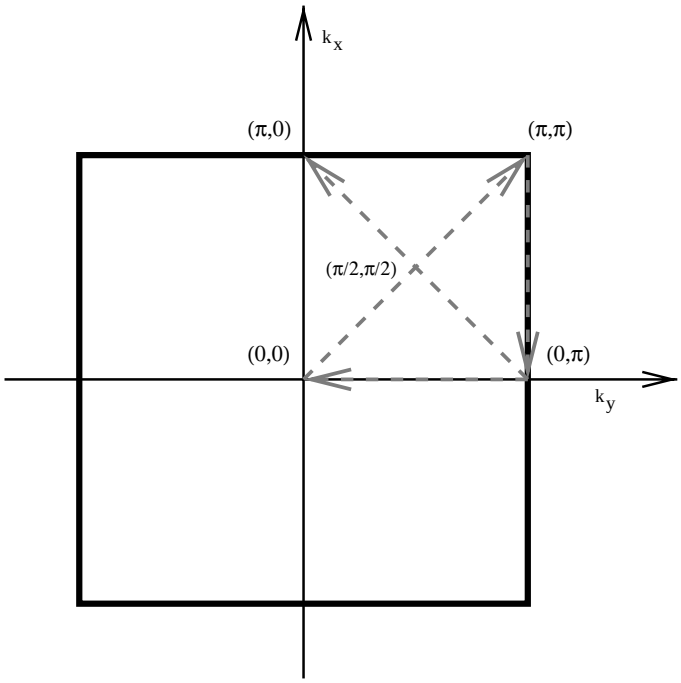


Figure 4.5: Paths in the symmetry axes shown in the following picture. It should be noticed, that the points in the triangle $(0,0) - (\pi,\pi) - (0,\pi)$ contain all information, as all other points are connected to them by symmetries.

thus carried out additional calculations at $\Delta\tau t = 0.2$. The energies for $\mathbf{k} = (\pi/2, \pi/2)$ and $\mathbf{k} = (\pi, 0)$ are indicated in Fig. 4.6, At $\mathbf{k} = (\pi/2, \pi/2)$ the energy one obtains at $\Delta\tau = 0.2$ is somewhat lower than for $\Delta\tau t = 0.05$, but the deviation is not significant. This is not a systematic error scaling like $\mathcal{O}(\Delta\tau)^2$ (see Sec. 2.1.2) [70, 76, 110], as can be seen in Fig. 4.4, where we compare the data with $\Delta\tau = 0.05$ to that of $\Delta\tau = 0.2$.

At $J/t = 2$, where our algorithm works much more accurately, one can see, that the variational results are too high in energy. For values of $J/t \geq 1$ additional results from series expansion [51] are available. At $J/t = 2$ we compare them to our results and observe a very good agreement. Only around $(\pi, 0)$ we find a small deviation from the series expansion calculation.

All calculations, both exact ones such as GFMC and approximate ones such as SCBA lead to flat bands around $\mathbf{k} = (\pi, 0)$. These flat bands are clearly confirmed by our calculations. They can be well observed for all considered values of $J/t$, both when considering the lower edge (Fig. 4.6) and the complete spectral function (Fig. 4.11-4.16 on pages 61f). The area in the Brillouin zone, which is covered by the flat band is shown explicitly in Fig. 4.8. Our data clearly show for $J/t \geq 0.6$, that the neighboring points of

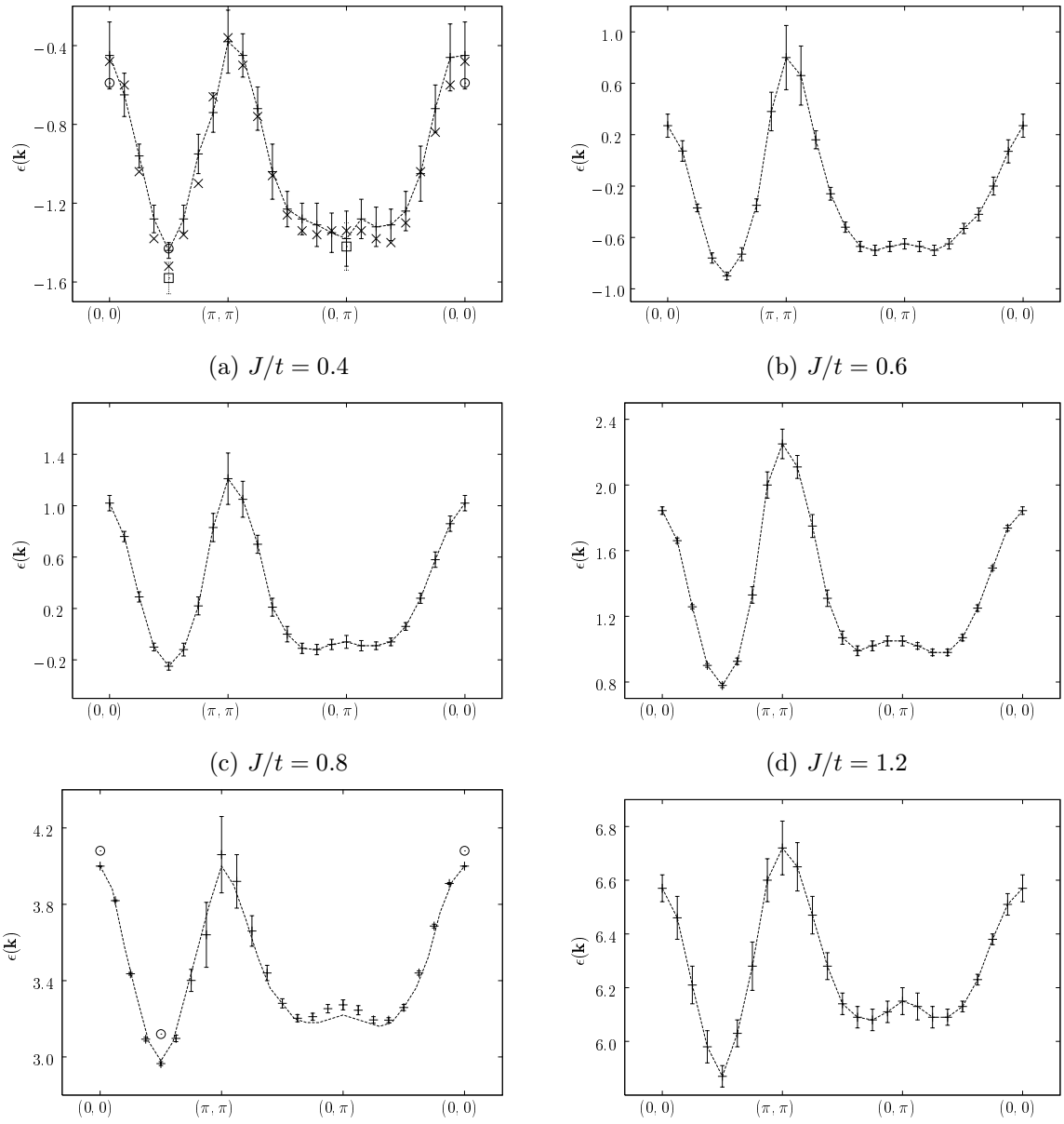


(a) $J/t = 0.4$ (b) $J/t = 0.6$

(c) $J/t = 0.8$ (d) $J/t = 1.2$

(e) $J/t = 2$ (f) $J/t = 4$

Figure 4.6: Lower edge of the spectrum along the symmetry axis of the Brillouin zone compared to variational Monte Carlo [50] (circles) for $J/t = 0.4$ and $J/t = 2$ and Green's function Monte Carlo for $J/t = 0.4$ [33] ($\times$). We give additionally our results for $\Delta\tau t = 0.02$ for $J/t = 0.4(\square)$. The results from series expansion for $J/t = 2$ [51] are indicated by the line, in all other cases the line is just a guide to the eye. All our results are for a $16 \times 16$ lattice.

$\mathbf{k} = (\pi, 0)$ are generally lower in energy. The band in this area is thus not completely flat, but it changes its curvature, where within the error bars, the points $(\pi, \delta)$ and $(\pi - \delta, 0)$ have the same energy. When going in the $(0, 0)$ and $(\pi, \pi)$ direction, the minimum is reached between $(2\pi/8, \pi) - (3\pi/8, \pi)$ resp. $(0, 6\pi/8) - (0, 5\pi/8)$, so that the symmetry

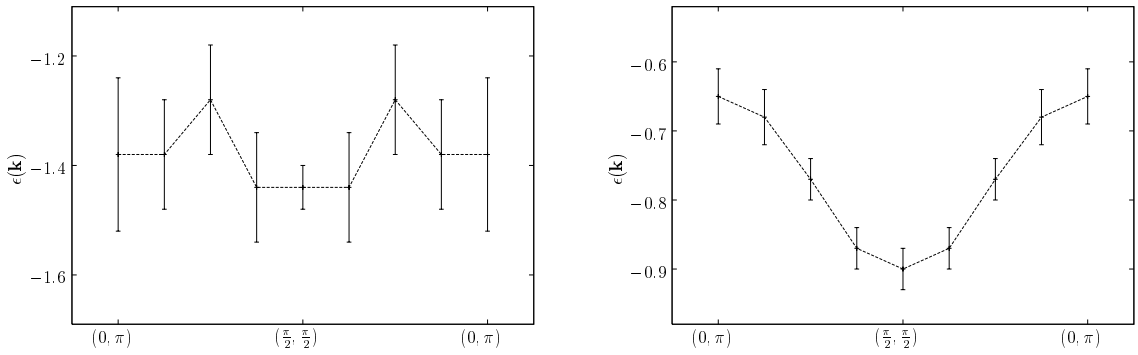


(a) $J/t = 0.4$




(b) $J/t = 0.6$

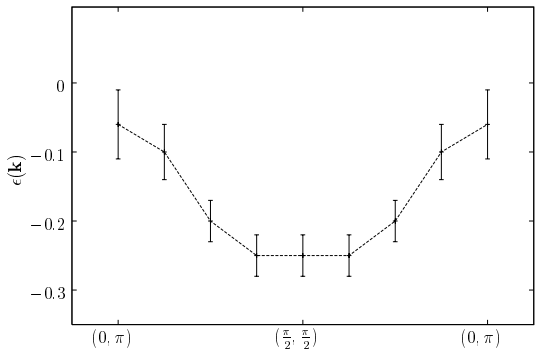


(c) $J/t = 0.8$

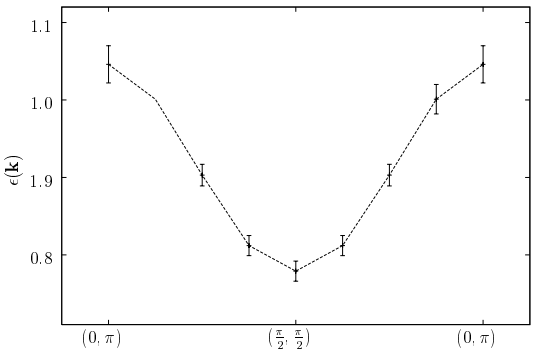


(d) $J/t = 1.2$

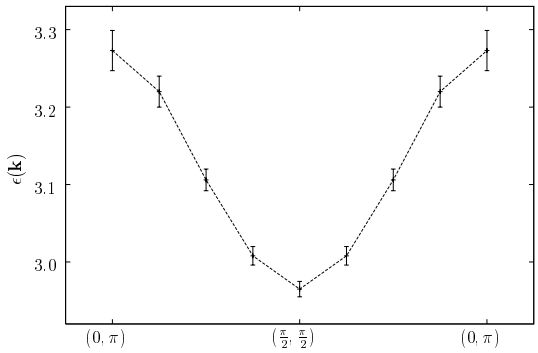


(e) $J/t = 2$

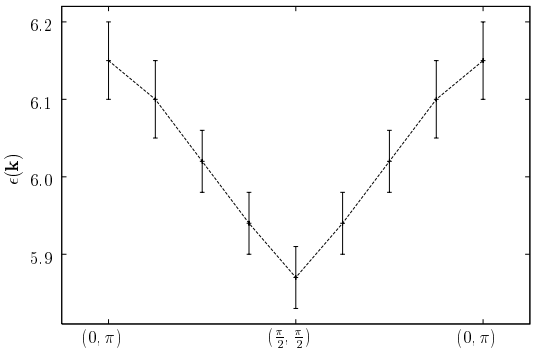


(f) $J/t = 4$

Figure 4.7: Lower edge of $A(k,\omega)$ going from $k = (\pi, 0)$ to $k = (0, \pi)$.

is fulfilled up to approximately $\delta \leq 0.3\pi$. The flat region of the band spans an extremely large area in the Brillouin zone, including the points $(\pi/2, 0)$, $(\pi, \pi/2)$, $(0, \pi/2)$, $(\pi/2, \pi)$, and $(\pi/2, \pi/2)$ (see Fig. 4.8).

The absolute minimum of the dispersion is always at $\mathbf{k} = (\pm\pi/2, \pm\pi/2)$. For all values of $J/t$, except for $J/t = 0.4$, this result is well outside of statistical errors. The energy gap between the $k$-points $\mathbf{k} = (\pi/2, \pi/2)$ and $\mathbf{k} = (\pi, 0)$ is about $\Delta = (0.25 \pm 0.05)t$, and no significant dependence on $J/t$ can be observed in the considered range (see Fig 4.7).

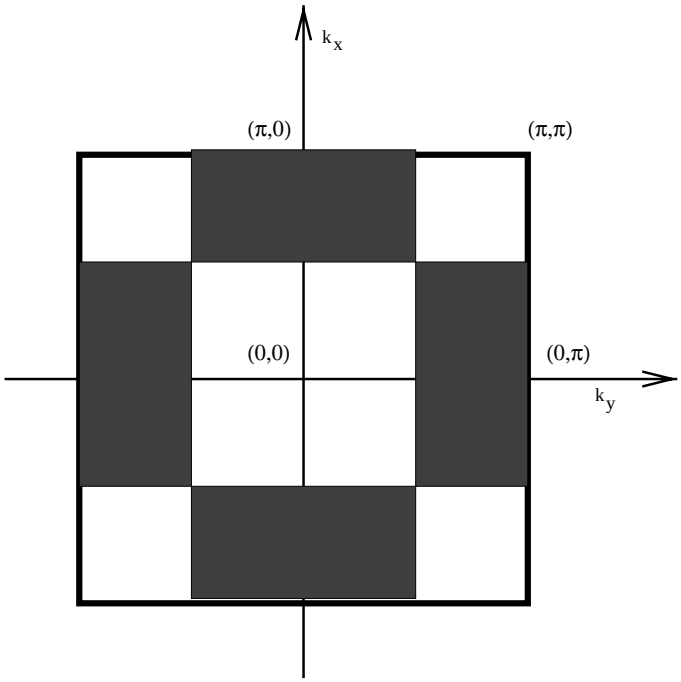


Figure 4.8: Area in the Brillouin zone, that is covered by the flat band (shaded) .

The SCBA [52] gives values ranging from $0.17t$ ($J/t = 1$) to $0.12t$ ($J/t = 4$), which are smaller than the values we obtain. Series expansions [51] on the other hand obtain values between $0.25t$ at $J/t = 2.4$, $0.22t$ at $J/t = 4$ and $0.15t$ at $J/t = 1$. At values of $J/t < 1$ the series expansion leads to an energy difference of about $0.15J/t$. However, in this region, the series do not show good convergence. The value obtained by series expansion is consistent with our results for large values of $J/t$. In the related Hubbard model (1.1) the gap between $(\pi/2, \pi/2)$ and $(\pi, 0)$ has not been observed [28] until now.

In Fig. 4.9, we plot the energy of the lowest lying state for different values of $J/t$. Again we compare with variational results [50]. The energy difference of the lowest one hole state from the Heisenberg energy scales like $\epsilon(\pi/2, \pi/2) = -3.28t - E_H + 2.33J^{2/3}$ for $J/t \leq 2$, where $E_H$ is the Heisenberg energy per site, and drops below that curve at higher values of $J/t$. The motivation for the choice of this special scaling is given by the string picture of eqs.(4.1,4.2). String effects will be discussed in detail in Sec. 4.3.3.

The intersection of the energy $\epsilon(\pi/2, \pi/2) = 0$ is between $J = 0.8t$ and $J = t$. An interpolation between the two values results in $J_0/t = 0.88 \pm 0.03$. This means, that above $J/t = 0.88$ a quantum Heisenberg antiferromagnet looses energy, when it is doped with a holes, that do not pair or interact in any other way. This result is in the same order as the critical value of $J/t$ for phase separation obtained by GFMC with stochastic

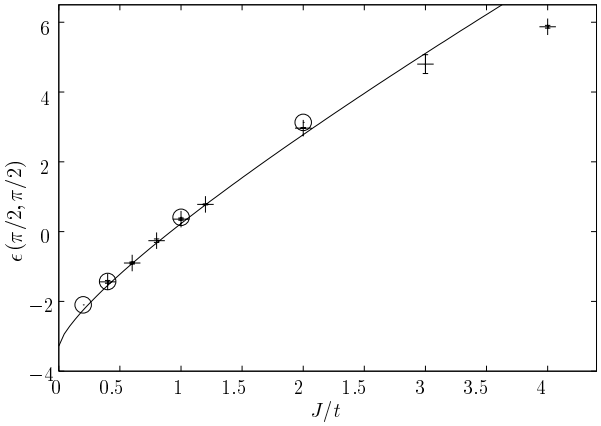


Figure 4.9: Energy of the lowest-lying state $\mathbf{k} = (\pi/2, \pi/2)$. The variational results are represented by the open circles. All points are values taken from $16 \times 16$ lattices. The line corresponds to $-3.28t - E_H + 2.33J^{2/3}$. Below $J/t = 2$ the lower edge clearly follows the fit, whereas above, the lowest energy falls below that value.

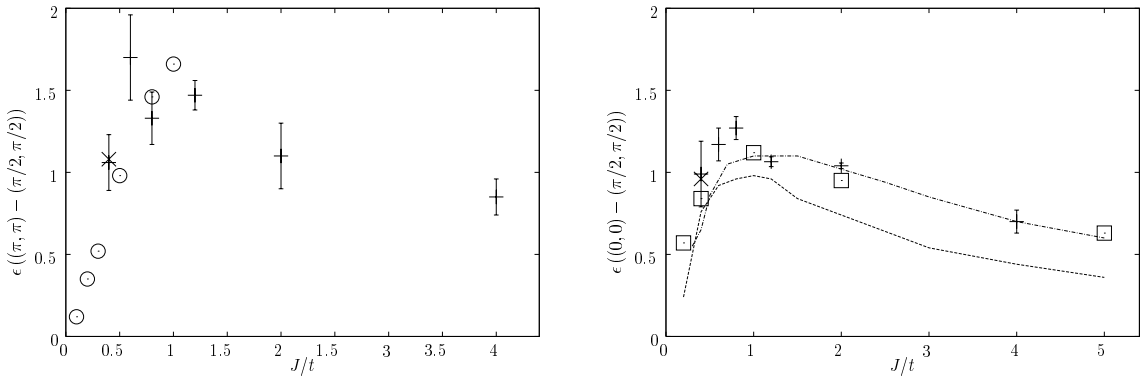


(a) Overall bandwidth $(\epsilon(\pi,\pi) - \epsilon(\pi/2,\pi/2))$ (b) $\epsilon(0,0) - \epsilon(\pi/2,\pi/2))$

Figure 4.10: Overall bandwidth ( $\epsilon(\pi,\pi) - \epsilon(\pi/2,\pi/2))$ and $\epsilon(0,0) - \epsilon(\pi/2,\pi/2)$ for different values of $J/t$. The open circles represent results from exact diagonalizations, the lower line in (b) shows the results of self consistent Born approximation in a $16 \times 16$ lattice, the crosses at $J/t = 0.4$ are the Green's function QMC results, and the open boxed represent results from variational QMC. The upper line in (b) shows the results from series expansion [51].

reconfiguration, that give a value of $J_c/t \approx 0.5$ [111]. This topic is still controversial, since other authors find phase separation for all values of $J/t$ [112]. If the holes have a negative (pair-)binding energy, the critical value for crossing the x-axis is shifted to larger values of $J/t$.

We finally use the lower edge of the spectrum to investigate both the overall bandwidth $\epsilon(\pi,\pi) - \epsilon(\pi/2,\pi/2)$, and the energy difference $\epsilon(0,0) - \epsilon(\pi/2,\pi/2)$. The latter is compared with the bandwidth resulting from SCBA [52] and series expansion [51], where the wave-

vectors $\mathbf{k} = (0, 0)$ and $(\pi, \pi)$ have degenerate energies. It can be seen in Fig. 4.10, that the bandwidth we obtain from our data is generally larger than the SCBA result. The qualitative behavior of the bandwidth is nevertheless the same. The bandwidth grows until $J/t \approx 1$, and then decreases monotonically. The results of the Green's function calculation [32] and of variational QMC [50] are consistent with the bandwidth we obtain. Again, excellent agreement is found with results obtained by series expansion [51] for $J/t \geq 1.2$. For $J/t \ll 1$ GFMC and our approach suffer from very large error bars. The only reliable results are those from exact diagonalizations [48] of systems up to 26 sites. Our results for $J/t = 0.4$, $J/t = 0.6$ and $J/t = 0.8$ are consistent with the exact ones. Unfortunately all the *exact* QMC approaches have an error of about $0.2t$ for the considered quantity at small values of $J/t$.

To summarize, the bandwidth of the lowest energy state in the Brillouin zone, has a qualitative behavior as predicted by the self consistent Born approximation. In the region $J/t < 1$, the bandwidth increases with $J/t$, whereas for $J/t > 1$ it decreases. At least for $J/t \geq 0.4$ the self consistent Born approximation underestimates the overall bandwidth systematically. Especially for $J/t \geq 1.2$ series expansion reproduces the correct bandwidth qualitatively and quantitatively.

### 4.3.2 The spectral function

The above results for the density of states and for the lower edge of the spectrum can be equally identified in the spectral function (Fig. 4.11-4.16), which is obtained by using the *Maximum Entropy* method on eq.(2.22). All the results for the lower edge remain as in the previous section, but the accuracy for this quantity in $A(\mathbf{k}, \omega)$ is reduced by the *Maximum Entropy* method.

For clarity, the maximum of each $A(\mathbf{k}, \omega)$ is normalized to 1 in the plots. The small numbers on the right hand side of the figures represent the maximum of each $A(\mathbf{k}, \omega)$ when the integral $\int_{-\infty}^{\infty} d\omega A(\mathbf{k}, \omega)$ is properly normalized to $\pi/2$ [1].

No significant dispersion can be observed for the peak at high energies, that generally has a width of about $2t$. The distance of its maximum to the lower edge of the band scales

[1] Recall, that the Green's function at $\tau = 0$ is given by G($\mathbf{k}$.0)=1/2 (eq.(2.19)), so this result follows immediately from the spectral theorem (2.22)

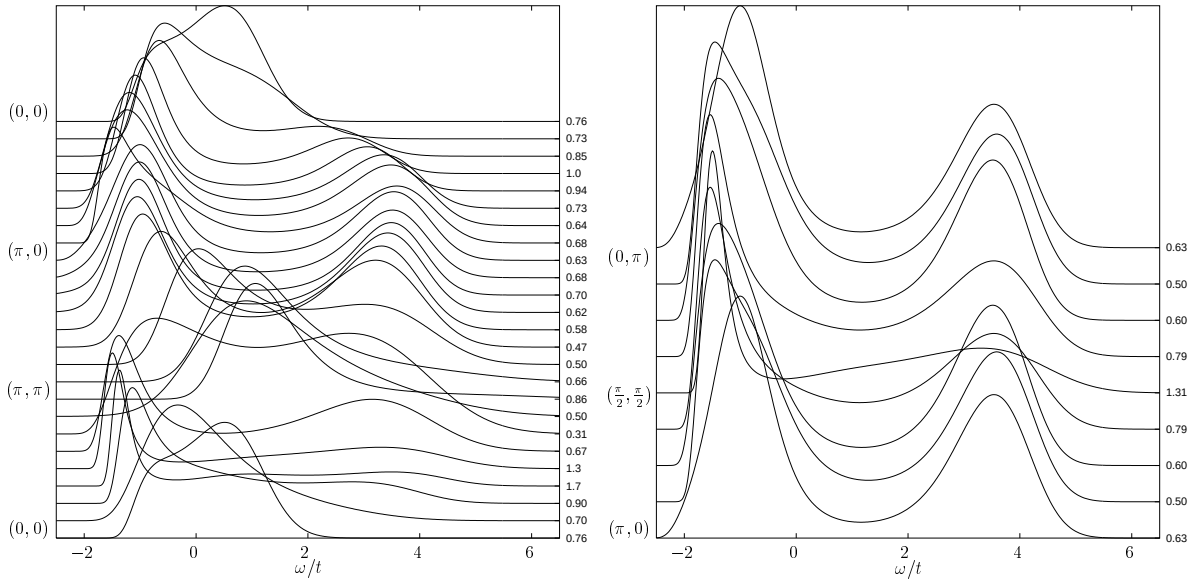


(a) (b)

Figure 4.11: Spectral function for a $16 \times 16$ system and $J/t = 0.4$.

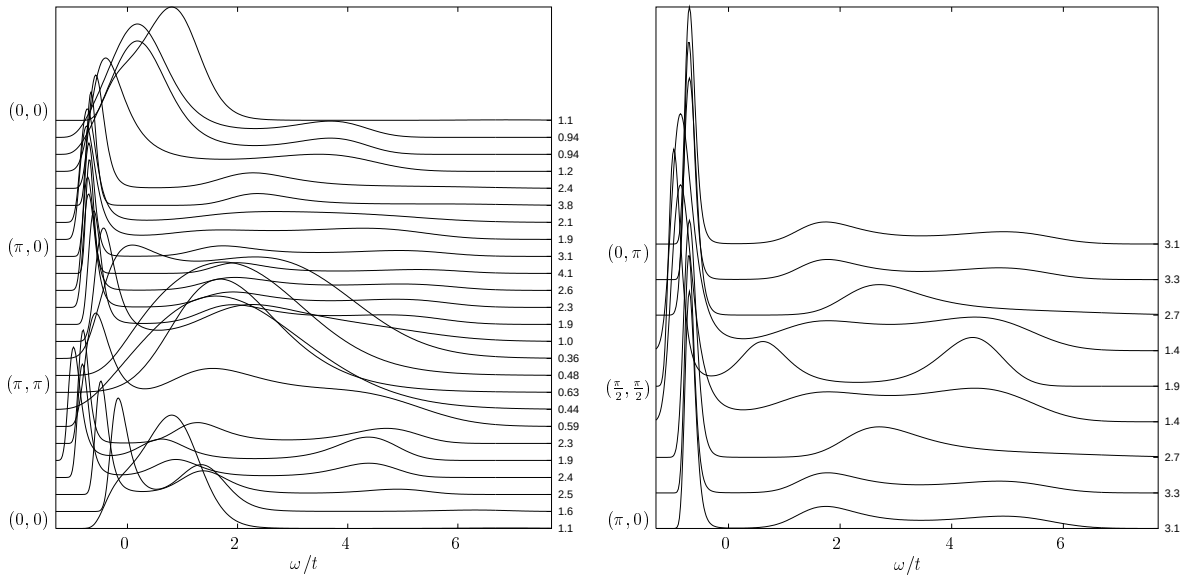


(a) (b)

Figure 4.12: Spectral function for a $16 \times 16$ system and $J/t = 0.6$.

approximately like $4t$, compared to the one-dimensional case the high energy excitation are extremely broad. The peaks around $(0, \pi)$ and $(\pi/2, \pi/2)$ are generally very sharp, suggesting the existence of a quasiparticle. Between $J/t = 0.6$ and $J/t = 2$, the shape of the peaks at the minimum of the dispersion is not changing significantly, whereas at $\mathbf{k} = (0, 0)$, the peak sharpens when approaching the supersymmetric point $J/t = 2$. The

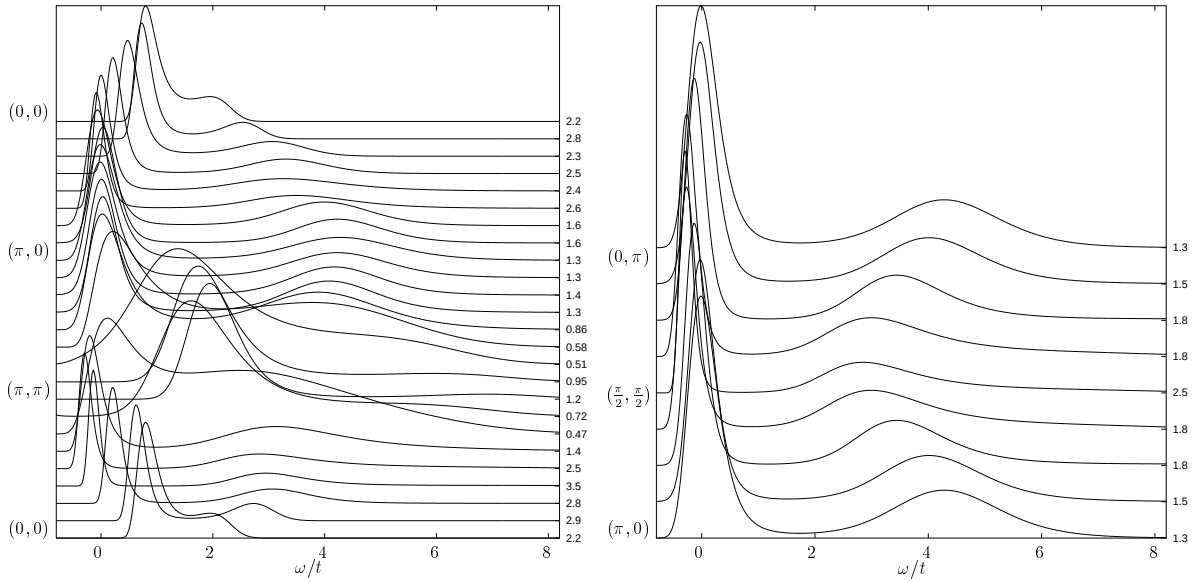


(a) (b)

Figure 4.13: Spectral function for a $16 \times 16$ system and $J/t = 0.8$.

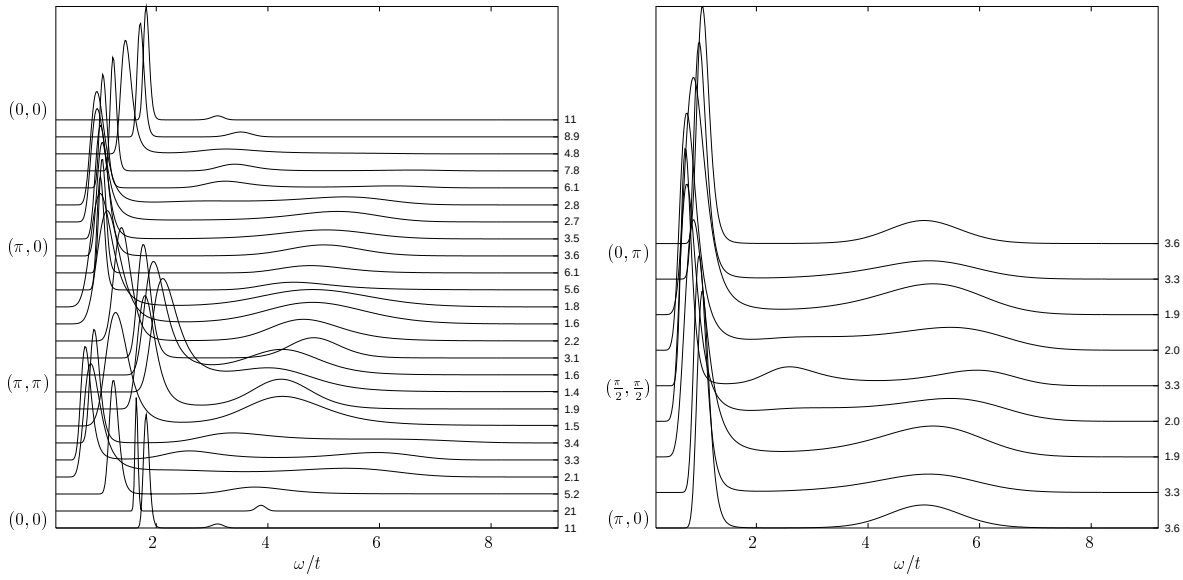


(a) (b)

Figure 4.14: Spectral function for a $16 \times 16$ system and $J/t = 1.2$

existence of a quasiparticle in the thermodynamic limit at the two $k$-points $\mathbf{k} = (\pi, 0)$ and $\mathbf{k} = (\pi/2, \pi/2)$ will be demonstrated in Sec. 4.4.

Especially around $(\pi/2, \pi/2)$, we observe an interesting additional structure at low energies, namely satellite peaks next to the low-energy peak. We perform a detailed investigation of this satellite peak in the next section.

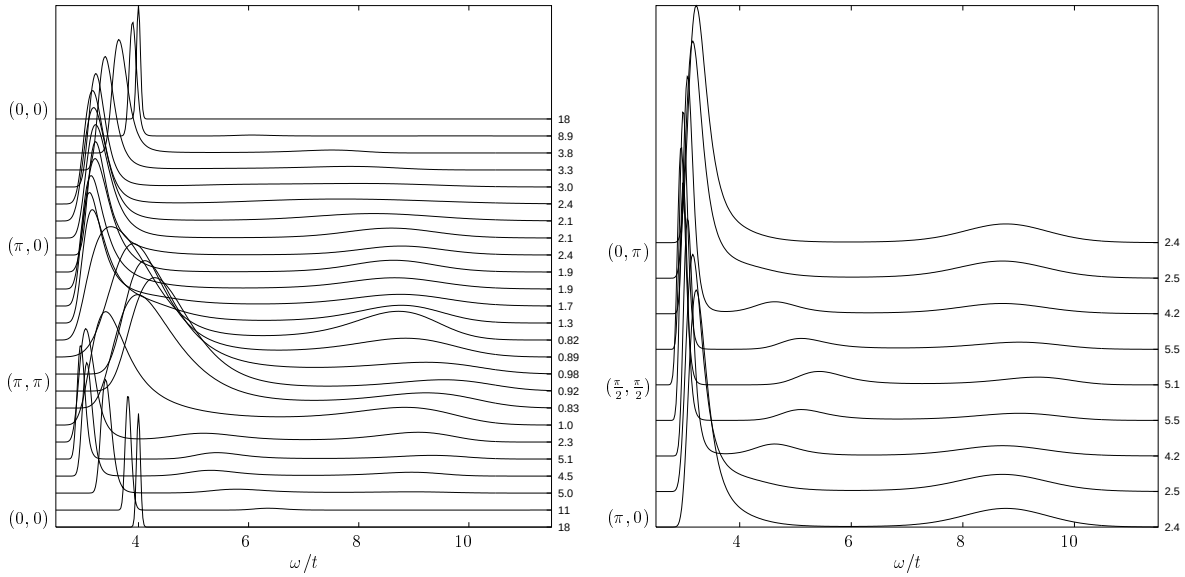


(a) (b)

Figure 4.15: Spectral function for a $16 \times 16$ system and $J/t = 2$

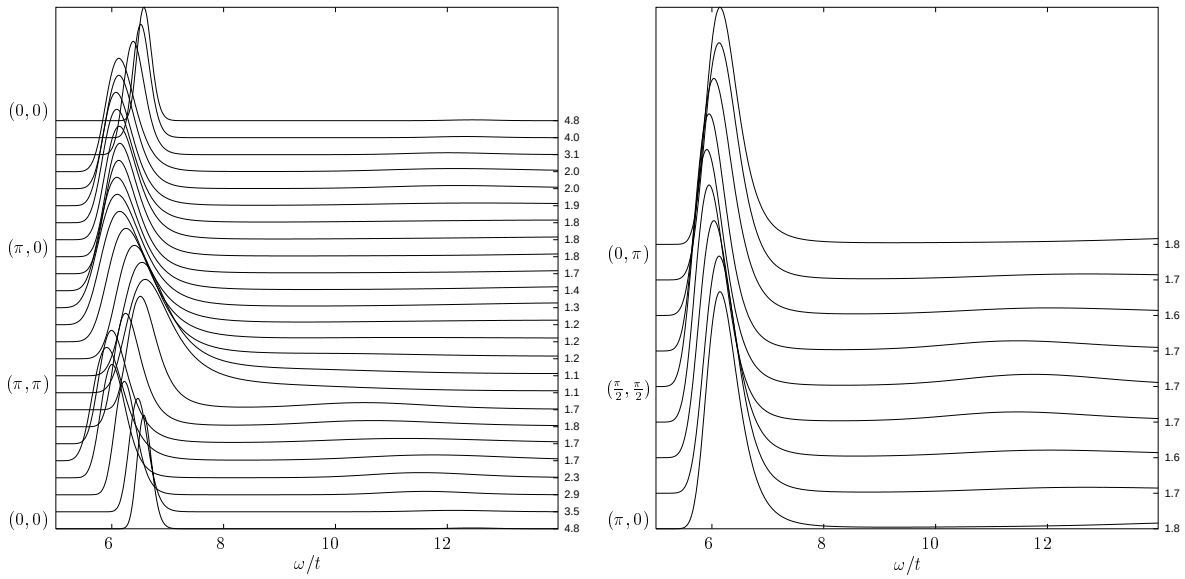


(a) (b)

Figure 4.16: Spectral function for a $16 \times 16$ system and $J/t = 4$

### 4.3.3 Excitations next to the lowest one

As can be seen above, a major part of weight is accumulated in the peak at lowest energies, which is extremely sharp. In Sec. 4.4 we will in fact show, that this peak corresponds to a quasiparticle and is thus an excitation described by a Dirac $\delta$-function. This $\delta$-peak cannot be handled satisfactorily by the *Maximum Entropy* method. As can be seen

by comparison of Figs. 4.6,4.7 and 4.11-4.16 the *Maximum Entropy* method gives some weight at energies lower than the band edge. This additional weight has to be balanced in some way, so that this error propagates to the other side of the $\delta$-peak. Small peaks in the vicinity of the $\delta$-peak can therefore not be resolved.

We solve this problem by subtracting the lowest exponential corresponding to the lowest energy as obtained in Sec. 4.3.1. The weight of this exponential is given by the quasiparticle weight discussed in Sec. 4.4. In order to prevent, that more weight is subtracted than actually is contained in the Green's function, we take the lowest possible value of the quasiparticle weight within the errors of our results. Additionally we check, if the results are insensible to small changes of the weight of the exponential within the error bars. This procedure can be done both for a single $k$-vector and for the density of states.

### String excitations

For $0.6 \leq J/t \leq 2$ we can, except for $J/t = 0.8$, observe a satellite peak next to the low-energy peak in regions of minimal hole energy in Figs. 4.11-4.16. For a better resolution of this peak, we subtract the exponential, that corresponds to the first excitation (see Fig. 4.17). As already stated above, the weight of this exponential is given by the quasiparticle weight given in Sec. 4.4. This modified Green's function can now be used as input of *Maximum Entropy*. The results are shown in Fig. 4.18. For $\mathbf{k} = (\pi/2, \pi/2)$ there are only little changes of the position of the maxima of the existing peaks at small

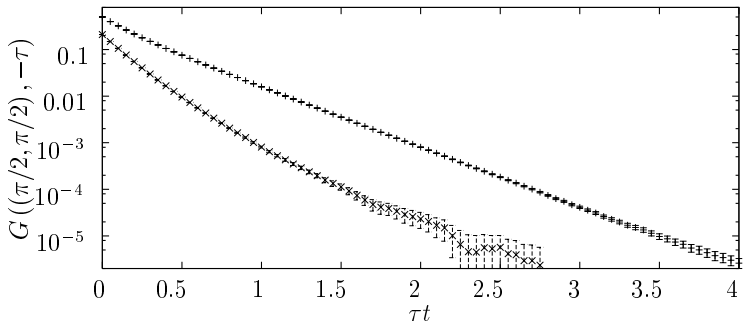


Figure 4.17: Green's function and *Green's function − first excitation* (lower curve) for a $16 \times 16$ system and $J/t = 2$ at $\mathbf{k} = (\pi/2, \pi/2)$.

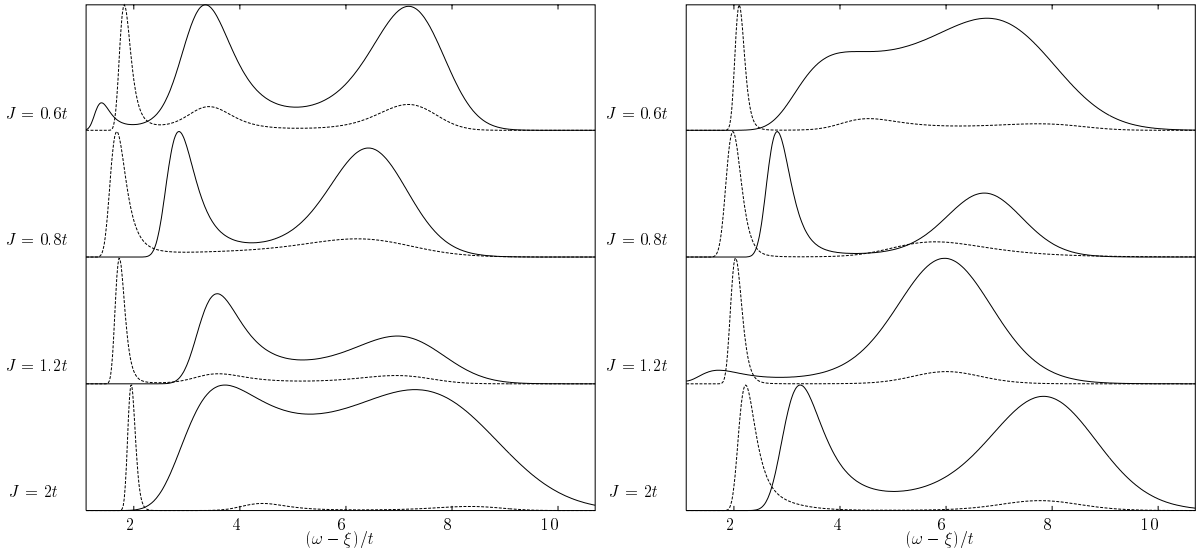


(a) $\mathbf{k} = (\pi/2, \pi/2)$ (b) $\mathbf{k} = (\pi, 0)$

Figure 4.18: Change of the spectral function when subtracting the major part of the first excitation. For $J/t = 0.8$ is is possible to resolve the second-lowest energy peak clearly, although is has been masked by the low-energy peak before. The dotted line is the original result, the full line gives the modified one. For a better resolution of the high energy peaks, the modified spectral function is rescaled, such that the maximum has the same value as the maximum of the original spectral function. For clarity, we use a different reference energies for each $J/t$ (the exact energies of the lower edge for $\mathbf{k} = (\pi/2, \pi/2)$ can be taken from Fig. 4.9 on page 59 and Fig. 4.19).

$J/t$ compared to the full spectral function (except the low-energy peak, that disappears, as we subtracted the exponential corresponding to it). We can further observe, that the satellite peak next to the low-energy peak at $\mathbf{k} = (\pi/2, \pi/2)$ can now be seen for all values of $J/t$, including $J/t = 0.8$. One should notice, that no additional weight has been produced at high energies, but the normalization has changed (again the maximal value is normalized to one, not the area of the spectral function).

At $\mathbf{k} = (\pi/2, \pi/2)$ the resolution of the second-lowest excitation is quite exact, when applying the above method, whereas at $(\pi, 0)$ the results are still not very accurate, or the string excitation is weaker. For $J/t = 1.2$ and $J/t = 0.6$ the resolution is not good enough to separate three excitations at $(\pi, 0)$. Generally the excitations at higher energies at $(\pi, 0)$ are broader than at $(\pi/2, \pi/2)$, so the positions of the maxima are not as well defined.

If the string picture is valid, as expected in the $t$-$J_z$ model (see the beginning of

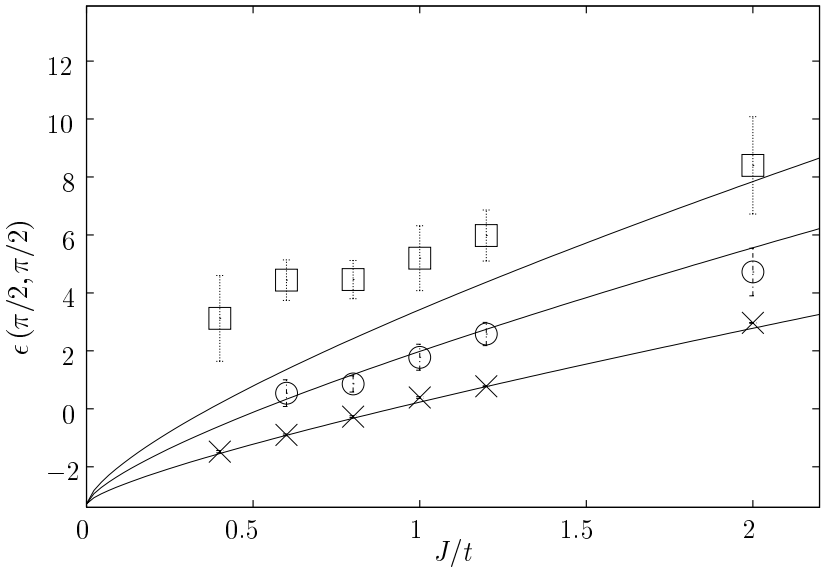


Figure 4.19: The first three excitations at $\mathbf{k} = (\pi/2, \pi/2)$. At $J/t = 0.4, 0.8$ and $J/t = 4$ only two peaks were resolved. The lines represent the solutions obtained by solving the linear string potential for the hole in the $t - J_z$ model.

this chapter and App. B), then the hole is confined by a linear potential, leading to ($k$-independent) eigenvalues of the energy [53, 54, 56, 109] given by

$$E_n/t = -2\sqrt{3} + a_n(J_z/t)^{2/3}, \tag{4.3}$$

where $a_n$ are the eigenvalues of a dimensionless Airy equation [55]. The first three eigenvalues are given by $a_n = 2.33, 4.08, 5.52$. A fit from SCBA for the first three excitations in the $t$-$J$ model for values of $J/t \leq 0.4$ results in $a_n = 2.16, 5.46, 7.81$, with the exponential of $2/3$ being kept [53]. In Fig. 4.19 the results for the first three excitations are given for $\mathbf{k} = (\pi/2, \pi/2)$, and are compared to the predictions from the string picture. The error bars on the second and third peak are obtained as the width of the *Maximum Entropy* peak at half intensity, the error bars of the first peak are taken as in Sec. 4.3.1. We find, that for $J/t \leq 2$ the lowest peak can be fitted to $-E_H - 3.28t + 2.33(J/t)^{2/3}t$, where $E_H$ is the Heisenberg energy per site, and the second peak can be fitted by $-E_H - 3.28t + 4.08(J/t)^{2/3}t$. The value of $3.28t + E_H$ is the result obtained from SCBA [53], the prefactors to $(J/t)^{2/3}$ are exactly the values of the dimensionless Airy function. This means that the first two peaks behave (within our error bars) exactly like it is expected by the string picture. Especially due to the clear $(J/t)^{2/3}$-dependence of the first and second peak, we conclude, that the string picture is a good one to describe the low-energy

physics of a single hole in the $t$-$J$ model up to very large values of $J/t \approx 2$. This is a surprising result, as the string picture is obtained in the Ising limit for $J/t \ll 1$. Further it is based on the continuum limit, which is a rather rough estimate in our case with strings of lengths between two and a maximum of five lattice points.

The third peak which can be resolved cannot be explained by the string picture, as its distance to the lower band edge is independent of $J$ and has a value of about $4t$.

At $J/t = 4$ the excitations fall below the values predicted by the string picture. In this regions the string picture is no longer valid, as the relaxation of the disturbed spin bonds is faster than the movement of the hole.

It should be noticed additionally, that the string pictures predicts a band without dispersion. This is clearly not the case in our simulations. However, the existence of a string is not only observed at the single point $(\pi/2, \pi/2)$, but also at $k$-points nearby, This is demonstrated for the value $J/t = 0.6$ (see Fig. 4.20).

Summarizing, one can notice, that remainings of the string effect can be observed for relatively large values of $J/t$. The string effect can be observed best around the point of minimal energy $\mathbf{k} = (\pi/2, \pi/2)$. Only the first two excitations can be explained in the string picture, the distance of the incoherent peak corresponding to high excitations to the lowest one is independent of $J$.

### A second look at the density of states

In the previous section, we have developed a method, that allows us to resolve small peaks, which are masked by large ones nearby. The same method can now be used for a better resolution of the density of states near the lower edge. Here we subtract two exponentials, the first one given by the lowest excitation, and the second one given by the excitation at $\mathbf{k} = (\pi, 0)$ (see Sec. 4.3.1), which has a very large weight due to the flat bands (see Fig. 4.21). The procedure of subtracting two exponentials is however less well defined than when just one exponential like for the string effect is subtracted. The fact, that the bands, although flat, consist of a number of slightly different exponentials introduces an uncontrollable error in the result of the calculation.

The results for $J/t = 0.6$ and $J/t = 1$ are shown in Fig. 4.22. For both values of $J/t$ we observe, that the gap is closed when exponentials corresponding to the lowest

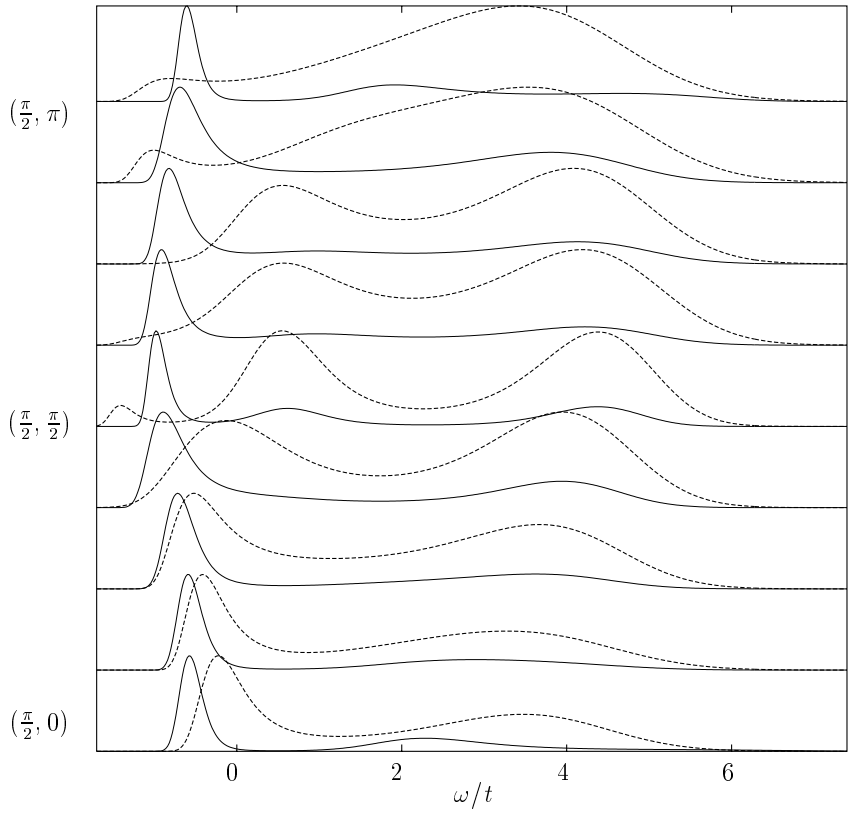


Figure 4.20: String effect, when going away from $(\pi/2, \pi/2)$. In the direction toward $(\pi/2, 0)$ the peak corresponding to the string approaches the position of the quasiparticle peak and merges with it, whereas toward $(\pi/2, \pi)$ the distance stays approximately constant. In the second case, the main effect is a broadening of the peak corresponding to the string. Shown is a $16 \times 16$ system with $J/t = 0.6$.

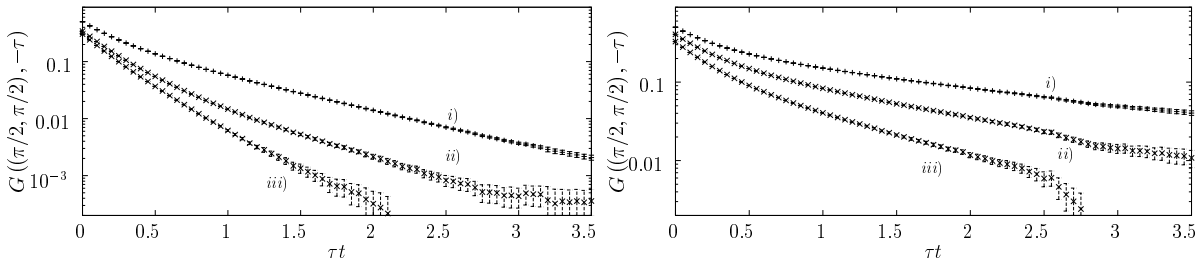


(a) $J = 0.6$ (b) $J = 1$

Figure 4.21: Original Green's function $(i)$), Green's function after subtraction of the lowest exponential $(ii)$), and after the additional subtraction of the second lowest exponential $(iii)$).

energies are subtracted from the original Green's function. Especially for $J/t = 1$ one can observe very clearly, how the lowest exponential moves continuously to lower energies, and approaches the peak at higher energies in the *original* density of states.

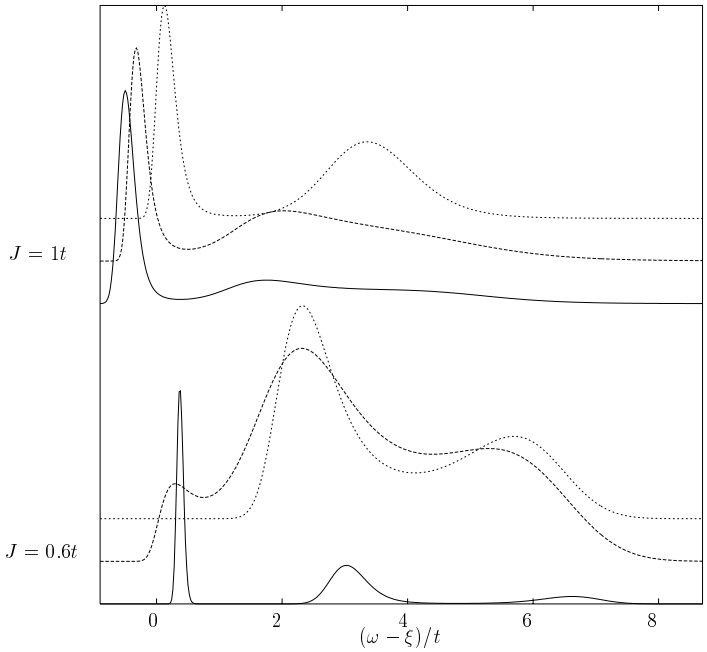


Figure 4.22: Density of states before and after subtraction the two lowest exponentials. The lowest curve corresponds to the original density, the second shows the result when subtracting the lowest exponential, and the third represents the result when an additional exponential is subtracted. It should be noticed, that we use the result, where the maximum is normalized. The area of under the peaks is proportional to the the value of $G(\tau = 0)$ in Fig. 4.21.

Although, the above procedure of subtracting two exponentials introduces a sizeable amount of noise to the original data, we conclude, especially due to the results at $J/t = 0.8$ and $J/t = 2$, where no gap is found in the density of states, that the coherent band is not gapped to the incoherent background, when the density of states in regarded.

### A remark about the reliability of the modified Green's function

When the above *Maximum Entropy* results obtained with the modified Green's function (Green's function − lowest exponential) are viewed closely, one recognizes, that sometimes an additional peak appears at low energies (this effect can be seen e.g. for $(\pi/2, \pi/2)$ in Fig. 4.20). To exclude, that this peak corresponds to a real physical effect, we take several modified Green's functions, which are consistent with the exponential of the lowest peak, which is only known up to some statistical error. So we take the lowest and the highest exponential, which is consistent with the results obtained in Sec. 4.3, and use it as input of *Maximum Entropy*.

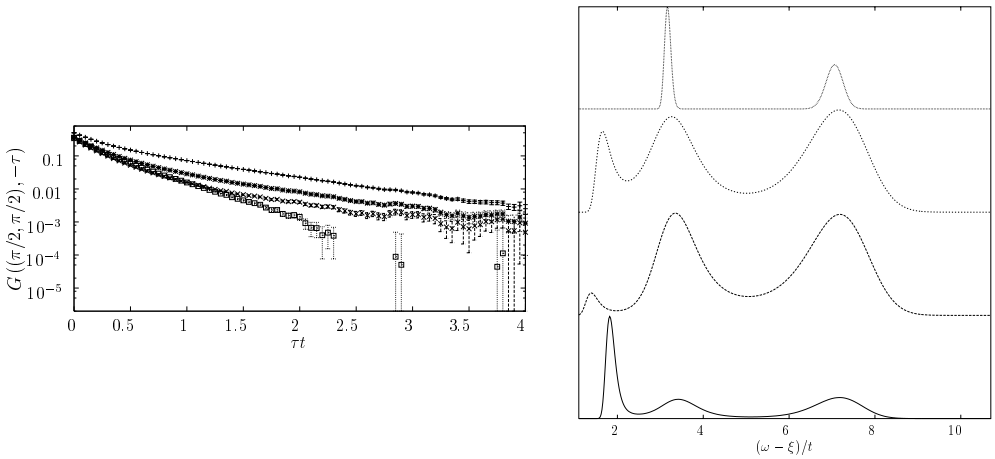


(a) Original Green's function, and three different modified functions, consistent with the exponential for the lowest energy.

(b) *Maximum Entropy* results when (a) is used as input

Figure 4.23: Green's function and resulting spectral function before and after subtraction of the lowest exponential, where the lowest exponential is within the error bars of Sec. 4.3. The results in (b) correspond (from bottom to top) to the original spectral function, to the spectral function used in Fig. 4.18, to the result when subtracting the lowest possible exponential, and to the result when the highest possible exponential is subtracted. The error bar an the exponential is $0.03t$, the error on its weight is 0.025.

As can be seen in Fig. 4.23, the peak, which appeared below the low-energy peak of the original function is only observed in one case, whereas the two other peaks can be observed in all cases, no matter what exponential is subtracted within the error bars. We conclude, that the low-energy peak is artificially introduced by subtracting exponentials, that are not quite the exact ones, introducing a systematic error in the low-energy spectrum. As can be seen, the high-energy peaks are not shifted significantly, however changes in the width can be observed.

### 4.3.4 Finite-size effects on the spectral function

Both our calculations and simulations by GFMC have shown, that the size dependence for the lowest energies given some $k$-vector are small above systems of size $8 \times 8$. The $4 \times 4$ systems however, that can be handled by exact diagonalizations, are pathological, as $\mathbf{k} = (\pi/2, \pi/2)$ and $\mathbf{k} = (\pi, 0)$ are topological the same points. This can be observed directly in the QMC data (see Fig. 4.24).

As we can see in Fig. 4.25 the complete spectral function given a particular point in

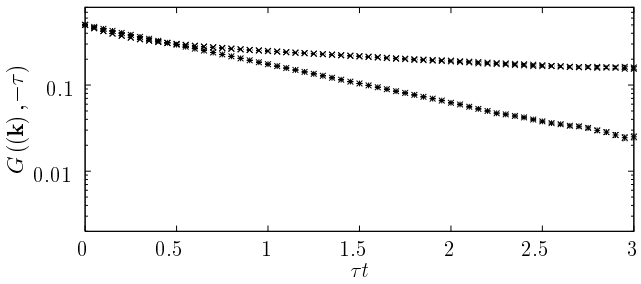


Figure 4.24: Green's function in a $4 \times 4$ system for $\mathbf{k} = (\pi/2, \pi/2)$, $\mathbf{k} = (\pi, 0)$ (the two upper curves lie one upon the other) and $\mathbf{k} = (0, 0)$ (lower curve) for comparison.

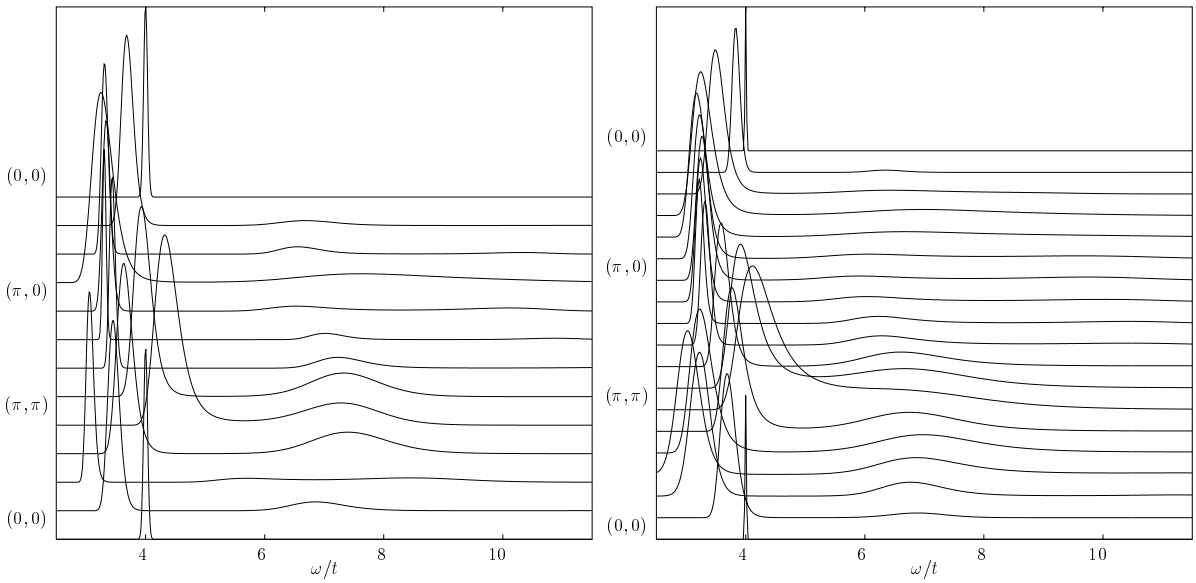


(a) $8 \times 8$ lattice (b) $12 \times 12$ lattice

Figure 4.25: Finite-size effects in the square lattice demonstrated for $J/t = 2$.

the Brillouin zone changes only little with size, once large enough systems are reached $(8 \times 8)$. However it is important to notice, that the finite-size effects on the quasiparticle weight are not at all negligible, as we will see in the next chapter.

## 4.4 The quasiparticle weight

Like in the one-dimensional case, the quasiparticle weight can be calculated as the weight of the exponential with the slowest decay, that is the exponential corresponding to the lower edge of the spectrum.

Variational results [50], SCBA [52] and exact diagonalizations [47, 49] predict a finite quasiparticle weight in two dimensions, that increases with $J/t$. However, in the variational calculations, there is no estimate of how accurate the results are, and in fact there is often a difference from exact results in $4 \times 4$ systems, that is well beyond the statistical error. Exact diagonalizations on the other hand suffer extremely from finite-size effects especially for this quantity. To do a finite-size scaling for the point $\mathbf{k} = (\pi/2, \pi/2)$ one has to use points that are nearby, otherwise only the $4 \times 4$ system contains that point in the Brillouin zone, and as already stated before, this point is identical to $(\pi, 0)$ at this system size. Thus strictly speaking a finite-size scaling for the most interesting point of minimal energy is not possible at all, when doing exact diagonalization studies.

### 4.4.1 The quasiparticle weight for $k$-points along the symmetry axes

An obvious question when investigating the quasiparticle weight is its value for different $k$-points. We will discuss the two case $J/t = 2$ and $J/t = 0.6$

#### The supersymmetric point $J/t = 2$

We start our discussion with a special case, the supersymmetric point. At the supersymmetric point S. Sorella was the first to notice, that at $\mathbf{k} = (0, 0)$, the quasiparticle weight is maximal [44]. In this work we give another proof of this fact, obtained by a completely different approach (see App. A). A further suggestion of S. Sorella's work is a jump in the quasiparticle weight given by

$$\frac{Z\big(\mathbf{k} + (\pi, \pi)\big)}{Z(\mathbf{k})} \approx (2m)^2 = 0.37 \tag{4.4}$$

in the thermodynamic limit, where $m$ is the antiferromagnetic order parameter. The magnetic order parameter is $m \approx 0.305$ [113] in the thermodynamic limit, and $m \approx 0.34$ for $N = 24 \times 24$ [20]. For this system size, we calculated the quasiparticle weight for all $k$-points along the symmetry axis (see Fig. 4.26.a). The ratio of $Z(\pi, \pi)$ and $Z(0, 0)$ fulfills eq.(4.4) in a $24 \times 24$ system

$$\frac{Z(\pi, \pi)}{Z(0, 0)} \leq (2m)^2 \approx 0.45, \tag{4.5}$$

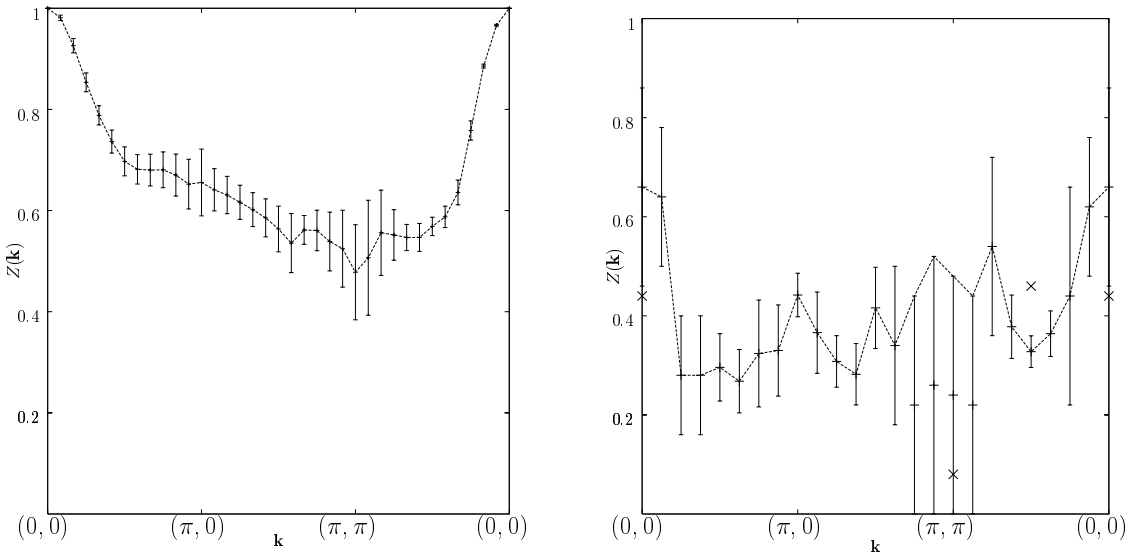


(a) $J = 2t$ (b) $J = 0.6t$

Figure 4.26: The quasiparticle weight $Z(\mathbf{k})$ for a $24 \times 24$ system for $J/t = 2$, and a $16 \times 16$ system for $J/t = 0.6$. In (b) results from exact diagonalization are given for comparison ($\times$). The results of exact diagonalization were interpolated between results for $J/t = 0.5$ and $J/t = 1$ for $\mathbf{k} = 0$ and $\mathbf{k} = (\pi, \pi)$ ($\sqrt{26} \times \sqrt{26}$-system) [49] resp. between $J/t = 0.55$ and $J/t = 0.7$ for $\mathbf{k} = (\pi/2, \pi/2)$ ($4 \times 4$-system) [47].

however $Z(\mathbf{k})$ seems to be continuous, when crossing the magnetic Brillouin zone at $(\pi/2, \pi/2)$ and $(\pi, 0)$. We observe a steep continuous drop of the quasiparticle weight when going away from $(0, 0)$ and a rather constant behavior in all other regions of the Brillouin zone. The overall features of the quasiparticle weight should not change too much, when going to the thermodynamic limit, at least it is not the case, for $Z(\pi/2, \pi/2)$ and $Z(\pi, 0)$. A finite-size scaling for the other points is often not possible as they are not contained in the Brillouin zone for smaller systems.

### Small values of $J/t$

For $J/t = 0.6$ it is already known from exact diagonalization, that the quasiparticle weight behaves quite differently from $J/t = 2$.

In a $4 \times 4$ system, the quasiparticle weight at $\mathbf{k} = (\pi, 0)$ and $(\pi/2, \pi/2)$ is about 0.47 [47, 48], whereas at $(\pi, \pi)$ it drops to about 0.10. At $(0, 0)$ the quasiparticle weight has a value of about 0.4 (obtained in a $\sqrt{26} \times \sqrt{26}$ lattice [49]). From our QMC simulations accurate results can only be obtained around $(\pi/2, \pi/2)$ and $(\pi, 0)$, at all other points,

the Green's function cannot be fitted by a single exponential for the values of $\tau t$ we can reach in our simulations. For the other points we can therefore only give an upper bound. The procedure to do so will be shown below.

The results for $J/t = 0.6$ are given in Fig. 4.26.b. It can be seen, that the quasiparticle weight around the minimum of the band (including the flat band around $(\pi, 0)$) remains approximately stable. The quasiparticle weight at $(\pi/2, \pi/2)$ and at the local minima around $(\pi, 0)$ is about 0.1 smaller than exactly at $(\pi, 0)$. The upper bound that we can give for $(\pi, \pi)$ is much larger than the result from exact diagonalization, and can therefore not give any new information about the system. The same is true for the $(0, 0)$-point, where our result suffers from very large error bars.

At $J/t = 0.4$ and $\Delta\tau = 0.05$, the Green's function at $\mathbf{k} = (\pi/2, \pi/2)$ and $(\pi, 0)$ suffers from a relatively large error, and thus we cannot decide, if the Green's function already approaches a single line on a logarithmic scale[2]. If we only take the very last points in $\tau t$ of the Green's function the resulting errors of the least square fit are extremely large. When additional points below $\tau/t = 2.5$ are included, the error bars are reduced drastically, however the measured quasiparticle weight is systematically too large, when the starting point in $\tau$ is chosen too small. Nevertheless, by adding one point after the other, we find $Z(\pi/2, \pi/2) \leq 0.28 \pm 0.04$ and $Z(\pi, 0) \leq 0.32 \pm 0.05$ as an upper bound in a $16 \times 16$ lattice. The result of exact diagonalization in a $4 \times 4$ lattice is 0.4. Thus our results give a new upper bound for the quasiparticle weight at $J/t = 0.4$ both for the point $\mathbf{k} = (\pi, 0)$ and for $(\pi/2, \pi/2)$. All other points in the Brillouin zone suffer from even larger error bars, so that we were not able to give the quasiparticle weight for all the points in the Brillouin zone.

### 4.4.2 The dependence of the quasiparticle weight on $J/t$

#### Finite-size scaling for the quasiparticle weight at $(\pi/2, \pi/2)$ and $(\pi, 0)$

Next we consider the thermodynamic limit for the $k$-points $\mathbf{k} = (\pi, 0)$ and $\mathbf{k} = (\pi/2, \pi/2)$. Fig. 4.27 and Fig. 4.28 show the finite-size scaling for these two points. They both have a large quasiparticle weight, and the difference of $Z(\mathbf{k})$ between the two points is small

[2]When one chooses $\Delta\tau t = 0.2$, the number of points is not sufficient for a reasonable least square fit, although the maximal $\tau t$ that can be reached is increased.

but finite.

The determination of the quasiparticle weight is only possible at $J/t \geq 0.6$. Below that value, the quality of the data is no longer sufficient to estimate the quasiparticle weight, however we give the upper bound for $J/t = 0.4$ as obtained in the previous section for a $16 \times 16$ lattice[3].

We perform a finite-size scaling for each value of $J/t$ separately. The size dependence of $Z(\pi/2, \pi/2)$ and $Z(\pi, 0)$ is not very large and has a linear behavior with the inverse linear size of the system, in agreement with SCBA [52]. The size dependence at $(\pi/2, \pi/2)$ is systematically larger than at $(\pi, 0)$. The lattices that were considered for the scaling are of size $16 \times 16$, $12 \times 12$, $8 \times 8$ and $4 \times 4$. At $J/t = 2$ we use additionally the $24 \times 24$ lattice. Values from exact diagonalization [47–49] were included when available.

### The quasiparticle weight in the thermodynamic limit

From the finite-size scaling, we obtain the value of the quasiparticle weight in the thermodynamic limit. One can see, that the quasiparticle weight increases with $J/t$ both for $\mathbf{k} = (\pi, 0)$ and $\mathbf{k} = (\pi/2, \pi/2)$ (Fig. 4.29). At $J/t = 4$ the quasiparticle reaches

[3] A finite-size scaling of an upper bound is not reasonable.

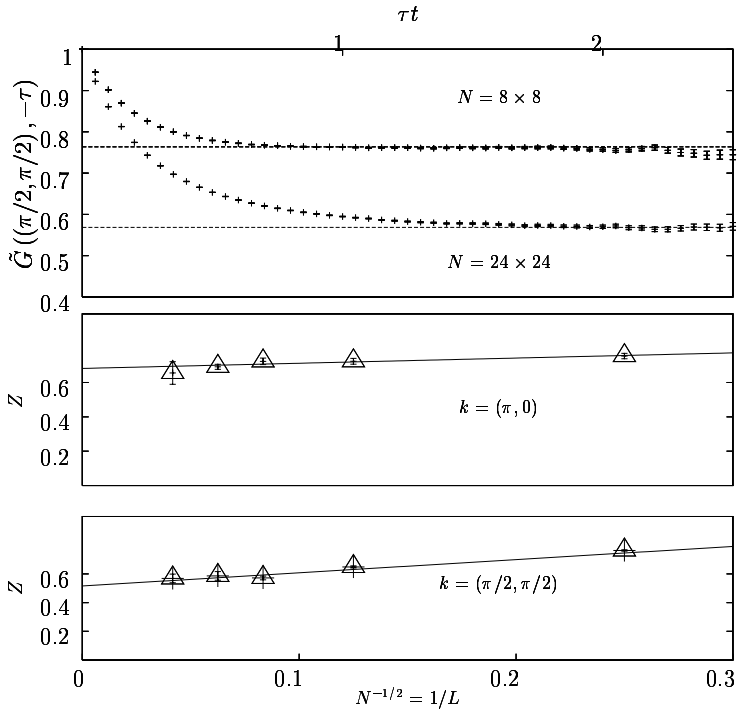


Figure 4.27: Finite-size scaling for $J/t = 2$ and $\mathbf{k} = (0, 0)$ and $\mathbf{k} = (\pi, 0)$.

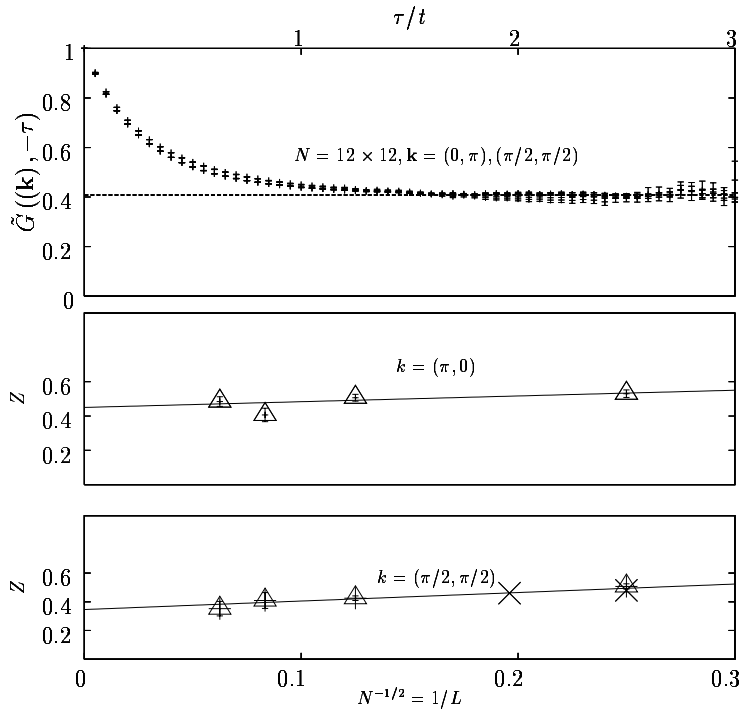


Figure 4.28: Finite-size scaling for $J/t = 0.6$ and $\mathbf{k} = (\pi/2, \pi/2)$ and $\mathbf{k} = (\pi, 0)$. The crosses are values interpolated from exact diagonalization results [47, 49].

about 80% of its maximal value. The quasiparticle weight at $(\pi/2, \pi/2)$ (the point with minimal energy) is always smaller than or equal to its value at $(\pi, 0)$. The changes of the quasiparticle weight with $J/t$ are small when $J/t \leq 1$ and the slope becomes steeper when approaching smaller values. Besides variational Monte Carlo [50], SCBA [52] is capable to give estimates about the quasiparticle weight. In Fig. 4.30 we compare our results at $16 \times 16$ to those of SCBA. We find, that the behavior is similar. It is especially interesting, that like in our case $Z(\pi, 0) > Z(\pi/2, \pi/2)$ for all considered values of $J/t$. At small values of $0.01 \leq J/t \leq 0.5$ SCBA find a scaling of $Z(\pi/2, \pi/2) = 0.63J^{2/3}$ resp. $Z(\pi, 0) = 0.71J^{0.7}$. For $J/t \leq 1$, the results from SCBA overestimate the quasiparticle weight at the two considered $k$-points. At $J/t = 2$ and $\mathbf{k} = (0, 0)$ on the other hand, the quasiparticle weight is underestimated by SCBA. The result of SCBA is approximately 0.9 instead of exactly 1 at this point. Based on the qualitatively good agreement of our results with those of SCBA we conclude, that this is approximately the correct scaling for this parameter range at $16 \times 16$ sites. By inspecting the results of the finite-size scaling, one finds, that the qualitative behavior does not change in the thermodynamic limit.

Based on that, the quasiparticle at $\mathbf{k} = (0, \pi)$ and $(\pi/2, \pi/2)$ should be finite for all

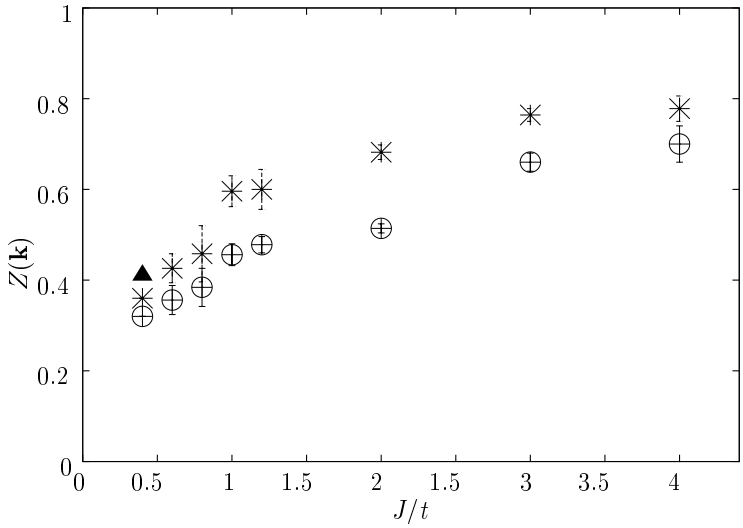


Figure 4.29: The quasiparticle weight for different values of $J/t$ for $\mathbf{k} = (\pi/2, \pi/2)$ (circles) and $\mathbf{k} = (\pi, 0)$ ($\times$). For $J/t = 0.4$ we can only give un upper bound for the quasiparticle weight. The result from exact diagonalization [47] in a $4 \times 4$ lattice is represented by the triangle.

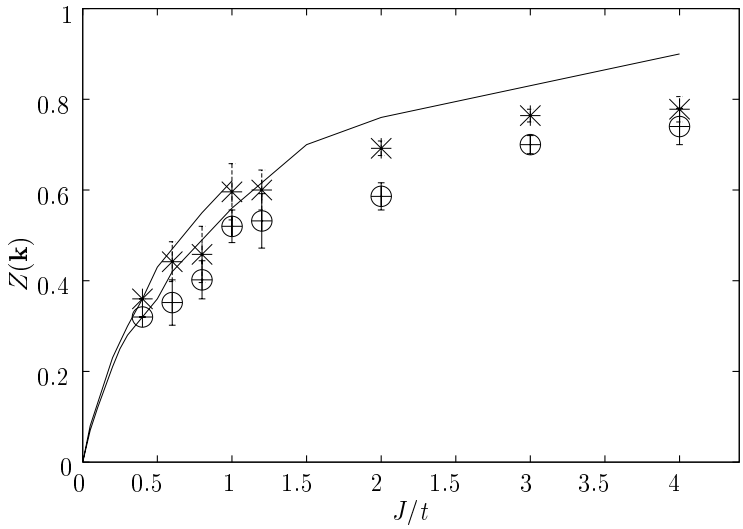


Figure 4.30: The quasiparticle weight for different values of $J/t$ for $\mathbf{k} = (\pi/2, \pi/2)$ (circles) and $\mathbf{k} = (\pi, 0)$ ($\times$) in a $16 \times 16$ lattice. For $J/t = 0.4$ we can only give un upper bound for the quasiparticle weight. We compare our result with SCBA, where the upper line corresponds to the quasiparticle weight for $\mathbf{k} = (\pi, 0)$ and the lower curve represents $\mathbf{k} = (\pi/2, \pi/2)$. The data points were taken from Ref. [52].

values of $J/t > 0$ in the thermodynamic limit.

| $J/t$ | $Z$ | $W_1$ | $W_2$ | $W_2/Z$ | $W_2/W_1$ | $W_H$ |
|---|---|---|---|---|---|---|
| 0.6 | 0.35 | 0.33 | 0.23 | 0.66 | 0.69 | 0.39 |
| 0.8 | 0.43 | 0.43 | 0.16 | 0.37 | 0.37 | 0.43 |
| 1.0 | 0.50 | 0.54 | 0.23 | 0.46 | 0.42 | 0.24 |
| 1.2 | 0.52 | 0.46 | 0.24 | 0.46 | 0.52 | 0.24 |
| 2.0 | 0.59 | 0.57 | 0.16 | 0.27 | 0.28 | 0.25 |

Table 4.1: Dependence of the quasiparticle weight $Z$, the weight of the first peak $W_1$, the weight of the second peak $W_2$ and its ratios on $J/t$. All results are taken at $\mathbf{k} = (\pi/2, \pi/2)$.

### 4.4.3 The weight of the first string excitation

Finally, we compare the quasiparticle weight to the weight of the first string excitation. When considering the results above (see Fig. 4.12-4.15), one could think, that the weight of the string excitation is much smaller than the weight of the lowest peak. In the following we will check, whether this is fulfilled, and if there is some systematic dependence of the ratio of these two peaks on $J/t$. In Table 4.1 we show the quasiparticle weight $Z$, the weight in the first peak $W_1$, resulting from the *Maximum Entropy* method, the weight of the second peak $W_2$, when the modified Green's function is used, the two ratios $W_2/Z$ and $W_2/W_1$, and the rest of weight at higher energies. All values are taken at $\mathbf{k} = (\pi/2, \pi/2)$ in a $16\times16$ lattice. The quasiparticle weight is taken as defined in the previous section, $W_1$ is the accumulated weight from $\omega/t = -\infty$ to the point, where the first peak falls down to a quarter of its maximum value. $W_2$ is either defined like $W_1$, or when the peak is not falling down to small enough values, we take the minimum between the string peak and the high energy peak. When a small artefact of the quasiparticle peak is remaining, we subtract its weight form $W_2$. The high energy weight $W_H$ is taken as all the weight, above $W_2$, measured from the modified Green's function. As $W_1$ is measured from the original Green's function, whereas $W_2$ and $W_H$ is taken from the modified Green's function, the sum of all three weights does not account to exactly one.

A comparison of $Z$ and $W_1$, that are expected to be the same, give a relative error for $W_1$ of about 10%. When we assume, that $W_2$ has about the same relative error, we end up with a relative error of about 25% for $W_2/Z$ and 35% for $W_2/W_1$. It is therefore difficult to conclude about the dependence of the ratios on $J/t$.

The results show that the weight $W_2$ is always smaller than $Z$, but we find, that it is

about the same order. This result shows, that the inspection of *Maximum Entropy* results alone can be misleading, especially when singularities in the spectral function occur.

Our data further suggests, that the gain of weight in the low-energy peak at $\mathbf{k} = (\pi/2, \pi/2)$ is at the expense of the high energy peak and of the string peak at the same time. The transfer of weight to the quasiparticle seems to be smooth with $J/t$.

# Chapter 5

# A single hole in the two-leg ladder

## 5.1 Ladder systems as a bridge from one to two dimensions

The ladder systems can be considered as a bridge between one-dimensional chains and two-dimensional planes. The crossover from the chain to the plane is not smooth at all [57–59], but a strong odd-even effect can be observed. At half filling the major difference is the existence of a spin gap for even-leg ladders (i.e. the lowest spin excitation has a finite energy in the thermodynamic limit) and its absence for odd-leg ladders, including the single chain. For two-leg ladders, a speculative phase diagram has been determined both for the weak-coupling Hubbard model [114] and for the $t$-$J$ model [115, 116]. They both found, that the low doping limit falls into the Luther-Emery region with a spin gap like at exactly half filling [117, 118] and a gapless charge excitation. In addition to being an interesting system on its own, the two-leg ladder at half filling is a realization of a spin-liquid state [3, 119, 120], whose understanding is a key issue for the theory of high-temperature superconductors.

Realizations of ladders can be found in different materials. Well known examples are cuprate compounds like $Sr_xCu_yO_z$. Depending on their actual composition, these compounds can build chains ($SrCuO_2$ [11]), two-leg ladders ($SrCu_2O_3$ [121]) and three-leg ladders ($Sr_2Cu_3O_5$ [122]). Further examples can be found in the review articles by T. M. Rice and E. Dagotto [57–59].

The ground state of a Heisenberg antiferromagnet on a two-leg ladder differs considerably both from the ground state of the chain and of the two-dimensional case. As stated above, one main difference is the existence of a spin gap in the two-leg ladder, which is absent in two dimensions and in the single chain. The spin gap exits for all finite values of $J_y/J_x$, where $J_y$ is the coupling between the chains, and $J_x$ is the coupling along the chain [117, 118, 123–127].

## 5.2 Exactly solvable limits

Before presenting our results, we discuss two simple limits, where exact results are available. The fully polarized state can be used to define the two bands in the two-leg ladder, the bonding and the antibonding one. From the limit of strong coupling along the rungs and weak coupling along the chain, one obtains pertubative results which are qualitatively correct up to the isotropic case.

### 5.2.1 The ferromagnetic limit

In the ferromagnetic limit (i.e all spins are aligned in one direction) the two-leg ladder can be easily solved exactly. In the direction along the ladder ($x$-direction), the chains are considered to have periodic boundary conditions. The boundaries in the direction across the ladder ($y$-direction) are taken as open. It is important to notice, that open boundaries in $y$-direction are equivalent to periodic boundary conditions in this direction when the coupling between the two chains is halved.

The Fourier transform in $y$-direction leads to two $k_y$-points, resulting in two bands with $\mathbf{k} = (k_x, \pi)$ and $\mathbf{k} = (k_x, 0)$ respectively. In the first case the contributions of the two chains to the Green's function are subtracted from each other (antibonding band), in the other case they are added up (bonding band).

In Fig. 5.1 the free hole in the ferromagnetic background is shown. When $t_x = 0$, the two bands are flat and splitted by $2t_y$, when $t_x$ is switched on one obtains two $2t_x \cos(k_x)$ bands. It can be seen, that the results of the QMC simulations are exactly lying on the analytic result. The energies of the QMC simulations were obtained by fitting a single exponential to the Green's function (see Sec. 4.3). In the case of free holes, the Green's

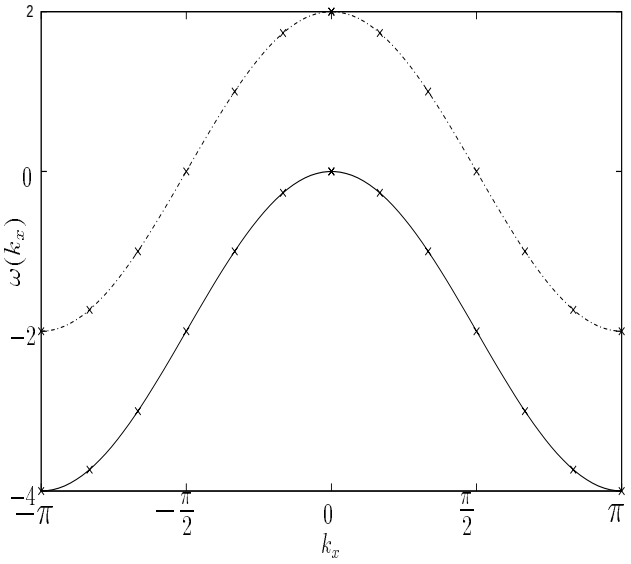


Figure 5.1: The dispersion of the holes in the two bands of a two leg ladder, when the spins are ferromagnetically ordered. The crosses shows the results of the QMC algorithm, produced by fitting the Green's function to an exponential. The lines show the two $2t\cos(kx) + \Delta$ bands. For electrons, the sign of the dispersion changes, so that the minimum in that case is at $k_x = 0$ as expected for the free case.

function consists of only one single exponential.

### 5.2.2 The strong coupling limit

To discuss the effects of antiferromagnetic correlations, we investigate another limit, the limit $J_y, t_y \gg J_x, tx$. The two-leg ladder can then be understood as a chain of singlets (Fig. 5.2) on the rungs, which interact weakly. The spectral function in the case $t_x = J_x = 0$ is given by [63, 128]

$$A(0,\omega) = \frac{1}{2\pi}\delta\big(\omega - (t_y - J_y)\big)$$
$$A(\pi,\omega) = \frac{1}{2\pi}\delta\big(\omega - (-t_y - J_y)\big), \tag{5.1}$$

leading to an energy splitting between the two excitations of $2t_y$. These two excitations can be resolved by our QMC simulations (see Fig. 5.3).

The two single excitations of eq.(5.1) start forming dispersing bands when interactions along the chains are considered. In the strong coupling limit, the resulting dispersion can be easily obtained following the work of Endres *et al* [60–63] in the electron picture of the original $t$-$J$ model (1.2).

The ground state of a ladder, where $J_y \gg J_x$ is approximately given by

$$|\,\Psi_0\,\rangle = |\,\mathcal{S}_1\,\rangle\,|\,\mathcal{S}_2\,\rangle \ldots |\,\mathcal{S}_L\,\rangle\,, \tag{5.2}$$

where $L$ is the length of the system, and the singlets on the rungs are given by

$$|\,\mathcal{S}_i\,\rangle = 1/\sqrt{2}\big(c^\dagger_{i,1,\uparrow}c^\dagger_{i,2,\downarrow} - c^\dagger_{i,1,\downarrow}c^\dagger_{i,2,\uparrow}\big)\,|\,v\,\rangle\,. \tag{5.3}$$

The state of a single electron (we choose spin $\uparrow$) on a rung is given by

$$\big|\,\Psi^b\,\big\rangle = 1/\sqrt{2}\big(c^\dagger_{i,1,\uparrow} + c^\dagger_{i,2,\uparrow}\big)\,|\,v\,\rangle \tag{5.4}$$

for the bonding case, and

$$|\,\Psi^a\,\rangle = 1/\sqrt{2}\big(c^\dagger_{i,1,\uparrow} - c^\dagger_{i,2,\uparrow}\big)\,|\,v\,\rangle \tag{5.5}$$

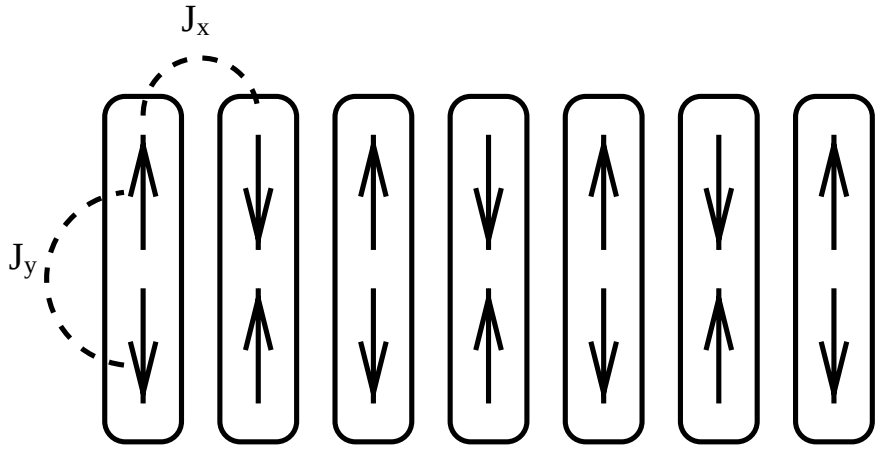


Figure 5.2: The strong coupling limit of a two-leg ladder. As $J_y \gg J_x$, the physics can be well understood by singlets on the rung, that interact weakly along the $x$-direction.

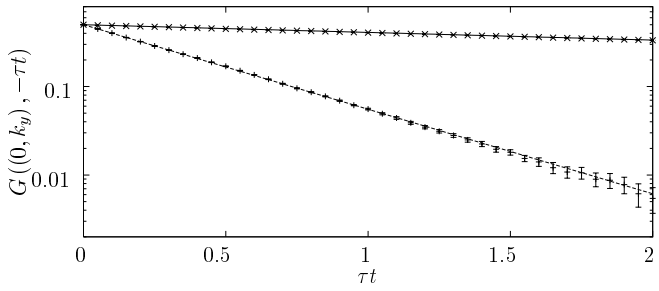


Figure 5.3: Green's function for the bonding and antibonding states on a single rung with $J_y/t_y = 1.2$ and $J_x = t_x = 0$. The upper curve corresponds to the bonding state, the lower curve to the antibonding state. The slope on a logarithmic scale is $-(J_y - t_y) = -0.2t_y$ and $-(J_y + t + y) = -2.2t_y$ corresponding to the negative energy difference to the Heisenberg antiferromagnet.

for the antibonding case. The state of a single hole (i.e one electron is missing) on a chain can now be expressed by

$$\left| \Psi \, {}^{B}_{A} \right\rangle = 1/\sqrt{L} \sum_{l=1}^{L} \exp(ikl) \left| l \, {}^{b}_{a} \right\rangle, \tag{5.6}$$

where

$$\left| l \, {}^{b}_{a} \right\rangle = |\, \mathcal{S}_1 \,\rangle \ldots |\, \mathcal{S}_{l-1} \,\rangle \left| \Psi \, {}^{b}_{a} \right\rangle |\, \mathcal{S}_{l+1} \,\rangle \, |\, \mathcal{S}_L \,\rangle \,. \tag{5.7}$$

The Hamiltonian for a single rung is given by the two-site $t$-$J$ model

$$H_0 = -t_y \sum_{i,\sigma} \Big( \tilde{c}^{\dagger}_{i,1,\sigma} \tilde{c}_{i,2,\sigma} + \tilde{c}^{\dagger}_{i,2,\sigma} \tilde{c}_{i,1,\sigma} \Big) + J_y \sum_{<i,j>} \Big( \vec{S}_i \cdot \vec{S}_j - 1/4 n_i n_j \Big), \tag{5.8}$$

the $x$ direction is approximated by the hopping of electrons, where the constraint of no double occupancy is enforced explicitly

$$H_i = -t_x \sum_{i,j,\sigma} \Big( \tilde{c}^{\dagger}_{i,1,\sigma} \tilde{c}_{j,1,\sigma} + \tilde{c}^{\dagger}_{i,2,\sigma} \tilde{c}_{j,2,\sigma} + h.c \Big). \tag{5.9}$$

Now one can calculate the dispersion by

$$\begin{aligned}
\omega(k_x) &= \langle\, \Psi_0 \,|\, H_0 + H_i \,|\, \Psi_0 \,\rangle - \left\langle \Psi \, {}^{B}_{A} \right| H_0 + H_i \left| \Psi \, {}^{B}_{A} \right\rangle = \\
&= -LJ_y - (L-1)J_y \mp t_y - 2t_x \cos(k_x) \times \\
&\times 1/4 \, \langle\, v \,|\, (c^{\dagger}_{i,1,\uparrow} c^{\dagger}_{i,2,\downarrow} - c^{\dagger}_{i,1,\downarrow} c^{\dagger}_{i,2,\uparrow})(c^{\dagger}_{j,1,\uparrow} \pm c^{\dagger}_{j,2,\uparrow})(\tilde{c}^{\dagger}_{i,1,\sigma} \tilde{c}_{j,1,\sigma} + \tilde{c}^{\dagger}_{i,2,\sigma} \tilde{c}_{j,2,\sigma}) \\
&\times (c^{\dagger}_{j,1,\uparrow} c^{\dagger}_{j,2,\downarrow} - c^{\dagger}_{j,1,\downarrow} c^{\dagger}_{j,2,\uparrow})(c^{\dagger}_{i,1,\uparrow} \pm c^{\dagger}_{i,2,\uparrow}) \,|\, v \,\rangle = \\
&= J_y \mp t_y - t_x \cos(k_x).
\end{aligned} \tag{5.10}$$

The only effect of the noninteracting singlets one the hole dynamics compared to the free ferromagnetic case, is a rescaling of the hopping $t_x$ by a factor of $1/2$, and a shift in energy of $J_y$.

When $J_x$ is switched on, the singlets on the rungs begin to order, leading to a further decrease in the effective hopping in $x$-direction. This can be seen by considering the overlap

$$\begin{aligned}
&\left\langle \Psi \, {}^{B}_{A} \right| H_i \left| \Psi \, {}^{B}_{A} \right\rangle = \\
&= \frac{t_x}{2} \cos(k_x) \, \langle\, v \,|\, (\alpha c^{\dagger}_{i,1,\uparrow} c^{\dagger}_{i,2,\downarrow} - \beta c^{\dagger}_{i,1,\downarrow} c^{\dagger}_{i,2,\uparrow})(c^{\dagger}_{j,1,\uparrow} \pm c^{\dagger}_{j,2,\uparrow})(\tilde{c}^{\dagger}_{i,1,\sigma} \tilde{c}_{j,1,\sigma} + \tilde{c}^{\dagger}_{i,2,\sigma} \tilde{c}_{j,2,\sigma}) \times \\
&\qquad \times (\beta c^{\dagger}_{j,1,\uparrow} c^{\dagger}_{j,2,\downarrow} - \alpha c^{\dagger}_{j,1,\downarrow} c^{\dagger}_{j,2,\uparrow})(c^{\dagger}_{i,1,\uparrow} \pm c^{\dagger}_{i,2,\uparrow}) \,|\, v \,\rangle = 2\alpha\beta.
\end{aligned} \tag{5.11}$$

As $\alpha\beta$ ($0 \leq \alpha, \beta \leq 2$, $\alpha+\beta = 2$) is expected to decrease when short range order along the chain sets in, the dispersion is reduced, when the coupling along the chain is increased. As the spin gap in units of $J_x$ given by $\Delta/J_x \sim J_y/J_x$ decreases when $J_x$ increases, and therefore the spin-spin correlation between two neighboring rungs increases, the effective hopping should decrease with $J_x/J_y$.

The strong coupling limit can be used as a starting point for pertubative or variational calculations [64, 120], that seem to work well up to the isotropic limit. Comparison to the analytical results of O. P. Sushkov [64], who derived an analytical form for the lower edge of the spectrum, will be made where possible.

## 5.3 The spectral function

In this section we discuss the spectral function both for the anisotropic and for the isotropic case.

In all cases we give the lower edge of the bonding and antibonding band (see Figs. 5.4, 5.5, 5.8, 5.10, 5.11, and 5.12) and the full spectral function (see Figs. 5.6, 5.7, 5.9, 5.13, 5.14, and 5.15). For the full spectral function we give the bonding and the antibonding band in a separate figure, with the physical normalization of the area $\int_{-\infty}^{+\infty} d\omega A(\mathbf{k},\omega) = \pi/2$. Additionally, we give both bands together in one figure, with the maximum of $A(\mathbf{k},\omega)$ for a fixed $\mathbf{k}$ normalized to 1, i.e we show $\frac{A(\mathbf{k},\omega)}{\max[A(\mathbf{k},\omega)]}$ as a function of $\omega/t$. In the first case, the distribution of weight can be better observed, in the second case, it is easier to follow the overall structures. Especially it can be seen directly, at which $k$-points the bonding band and the antibonding band cross. The unit of energy for the following discussion is taken as $t \equiv t_x$, when not given explicitly. All energies are measured relative to the Heisenberg ground state of the ladder, i.e. the Heisenberg ground state energy is fixed at $\omega/t = 0$.

Excellent results for the lower edge of the spectrum were obtained from series expansion [65]. Unfortunately these results are only available for $J_y/J_x \geq 1$ and no information about the weight of the low-lying excitations, the quasiparticle excitations neither of the excitations at higher energies are available from this method. We show the results from series expansion at the end of this section in Fig. 5.16 on page 100.

### 5.3.1 The anisotropic case

We start the discussion of our results with the anisotropic case $J_y \neq J_x$. In this case there are four different free parameters in the $t$-$J$ two-leg ladder. As stated above, we choose the hopping along the chain $t_x$ to be the unit of energy. One possible connection between the parameters can be achieved when one uses the derivation of the $t$-$J$ model from the Hubbard model, where $J = 4t^2/U$. This leads to the choice of $t_y = t_x\sqrt{J_y/J_x}$. We do additional calculations using $t_y = t_x J_y/J_x$. The spin gap in a 2-leg ladder $\Delta \geq J_y/2$ [118, 123, 124] is relatively large, such that it is sufficient to use temperatures $\beta J_y \approx 10$ to reach the ground state.

#### Strong coupling along the rungs

We consider the case $J_x/t_x = 0.4$, $J_y/t_x = 1.6$ and $t_y/t_x = 2$ (Figs. 5.4 and 5.6), and the case $J_x/t_x = 0.4$, $J_y/t_x = 0.8$ and $t_y/t_x = 2$ (Figs. 5.5 and 5.7), where the first case corresponds to the connection via the Hubbard model and in the second case $J_x/t_x = J_y/t_y$. The spin gap is approximately given by $\Delta \approx 1.4t$ and $\Delta \approx 0.6t$ [118, 123, 124], respectively.

We first consider the bonding band only. As one can see in Figs. 5.6 and 5.7 the major part of weight is accumulated in a single band at low energies. Its dispersion can be observed better in Figs. 5.4 and 5.5. The dispersion, especially in the case of the stronger inter-chain coupling $J_y/J_x = 4$ (Fig. 5.4) compared to $J_y/J_x = 2$ (Fig. 5.5), can

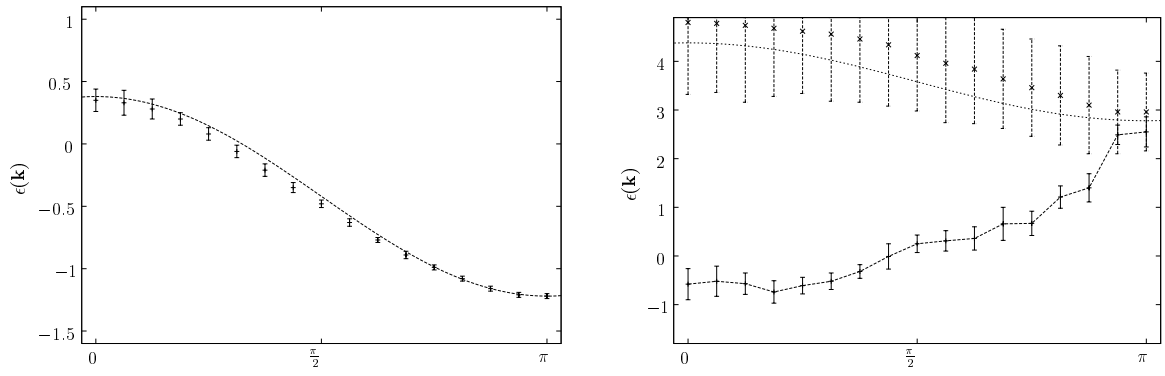


(a) Bonding band (b) Antibonding band

Figure 5.4: Lower edge of the spectrum of a $32 \times 2$ ladder with $J_x/t_x = 0.4$, $J_y/t_x = 1.6$ and $t_y/t_x = 2$. The line represents $0.80\cos(k_x)t - 0.42t$ for the bonding band, the lower line for the antibonding band it is a guide to the eye. For the antibonding band, we give additionally the peak position for the high-energy excitation, and fit it by $4t + 0.80\cos(k_x)t - 0.42t$.

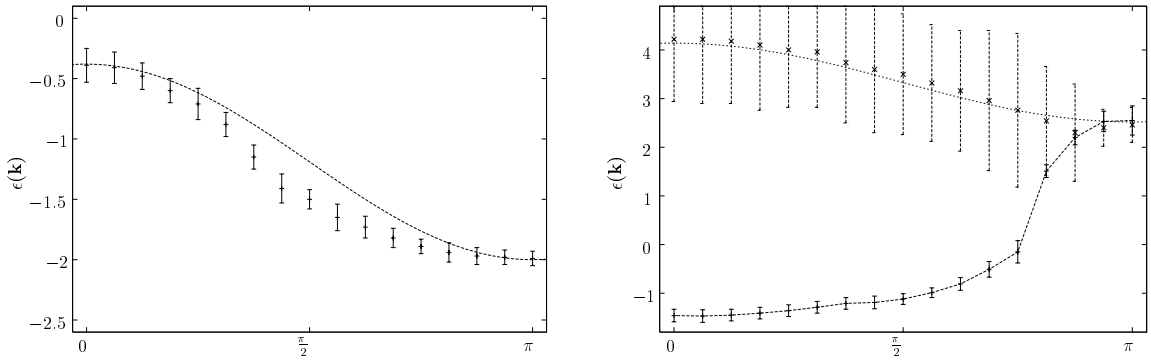


(a) Bonding band (b) Antibonding band

Figure 5.5: Lower edge of the spectrum of a $32 \times 2$ ladder with $J_x/t_x = 0.4$, $J_y/t_x = 0.8$ and $t_y/t_x = 2$. The line represents $0.81\cos(k_x)t - 1.19t$ for the bonding band, the lower line for the antibonding band it is a guide to the eye. For the antibonding band, we give additionally the peak position for the high-energy excitation, and fit it by $4t + 0.81\cos(k_x)t - 1.19t$.

be reproduced by a cosine, as the strong coupling picture suggests. The effective hopping is rescaled by about 80% in both cases. The energy at $\mathbf{k} = (\pi/2, 0)$, that is expected to be at $J_y - t_y$, is reproduced correctly, again better for the stronger relative coupling.

We continue our discussion with the antibonding band, where one can identify the band at higher excitation with the band, one obtains from the strong coupling calculation. The two bands, that are derived from the strong-coupling calculation (i.e the low-lying band in the bonding case and the high band in the antibonding case) will be called *original* bands in the following. The first important point is the energy gap of the original antibonding band to the original bonding band. As we have seen above, the original band of the bonding band, and the one of the antibonding band should be separated by about $2t_y$. In Fig. 5.6 and Fig. 5.7 this leads to a splitting of $4t_x$ in the energy units used here, what can be confirmed by inspection of the spectral function. The antibonding band, like the bonding band, follows a cosine-like dispersion.

We conclude, that the simple strong coupling limit *Ansatz* reproduces very well the major contributions of the spectral function for $J_y/J_x \gg 1$.

In the antibonding band, we further observe the presence of a *shadow* band at low energies. This band has less weight, than the band at higher energies, nevertheless it can be clearly resolved for $\mathbf{k} = (0, \pi) - (3\pi/4, \pi)$. Its energies around $\mathbf{k} = (0, \pi)$ are of the order of $J_y$ higher than the energies of the bonding band at $\mathbf{k} = (\pi, 0)$. Here it should be noticed that the spin gap $\Delta$ approaches $J_y$ in the limit $J_y/J_x \to \infty$. At this point,

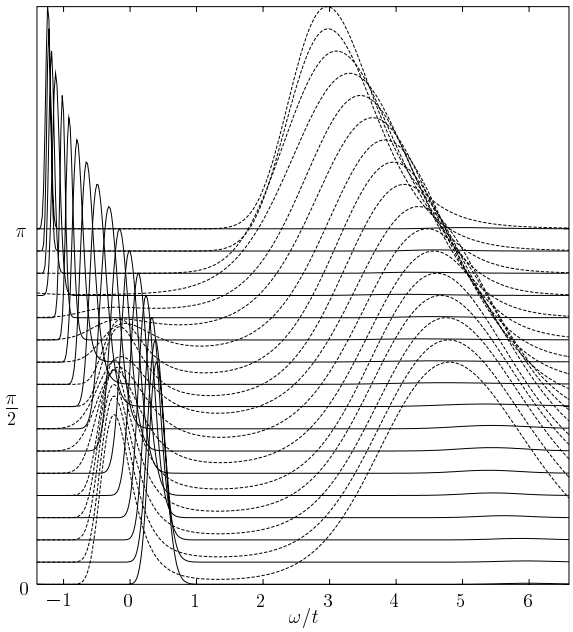


(a) Complete spectral function

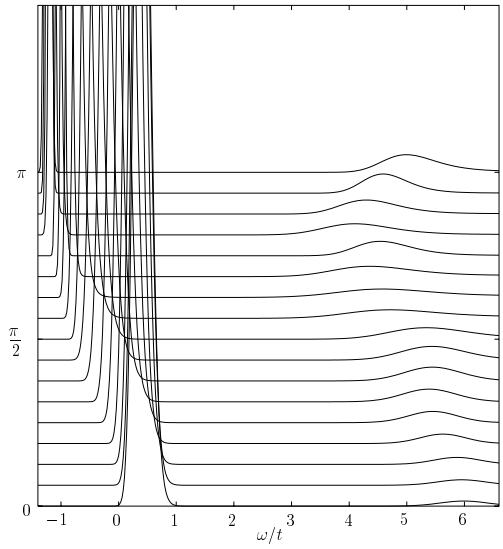


(b) Bonding band

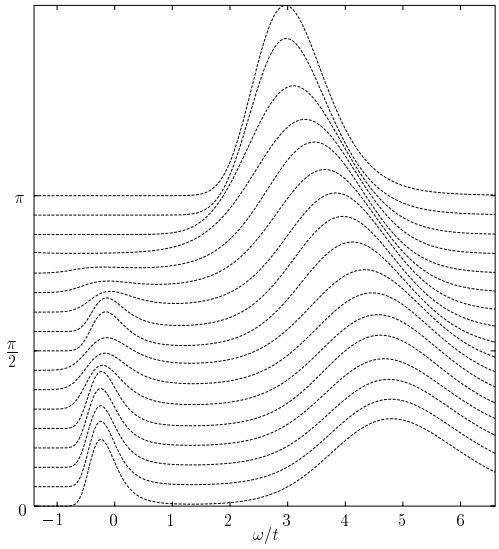


(c) Antibonding band

Figure 5.6: Spectral function of a $32 \times 2$ ladder with $J_x/t_x = 0.4$, $J_y/t_x = 1.6$ and $t_y/t_x = 2$.

we interpret the shadow band as an excitation of the bonding band, together with a spin excitation having momenta $\mathbf{q} = (\pi, \pi)$ and energy $\Delta$, where we just add up momenta and energies. For the bonding band, we see a weak structure at energies comparable to those of the original antibonding band. Whereas for the bonding original band and for the antibonding shadow band, a symmetry about $k_x = \pi/2$ has been clearly resolved, we cannot observe any significant sign of symmetries in the excitation spectra between the bonding shadow band and the antibonding original band at this point.

The shadow band will be discussed in more detail for the isotropic case, where the

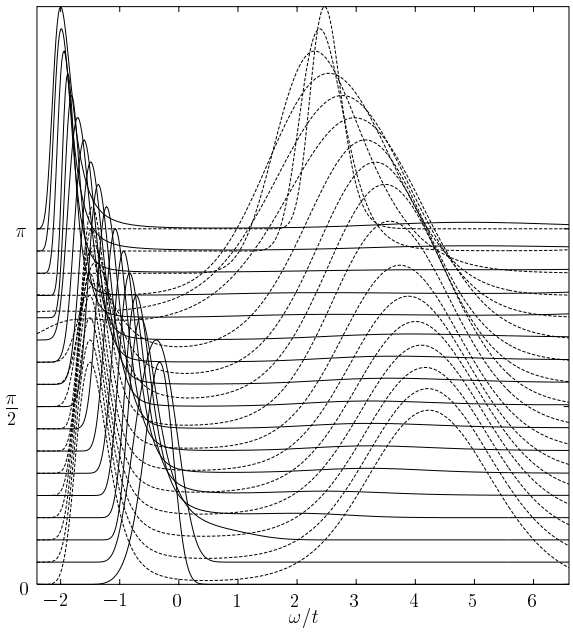


(a) Complete spectral function

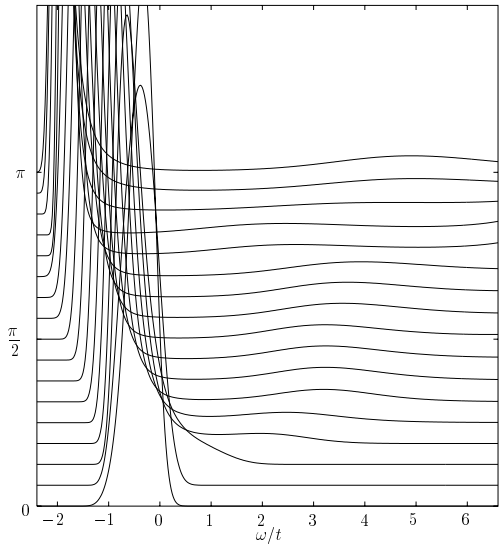


(b) Bonding band

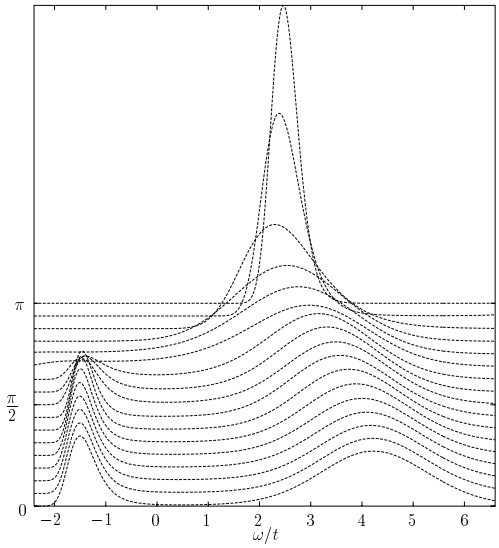


(c) Antibonding band

Figure 5.7: Spectral function of a $32 \times 2$ ladder with $J_x/t_x = 0.4$, $J_y/t_x = 0.8$ and $t_y/t_x = 2$

quality of the QMC data is better, leading to more precise results for the spectral function. A more formal calculation concerning the shadow bands will be performed in App. C.

Further noticeable are the sharp peaks of the bonding band in the two-leg ladder in contrast to the bands in one and two dimensions at $J/t = 0.4$. From this we conclude, that the quasiparticle weight is large for ladder systems with strong coupling along the rungs. The numerical data to confirm this will be shown in Sec. 5.5.

Very similar results were obtained by series expansion [65], unfortunately they worked in a parameter range with $t_x = t_y$, so we can only compare directly in the isotropic case.

These results obtained by Oitmaa *et al* are reproduced in Sec. 5.3.2, Fig. 5.16 on page 100.

### Weak coupling along the rungs

Here we briefly consider the case $J_x/t_x = 0.4$, $J_y/t_x = 0.1$ and $t_y/t_x = 0.5$ (Figs. 5.8 and 5.9). This choice of parameters can no longer be described by the picture of non-interacting rungs. The natural starting point are two one-dimensional chains, which interact weakly. The breakdown of the strong coupling picture can easily be shown by the following observations. First the bonding and the antibonding band's dispersions no longer resemble that of the strong coupling cosine bands. The strong coupling minima at $k_x = \pi$ for both bands are shifted to $k_x = \pi/2$ like in one dimension. The minima of the upper antibonding band are at $\mathbf{k} = (\pi, 0)$ and $\mathbf{k} = (\pi, \pi)$. The only remainder of the strong coupling picture is the splitting between the low-energy bonding and the high-energy antibonding band, that still is given by $4t_y = 2t_x$ (measured as the distance between the respective minima).

A comparison with the spectral function of the one-dimensional case at the same value of $J_x/t_x = 0.4$ (Fig 3.4) as considered here shows similarities of the bonding band (Fig. 5.9.b) to the lower edge of the spectrum in one dimension. The antibonding band shows appreciable weight at low energies compared to the strong coupling limit. In the following we check, whether these structures can be explained by a shadow band as in the strong coupling limit. We first observe sharp excitations of the bonding band around $\mathbf{k} = (0, \frac{3}{4}\pi)$ and of the antibonding band at $\mathbf{k} = (\pi, \frac{1}{4}\pi)$ at about the same energy, thus showing the predicted symmetry of shadow bands. Additionally, the lower band in the

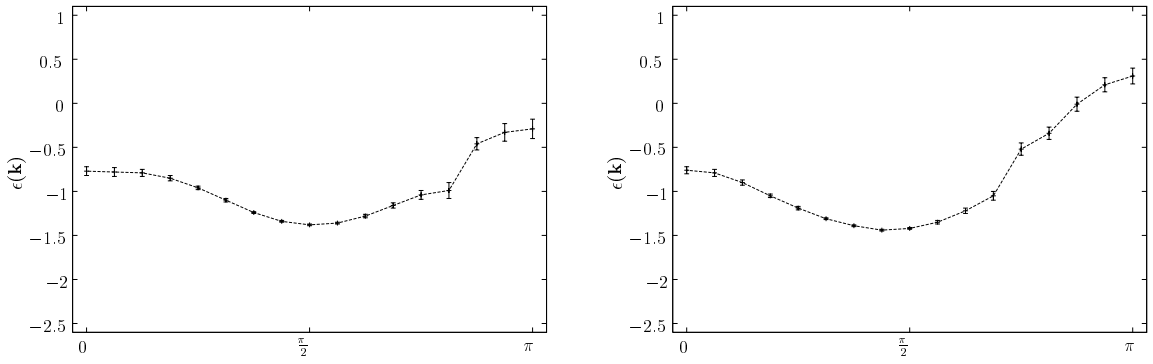


(a) Bonding band (b) Antibonding band

Figure 5.8: Lower edge of the spectrum of a $32 \times 2$ ladder with $J_x/t_x = 0.4$, $t_y/t_x = 0.5$ and $J_y/t_x = 0.1$. The lines are a guide to the eye only.

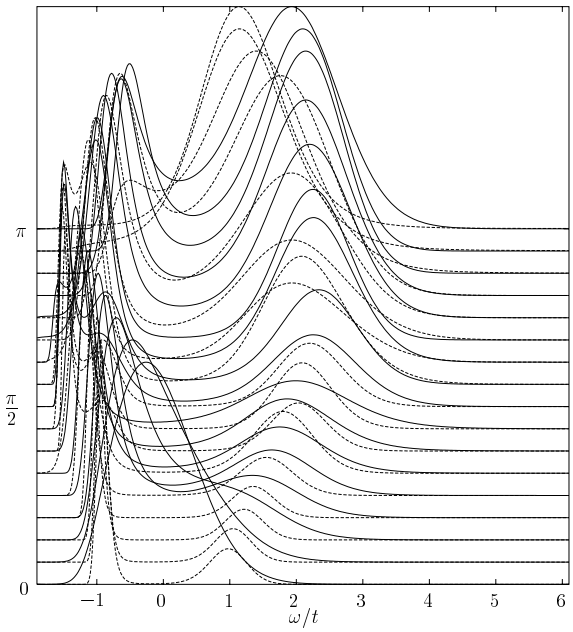


(a) Complete spectral function

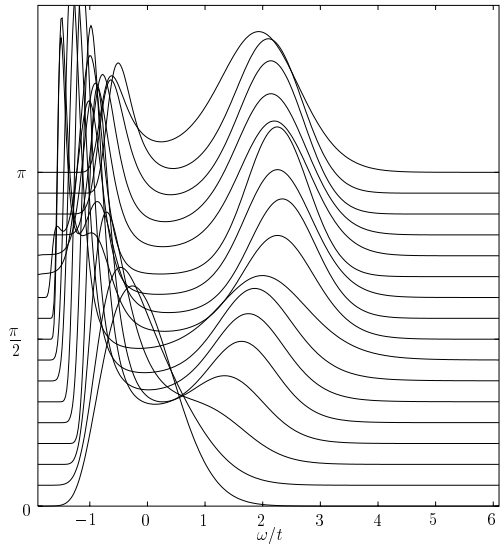


(b) Bonding band

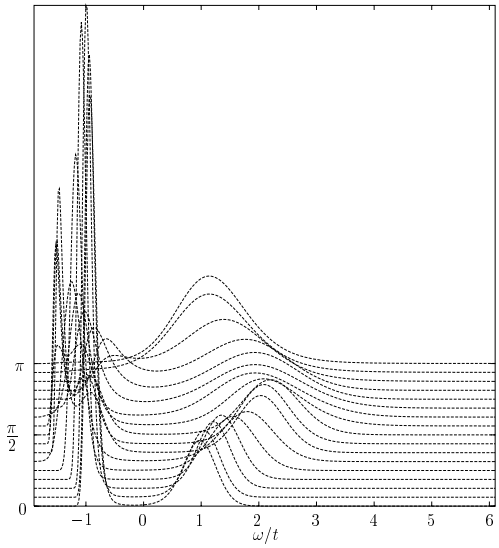


(c) Antibonding band

Figure 5.9: Spectral function of a $32\times2$ ladder with $J_x/t_x = 0.4$, $J_y/t_x = 0.1$ and $t_y/t_x = 0.5$.

antibonding spectral function looses weight when approaching $k_x = \pi$ as in the strong coupling case. However, the symmetry about $k_x = \pi/2$ of the lower edge of the spectrum for bonding and antibonding case is not given so accurately as for strong coupling.

As we have seen above, the shadow band in the strong-coupling case can be explained by a very simple *Ansatz*, namely as an excitation of the bonding band, together with a spin excitation having momenta $\mathbf{q} = (\pi, \pi)$ and energy $\Delta$, which is given by the spin gap. If this simple *Ansatz* still holds in the weak coupling limit, the energy difference of the antibonding shadow band to the bonding original band is approximately given by

the spin gap $\Delta \approx J_y/2 = 0.05t$. Our results are consistent with such a small energy difference, but we cannot conclude from our data, whether the two bands are degenerate.

On the other hand, the lower edge of the spectrum for the bonding band, the antibonding band, and for the single chain at $J/t = 0.4$ look rather similar. The spectral function can thus be explained by a one-dimensional behavior accompanied by minor corrections due to the coupling to the other chain.

From our data it is not possible to conclude, whether the two-leg ladders at weak inter-chain coupling are better described by a shadow band *Ansatz*, or by the single chain. Whereas the low-lying bonding band is very similar to the single chain, the antibonding band shows properties both of a shadow of the bonding band, and of a isolated single chain.

### 5.3.2 The isotropic case

The isotropic case is the one that has been studied most extensively in the past [57–59, 129]. The spin excitation spectrum at half filling is now well understood [117, 118, 123–127], where the most relevant result is the existence of a spin gap, with a value of $\Delta \approx 0.5J$.

We have considered here the cases $J/t = 0.4$, $J/t = 1.2$ and the supersymmetric case $J/t = 2$. As in previous cases, we consider first the lower edge of the spectrum (see Figs. 5.10-5.12), and subsequently the full spectral function (see Figs. 5.13-5.15).

We start the discussion of the isotropic case with a small Heisenberg interaction $J/t = 0.4$, the same value for $J_x/t_x$ as we used in the anisotropic case above. As can be seen from Fig. 5.10 and Fig. 5.13, the overall shape of the spectral function is more similar to the limit of strong coupling along the rungs, than to two weakly coupled chains.

The bonding band consists of a sharp low-lying band, with an overall dispersion of about $0.9t$. The shape of the dispersion has changed compared to the strong coupling limit, and is no longer following a cosine band. The minimum has shifted from $k_x = \pi$ towards $k_x \approx 3\pi/4$. Like for strong coupling the maximal energy for the bonding band is at $k_x = 0$. The minimum of the band shifts from $\mathbf{k} = (\pi, 0)$ to about $\mathbf{k} = (\frac{3\pi}{8}, 0)$, but the band is extremely flat between $k_x = \pi$ and $k_x = \pi/2$. This property is very similar to the two-dimensional case, where we observed flat bands spanning the area from $\mathbf{k} = (\pi, 0)$

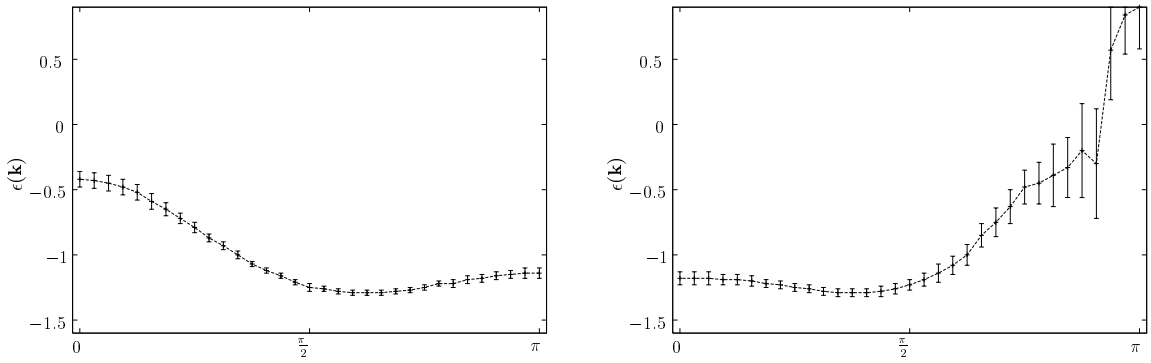


(a) Bonding Band (b) Antibonding Band

Figure 5.10: Lower edge of the spectrum of an isotropic $64 \times 2$ ladder with $J/t = 0.4$. The lines are a guide to the eye only.

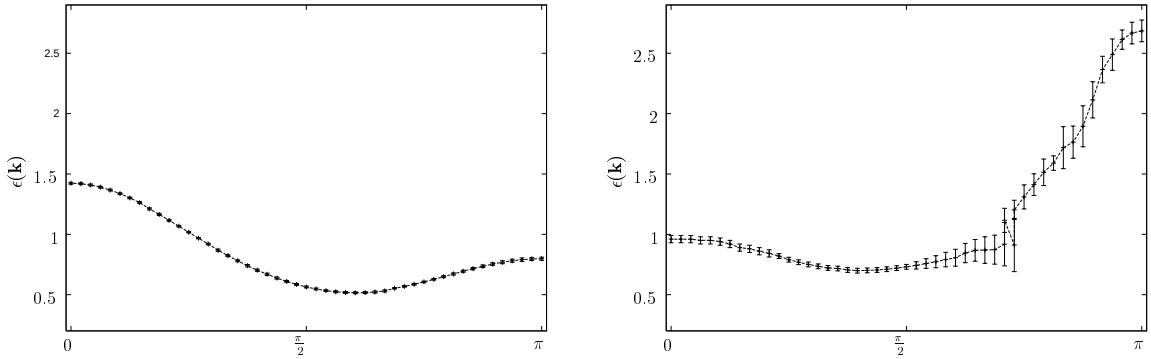


(a) Bonding band (b) Antibonding band

Figure 5.11: Lower edge of the spectrum of an isotropic $96 \times 2$ ladder with $J/t = 1.2$. The lines are a guide to the eye only.

to $\mathbf{k} = (\pi/2, 0)$ and $\mathbf{k} = (\pi/2, \pi/2)$. The occurrence of flat bands is thus not restricted to a long-range antiferromagnetic order like in the two-dimensional case, but also occurs in a spin-liquid state, which only shows short-range antiferromagnetic order. The only similarity to the weak coupling limit is the broadening of the peak around $k_x = 0$.

The antibonding band consists of two dispersing bands. The band at high energies can be related to the antibonding band in the limit of strong coupling. Its overall dispersion of about $1.5t$ is larger than for the bonding band. The energy gap between the two bands is about $3.5t$, and is thus somewhat reduced with respect to the strong coupling case.

There is an additional structure at low energies, the *shadow* band, which we already observed in the strong coupling limit. The shadow band of the antibonding band and the low-lying original bonding band are approximately symmetric to each other, where $\pi/2$ is the mirror axis, like for strong coupling. The shadow band can only be observed at values of $0 \leq k_x \leq 3\pi/4$, as at higher values of $k_x$ the weight is reduced very drastically.

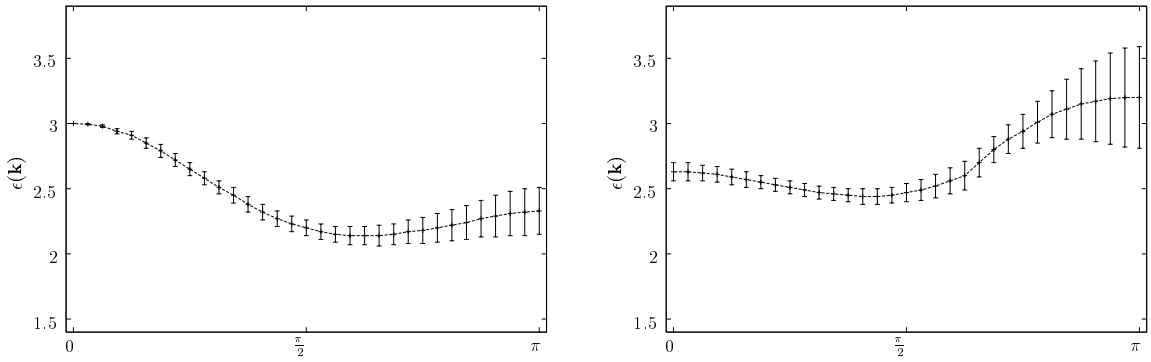


(a) Bonding band (b) Antibonding band

Figure 5.12: Lower edge of the spectrum of an isotropic $64 \times 2$ ladder with $J/t = 2$. The lines are a guide to the eye only.

For the considered value of $J/t = 0.4$ no shift in the energy of the shadow band compared to the original band can be observed, as it is the case for strong coupling. In the strong coupling limit, the spin excitation was mostly localized on a single rung, whereas in the isotropic case, it can propagate along the chain. This should lead to an increased interaction between the hole and the spin excitation, that is not considered in the simple shadow band picture, where energies and momenta of the excitations are simply added up[1]. In App. C we give a more formal calculation considering the shadow bands following the ideas of Kampf and Schrieffer [99], that can explain the additional shift in energy of the shadow band towards lower energies. For a more detailed analytical approach, both the coupling of spin excitations and holes on a two-leg ladder and the exact shape of the spin susceptibility has to be investigated in more detail.

When $J/t$ is increased, the lower edge of the bonding band and the shadow band is not changing drastically. The main effect is a transfer of weight from high energies to the low-lying bands. This effect is more pronounced in the antibonding band. The shadow band is extremely sharp for $J/t = 1.2$. At the supersymmetric point, the shadow band is less peaked than for $J/t = 0.4$ and $J/t = 1.2$. Although, a considerable amount of weight is accumulated in the shadow band, the data is not accurate enough to give a value for the quasiparticle weight. At the supersymmetric point, we observe, like in one

[1] this corresponds to a convolution of the Green's function and the susceptibility (in this case given by the approximate form $\chi(\omega, \mathbf{q}) \sim i\delta(\omega - \Delta)\delta(\mathbf{q} - (\pi, \pi))$ such as in the charge spin separation *Ansatz* in one dimension. The $\delta$-function in $\omega$-space is supported, both from our numerical results (see Fig. C.2 on page 140), and of a recent semiclassical theory [130]. We can further observe a sharp peak at $\mathbf{q} = (\pi, \pi)$ for $S(\mathbf{q})$ in Fig. C.2, which justifies the simplification in $\mathbf{q}$-space.

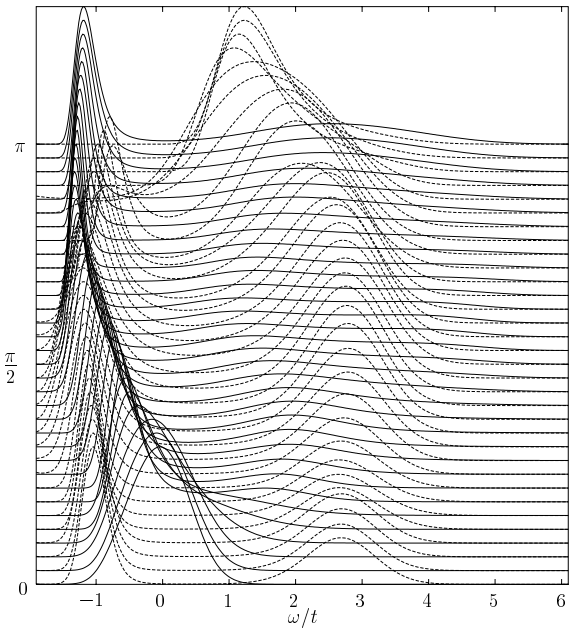


(a) Complete spectral function

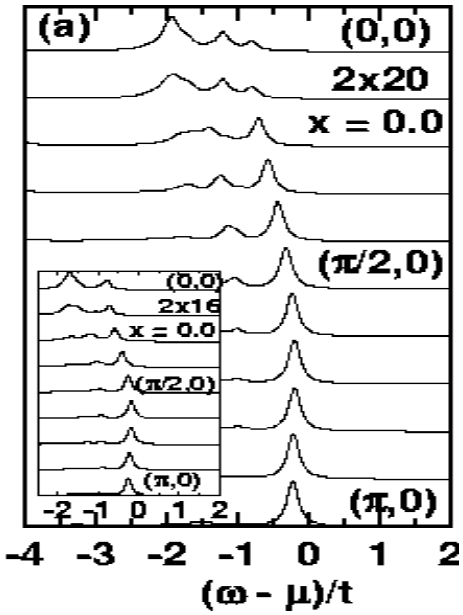


(b) Bonding band, taken -with permission of the authors- from Ref. [129]

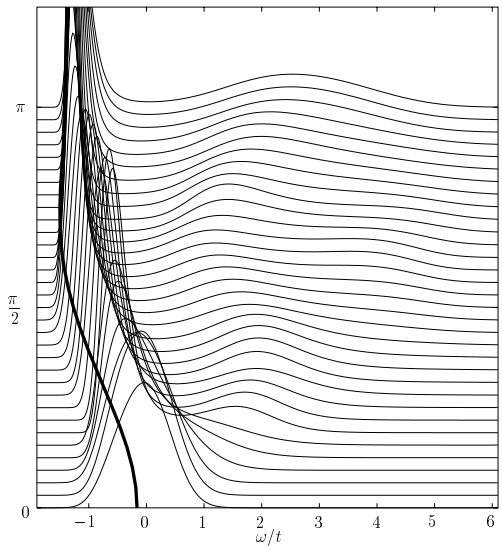


(c) Bonding Band

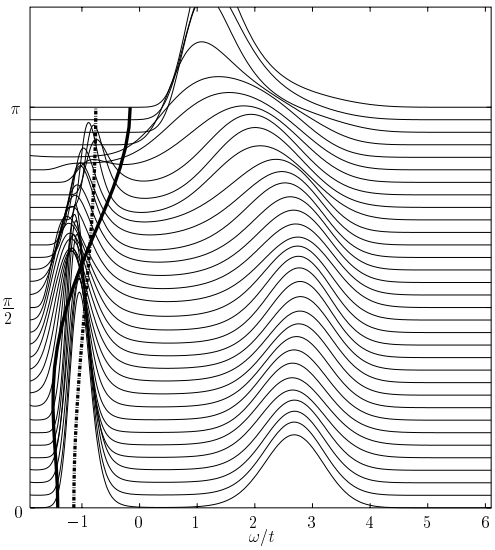


(d) Antibonding Band

Figure 5.13: Spectral function of an isotropic $64 \times 2$ ladder with $J/t = 0.4$. Fig. (b) shows recent results by Martins *et al* obtained by a truncated Lanczos algorithm. The results have to be rotated by $\pi$ for comparison. The full lines represent $\epsilon_{1/2}$ (c),(d), where for the antibonding band, we shifted the dispersion by $\pi$. The dashed line represents $\epsilon_{3/2}$ (d).

and two dimensions, the $\delta$-excitation at $\mathbf{k} = (0, 0)$, which belongs to the bonding band of the two-leg ladder.

The only analytic expression for the dispersion of the quasiparticles in the isotropic case up to now was derived by O. P. Sushkov [64]. We compare our numerical data to his

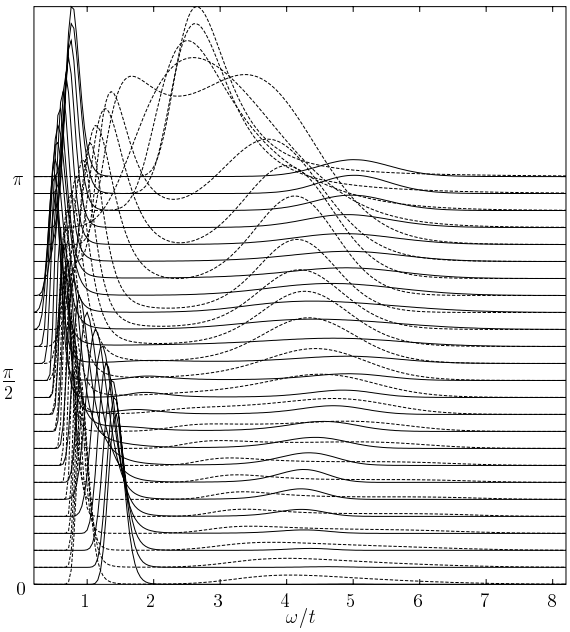


(a) Complete spectral function

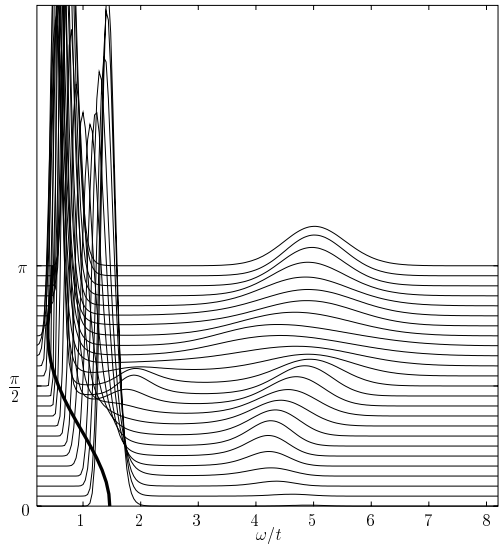


(b) Bonding band

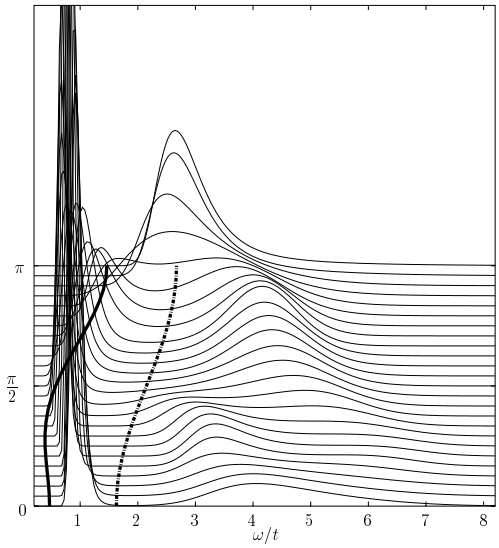


(c) Antibonding band

Figure 5.14: Spectral function of an isotropic $96 \times 2$ ladder with $J/t = 1.2$. Only every second $k$-point was plotted in the figures. The full lines represent $\epsilon_{1/2}$ (b),(c), where for the antibonding band, we shifted the dispersion by $\pi$. The dashed line represents $\epsilon_{3/2}$ (c).

results. These calculations by Sushkov start again from the strong coupling limit, and pertubatively take into account corrections of higher order. The work predicts quasiparticles, which accumulate the major part of the weight of the spectral function. At small values of $J/t$, excitations carrying spin $S = 3/2, 5/2, \ldots$ are expected, additional to the

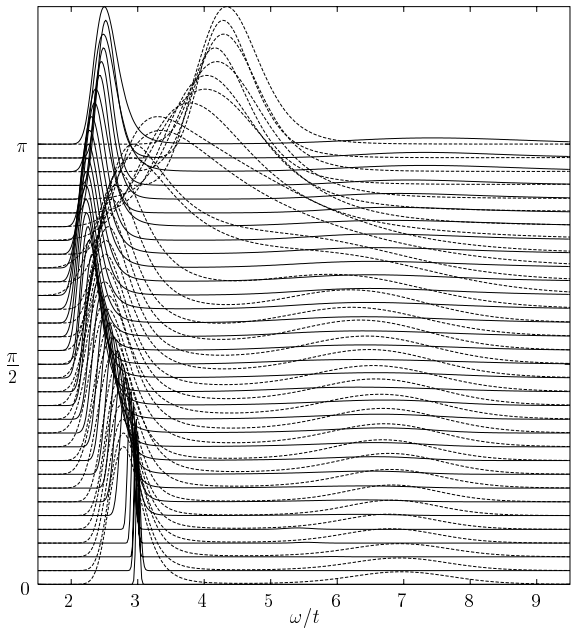


(a) Complete spectral function

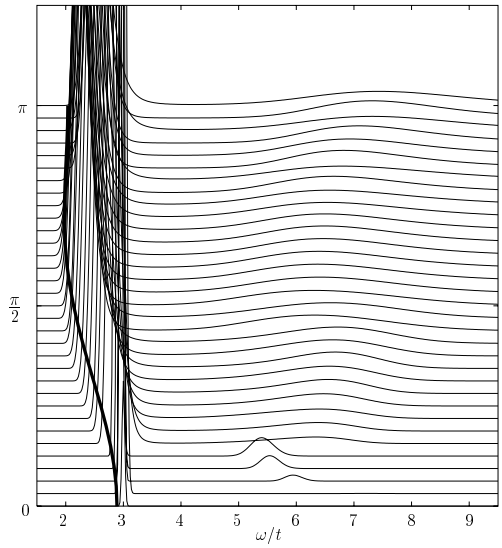


(b) Bonding band

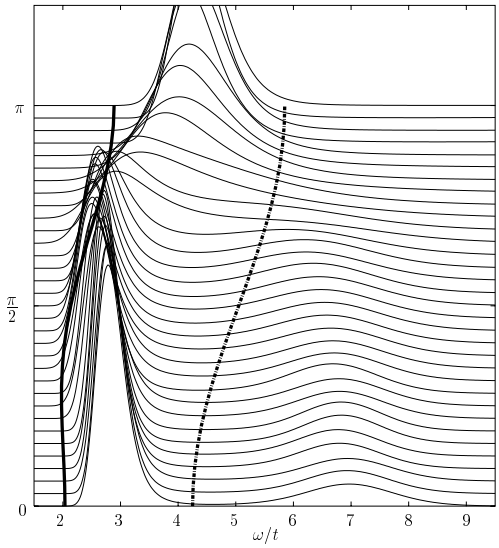


(c) Antibonding band

Figure 5.15: Spectral function of an isotropic $64 \times 2$ ladder with $J/t = 2$. The full lines represent $\epsilon_{1/2}$ (b),(c), where for the antibonding band, we shifted the dispersion by $\pi$. The dashed line represents $\epsilon_{3/2}$ (c).

$S = 1/2$ quasiparticle. The dispersions of these excitations are given by

$$\begin{aligned}
\epsilon_{1/2} &= \epsilon_0 - t + \rho^2 \cos q_x + \Delta E/2 - \sqrt{(\Delta E/2)^2 + 2|V|^2} \\
\epsilon_{3/2} &= \epsilon_0 - 2t + J_y + \frac{J_x}{4} + \frac{3}{8}\frac{J_x^2}{J_y} + 2t_{eff} \cos q_x \\
\epsilon_{5/2} &= \epsilon_0 - (1+\sqrt{2})t + 2J_y + \frac{3J_x}{4} + \frac{3}{4}\frac{J_x^2}{J_y},
\end{aligned} \tag{5.12}$$

where $\Delta E = (2t + J_y - 1/3J_x + \frac{3}{8}\frac{J_x^2}{J_y}$, $\rho = 1 - 3/2\mu^2$, $V = -\sqrt{3}2\rho t - \sqrt{3}4\rho J e^{-iq_x} -$

$\sqrt{3}/2\mu t e^{-2iq_x}$, and the coefficient $\mu \approx 0.3$ [120,125] takes into account spin-wave quantum fluctuations. The effective hopping for $\epsilon_{3/2}$ can be derived pertubatively and is given by

$$t_{eff} = -\frac{t_x J_x/4}{t_x + 3J_x^2/(8J_y) - J_x/4}. \tag{5.13}$$

We compare our results to these predictions. The energies $\epsilon_{1/2}$ and $\epsilon_{3/2}$ has to be shifted pairwise by a constant (additional to the one due to the $1/4 n_i n_j$-term). We choose this constant, which is of the order $0.4t$ such that the bonding band from *Maximum Entropy* around $k_x = \pi$ is well described by $\epsilon_{1/2}$. When the exact lower edge is taken, the constant reduces to approximately $0.2t$, the same deviation seen as in series expansion [65]. When one compares $\epsilon_{3/2}$ with the results from our simulations, one has to notice, that the particle corresponding to $\epsilon_{3/2}$ is produced by two elementary excitations, one triplet excitation and one hole excitation. In our simulations, the triplet excitation is absent, so the overall system in our simulations always carries spin 1/2. It is therefore not clear, if remainders of the $\epsilon_{3/2}$ bound state can be seen in principle, and if it goes to the odd or even parity channel. From an inspection of the results, we see, that the bound $S = 3/2$ state can at best be identified with the shadow band in the antibonding band, but only for small values of $J/t$.

As one can see from Figs. 5.13-5.15, the lower edge of the spectrum is well described by $\epsilon_{1/2}$ of the above *Ansatz* between $k_x = \pi/2$ and $k_x = \pi$. Around $k_x = 0$, the exact numerical results are lower in energy than the analytical calculations. In this region, the quasiparticles of eq.(5.12) have a large energy and are thus unstable with respect to real emission of a spin wave which is not considered in the *Ansatz* (5.12) [64].

The excitations corresponding to $\epsilon_{3/2}$ can be identified with the antibonding shadow band. The effective hopping for the isotropic case is $t_{eff} \approx 0.095$, 0.26, 0.40 for $J/t = 0.4$, 1.2, 2. We notice, that the agreement is much worse than for the bonding band. Our simple explanation of the shadow band as *bonding band + non-local spin excitation* seems to explain the data better than the bound *spin+hole* particle of eq.(5.12). The fits which are obtained from the shadow band picture of App. C (full lines in the antibonding band of Figs. 5.13-5.15) reproduce the lower edge of the spectrum fairly well for all values of $J/t$, whereas the dispersion of $\epsilon_{3/2}$ only describes the lower edge for $J/t = 0.4$.

We finally consider bound states corresponding to $\epsilon_{5/2}$. The energy gap of this excitation to $\epsilon_{3/2}$ at $k_x = \pi/2$ is for the isotropic case given by $\frac{15}{8}J + (1 - \sqrt{2})t$. For

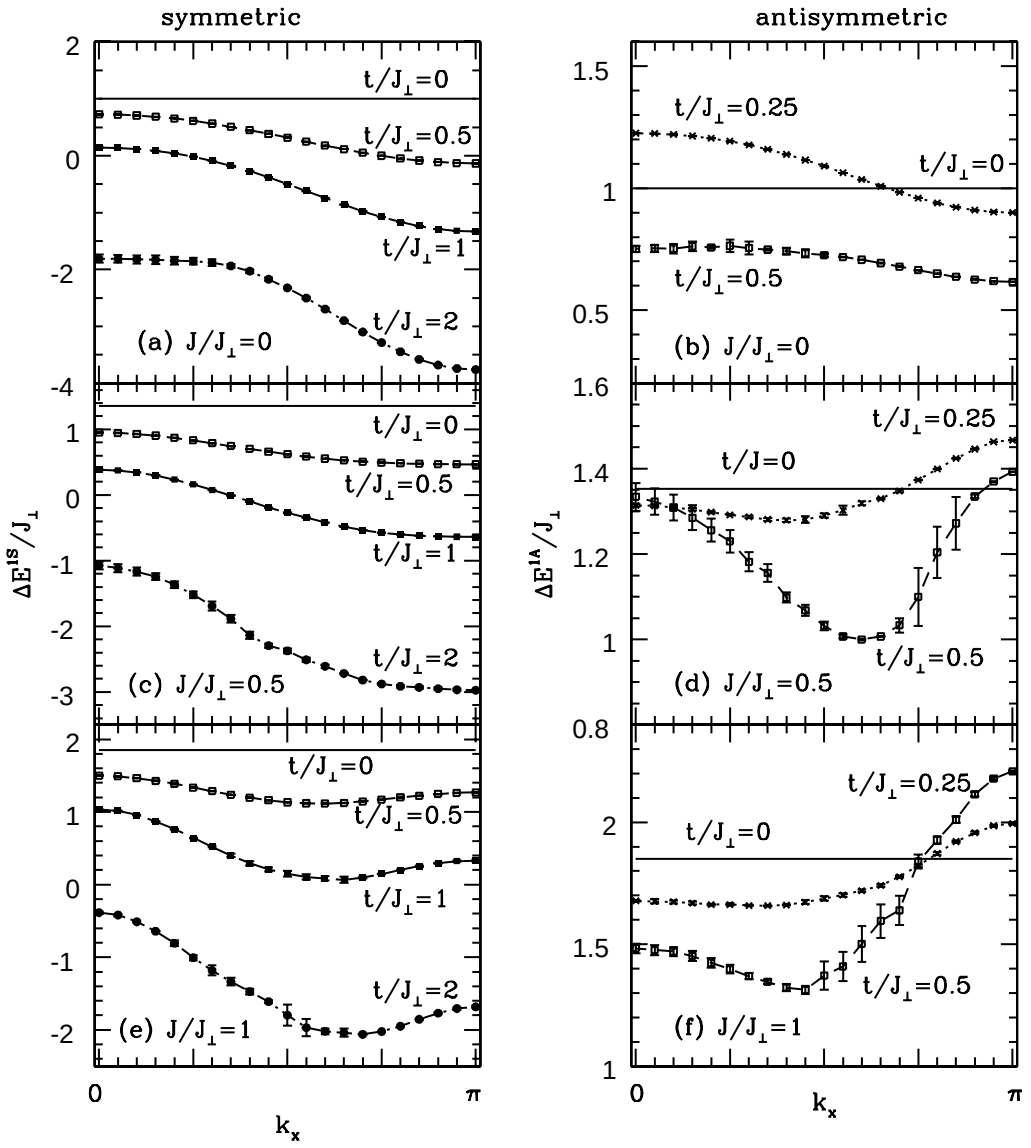


Figure 5.16: Results for the lower edge of the spectral function from series expansion, reproduced -with permission of the authors- from the article by Oitmaa *et al* [65]. The notations are $J_\perp \equiv J_y$, $J \equiv J_x$ and $t \equiv t_y = t_x$. The energy scale is in units of $J_y$.

$J/t = 0.4, 1.2, 2$ this corresponds to $0.34, 1.84t, 3.34t$ and thus the excitation energy scales linearly with $J/t$. From inspecting our data, we cannot see any numerical evidence for such an excitation neither in the bonding nor in the antibonding band. It is important to notice at this point again, that we do not probe with the correct quantum number (in this case $S = 5/2$), so that we can in principle only find remainders of this state, which form locally.

Summarizing, we can state, that the excitations in a two-leg ladder are very well described by a strong-coupling *Ansatz* at low excitations ($\epsilon_{1/2}$), whereas for the higher

excitations, the agreement is only reasonable for small values of $J/t$. The low-lying antibonding excitations can be explained by a simple shadow band picture.

Finally, we compare to results obtained by series expansion. Fig. 5.16, taken from Ref. [65], shows results for $t_x = t_y$ for values of $J_x/J_y = 0$, 0.5, 1. Fig. 5.16.e and 5.16.f correspond to the isotropic case, and can directly be compared to our results. We find an excellent agreement for $J/t = 2$, the results from series expansion for $J/t = 1$ and $J/t = 0.5$ are very similar to our results at $J/t = 1.2$ and $J/t = 0.4$ respectively.

## 5.4 Excitations at higher energies in the two-leg ladder

As in the two dimensional case, the motion of a hole in the spin background can lead to unsatisfied bonds. The major difference to two dimensions is the absence of long-range antiferromagnetic order in the ladder, so the string picture is probably not applicable to two-leg ladders.

The investigation of excitations at higher energies, or near the quasiparticle peak, is performed in the same way like in two dimensions. We first subtract the part in the Green's function, that corresponds to the low-lying quasiparticle. The modified Green's function is then used as an input for the *Maximum Entropy* method. This procedure is only done for the bonding band, as for the antibonding band, the weight of the lowest excitations is rather small and its absolute value cannot be calculated accurately enough.

In the strong coupling limit, the low energy peak is very sharp for all values of $k_x$ (see Figs. 5.4-5.7). When the exponential corresponding to that peak is removed from the Green's function, then the remaining Green's function suffers from large relative errors. A subsequent *Maximum Entropy* analysis of this modified Green's function does not reveal new structures in the spectral function.

For the isotropic case we do the calculations for the three cases $J/t = 0.4$, $J/t = 1.2$, and $J/t = 2$ (see Fig. 5.17) for the bonding band. The structures which are about $4t$ higher in energy than the quasiparticle band are now better resolved. For the parameters $J/t = 0.4$ and $J/t = 1.2$ these structures can definitely be identified with the shadow

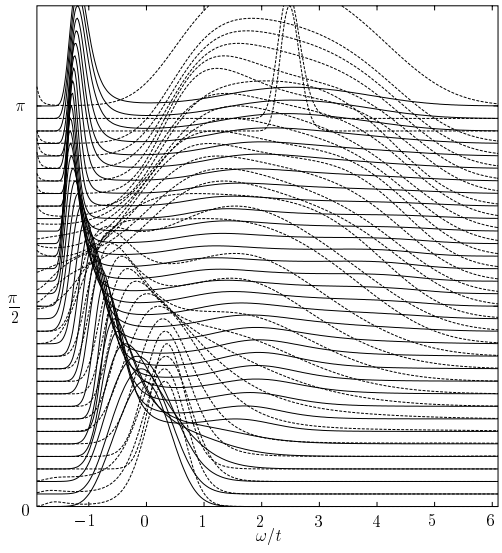


(a) $J = 0.4t$, $N = 64 \times 2$

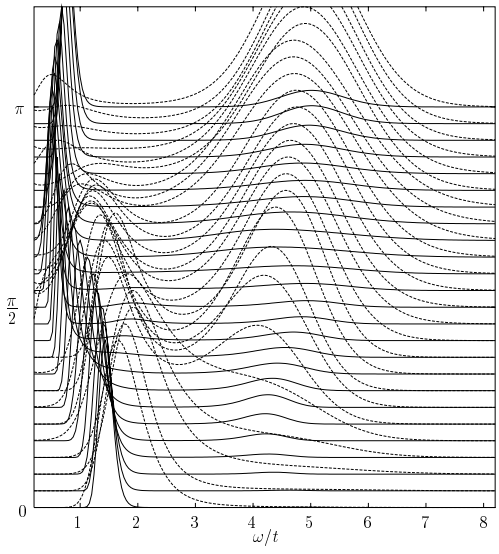


(b) $J = 1.2t$, $N = 96 \times 2$

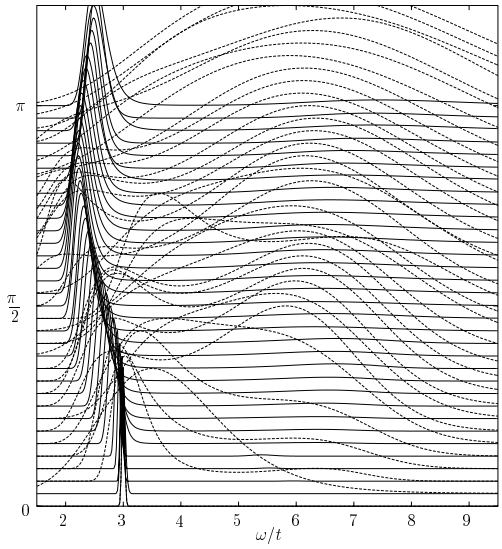


(c) $J = 2t$, $N = 64 \times 2$

Figure 5.17: Bonding band of an isotropic two-leg ladder when the lowest excitation is removed. The original spectral function is shown for comparison (full lines).

band of the high energy antibonding band emerging from the strong coupling limit. For $J/t = 2$ the high-energy contributions of the bonding band are very small, so that the resolution is not good enough to see the symmetry between the two bands.

We can see an additional structure, at least for $J/t = 0.4$ and $J/t = 1.2$ between $\mathbf{k} = (0, 0)$ and $(\pi/2, 0)$. This structure is nearby the lower edge of the spectrum, and does not scale significantly with $J/t$. For this reason, we do not identify this excitation with some string processes. This structure can neither be explained by a *shadow* corresponding to spin excitations with even parity. The structure factor for these excitations is -like

in the odd parity channel- peaked around $k_x = \pi$, but only has about 15% of the odd parity weight, and the spin gap at this $k$-point is about $2J$ in the isotropic case [131]. We therefore expect in this picture, that the energy difference between the second peak at $k_x = 0$ and the low-lying bonding band at $k_x = \pi$ is about $2J$. This is only fulfilled for $J/t = 0.4$, whereas for $J/t = 1.2$ the difference is far too small.

On the other hand the *quasiparticle* $\epsilon_{1/2}$ obtained by Sushkov [68] is not well defined around $k_x = 0$, as it is unstable with respect to a real emission of a spin wave. From our calculation however, we obtain a real quasiparticle around this $k$-point with a fairly large quasiparticle weight. We therefore identify the state, which appears next to the lower edge of the spectrum (the quasiparticle) with the excitation obtained by Sushkov, which in this region only corresponds to the second-lowest excitation, and therefore does not correspond to the quasiparticle as opposed to the region $k_x > \pi/2$, where the excitation given by Sushkov really follows the lower edge.

We finally check for the excitation $\epsilon_{5/2}$ (see eq.(5.12)). The energies, where these excitations are expected are at $\omega/t = -0.61t$, $3.99t$, $8.49t$ for $J/t = 0.4$, 1.2, 2. Again we cannot observe any numerical evidence for remainders of these excitations.

The *Maximum Entropy* analysis of the modified Green's function has thus revealed the following two results for the isotropic case. First we showed, that the high-energy excitation in the bonding band is the shadow band of the original antibonding band. The excitation near the lower edge corresponds to the excitation $\epsilon_{1/2}$ given by Ref. [68], which for $k_x < \pi/2$ is not the quasiparticle, but the second-lowest excitation.

## 5.5 The quasiparticle weight

The quasiparticle weight in a two-leg ladder is expected to be relatively large in the thermodynamic limit [64, 120, 131, 132]. As the system has a large spin-gap there are no decay channels available for the quasiparticles. This effect is not size dependent, and therefore the finite-size effects for lattice sizes $N > 6 \times 2$ are small. Basically these results have been confirmed by our simulations.

As one can see in Fig. 5.18, the size effects for lattices, that are longer or equal $L = 32$, are in fact smaller than the resulting error bars. In the following, we will take all results from the largest system, that has been calculated, without doing any finite-size scaling.

### 5.5.1 Strong coupling along the rungs

We first consider the strong coupling limit. As one expects from the spectral function (5.6), there is an extremely large quasiparticle weight in the bonding band, whereas in the antibonding band the quasiparticle weight is small, or even vanishing (see Fig. 5.19). This result supports the assumption, that the strong coupling limit is robust not only for the dispersion, but also for more sensitive quantities like the quasiparticle weight. The small weight for the antibonding shadow band can already be seen directly from the spectral function. A large spin gap leads to a shadow band with little weight, as it can be expected intuitively, as the coupling between the spin susceptibility and the Green's function corresponding to the bonding band decreases with the spin gap (see App. C).

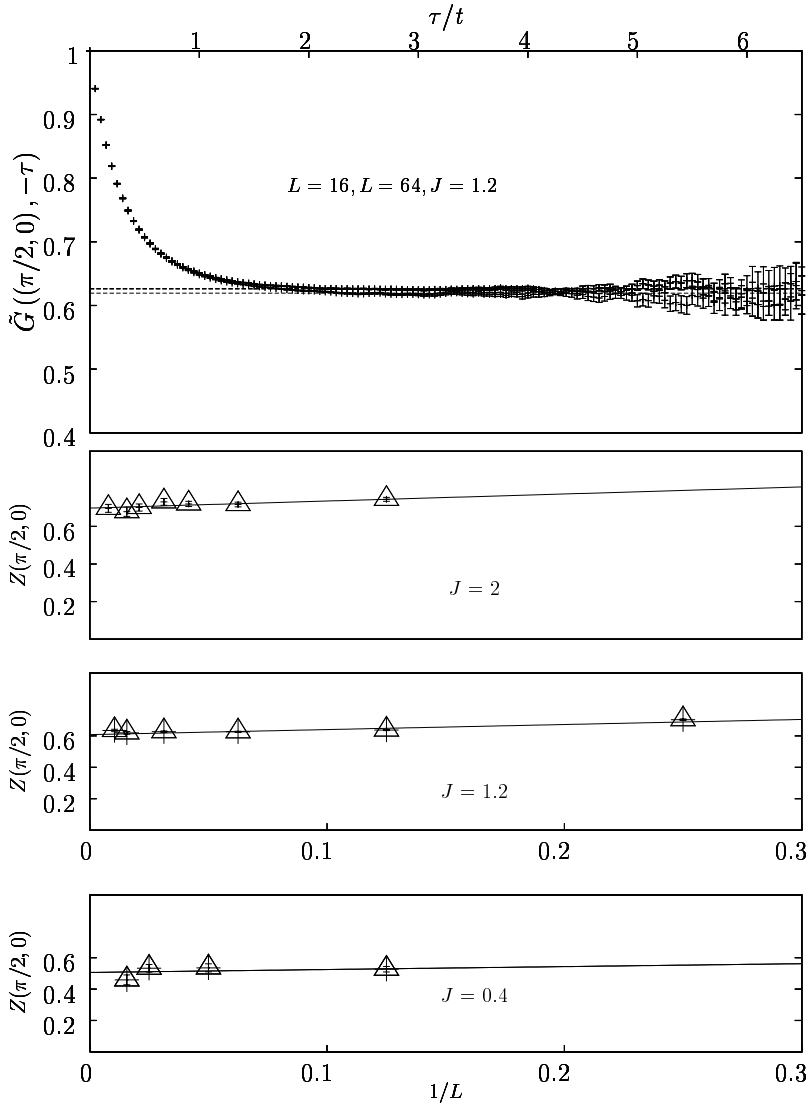


Figure 5.18: Finite-size scaling for $J/t = 0.4, 1.2, 2$ and $\mathbf{k} = (\pi/2, 0)$

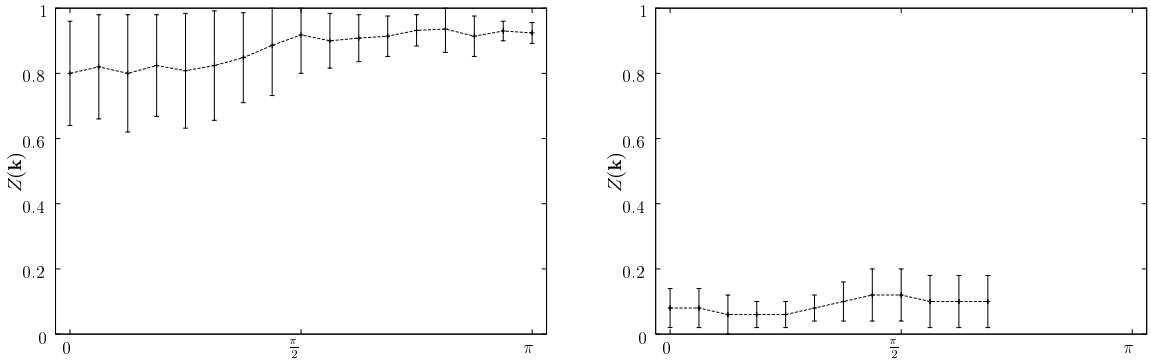


(a) Bonding band (b) Antibonding band

Figure 5.19: The quasiparticle weight for $J_x/t_x = 0.4$, $J_y/t_x = 1/6$ and $t_y/t_x = 2$ and $N = 32 \times 2$. For the antibonding band (b), the lower band can only be resolved between $k_x = 0$ and $k_x \approx 3\pi/4$. The data for the antibonding band is not good enough to make a final statement if the quasiparticle weight in the antibonding band is finite for the chosen values of $J$ and $t$.

### 5.5.2 The isotropic case

For the isotropic case, we consider again the cases $J/t = 0.4$, $J/t = 1.2$, and the supersymmetric case $J/t = 2$. The results are shown in Figs. 5.20-5.22 both for the bonding and for the antibonding band. For the antibonding case, we can only give the quasiparticle weight up to $k_x \approx (2\pi/3, \pi)$. Above that value, it is only an upper bound for the quasiparticle. In the bonding band, for $J/t = 0.4$ and $k_x < \pi/4$, we can only give an upper bound, too.

At $J/t = 2$ we cannot give a result for the quasiparticle weight in the antibonding

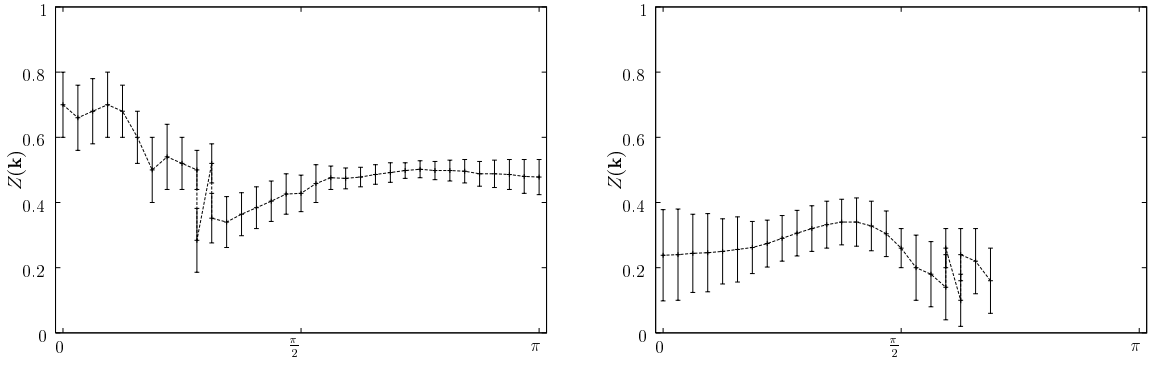


(a) Bonding band (b) Antibonding band

Figure 5.20: The quasiparticle weight for $J/t = 0.4$ and $N = 64 \times 2$. The kink in the values indicates, that the results should be interpreted as an upper bound only starting from this value. This is the case for $k_x < \pi/4$ in the bonding case, and $k_x > 5\pi/8$ in the antibonding band.

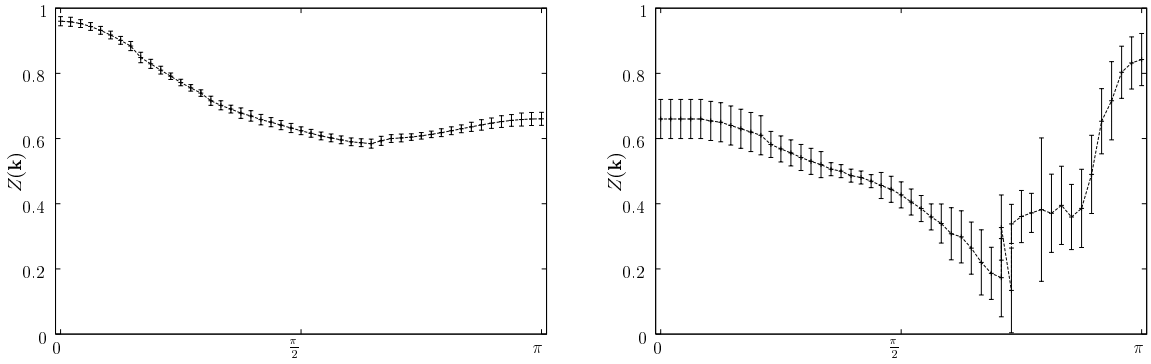


(a) Bonding band (b) Antibonding band

Figure 5.21: The quasiparticle weight for $J/t = 1.2$ and $N = 96 \times 2$. For $k_x > 3\pi/4$ in the antibonding band, the presented values are only an upper bound. The quality of the data for the antibonding band is not sufficient to extrapolate the quasiparticle weight.

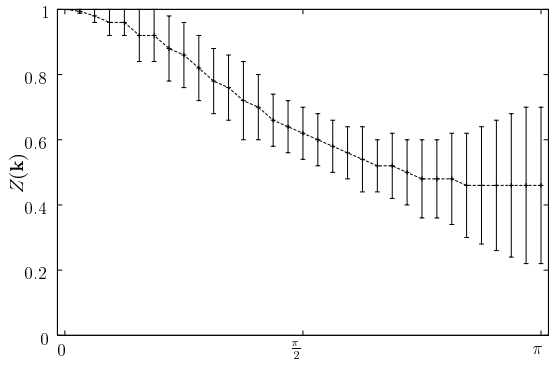


(a) Bonding band

Figure 5.22: The quasiparticle weight for $J/t = 2$ and $N = 64 \times 2$.

band, as the quality of the Green's function is not sufficient to obtain the weight of the lowest exponential.

The results for $Z(\mathbf{k})$ show again, that the weight of the shadow band vanishes, when approaching $\approx 3/4\pi$ from the $k_x = 0$ direction. We cannot make any conclusions from our data, if a very small contribution still exists in the range $(3/4\pi, \pi) - (\pi, \pi)$. Especially in the bonding band, the quasiparticle weight is large for most values of $k_x$. For small $J/t = 0.4$, the maximal quasiparticle weight is around $k_x = \pi$, whereas for intermediate ($J/t = 1.2$) and large values of $J/t$ the maximum of $Z(k_x, 0)$ shifts toward $k_x = 0$, similar to the two-dimensional case (see Fig. 4.26). For the supersymmetric point $J/t = 2$, the spectral function for $\mathbf{k} = (0, 0)$ is only a single $\delta$-function containing the complete weight of the spectral function, like in two dimensions and the single chain.

We have shown, that the quasiparticle weight in a two-leg ladder is relatively large in the thermodynamic limit. This is in agreement to approaches using self-consistent

Born approximation [120] and exact diagonalizations [120, 132] on small lattices. As a consequence of the large quasiparticle weight, perturbational and variational calculations give surprisingly exact results [68] different from the one- or two-dimensional case.

# Chapter 6

# A single hole in the three-leg ladder

In contrast to the one-dimensional and two-dimensional cases, the three-leg ladder has not been studied very extensively up to now. One of the main reasons is, that only quite recently first experiments on the related materials like e.g. $Sr_2Cu_3O_5$ [121, 122] have been carried out, showing among other things, that the susceptibility $\chi(T)$ approaches a constant as the temperature $T \to 0$ like in a one-dimensional chain. In contrast to the two-leg ladders, long-range antiferromagnetic order has been observed by muon spin resonance measurements [133] in $Sr_2Cu_3O_5$. This long-range magnetic order is most probably stabilized by the weak inter-chain coupling. In a single isolated three-leg ladder one expects quasi-long-range magnetic order like in a one-dimensional system, as, according to the theorem of N. D. Mermin and H. Wagner [134], true long-range order cannot occur in a one-dimensional system with short-range interactions only.

The number of available analytical or numerical results is still limited, as the ladder systems have attracted considerable interest just a few years ago, when the related materials have been explored experimentally. One main result for the three-leg Heisenberg ladder is the absence of a spin gap in the thermodynamic limit [57–59, 66, 135, 136]. For finite systems at half filling, the low-energy physics is thus very much dependent on the finite-size gap in the spin excitation spectrum. As a consequence thereof it is very difficult to extrapolate results from exact diagonalization [67] to the thermodynamic limit, where the largest lattices, that are in principle accessible at the time, are about $10 \times 3$ lattice points.

## 6.1 Checkerboarding and boundary conditions

We first give some technical details and make some remarks about our algorithm in a three-leg ladder, as for this topology, some minor changes to the algorithm have to be done. This concerns both the calculation of the Green's functions, that will be addressed in the next section, and the underlying loop algorithm.

The basic difference between the three-leg ladder and the previously discussed topologies are the open boundary conditions in the direction along the rungs, the $y$-direction. These boundaries have to be considered in the loop algorithm. The checkerboarding in the direction along the legs, the $x$-direction can be retained, whereas in $y$-direction, the boundaries are incorporated by setting the probability for the hole and for the pseudospin to jump from the bottom leg 0 to the top leg 2, or from leg 2 to 0 equal to zero.

As this entails some changes to the loop algorithm, the Heisenberg loop part is checked by comparing with the ground state energy for the isotropic case given by $E_0 = -0.6006(3)J$ [135] per site. Our result in a $48 \times 3$ lattice, with $\beta J = 10$ and $\Delta\tau J = 0.1$ gives us $(-3.058 \pm 0.018)J$ per rung. The Heisenberg model used by B. Frischmuth *et al* is without the $1/4J$ term, that is part of the $t$-$J$ model. When we subtract $0.25J$ per bond, or $-1.25J$ per rung, we end up with an energy of $-0.6027J \pm 0.006J$. The energy of our simulations is thus correct within the error bars.

## 6.2 Exactly solvable limits

Again we start with the discussion of two exactly solvable limits, the fully polarized, ferromagnetic state, that we use to define the three bands in the three-leg ladder, and the physics of a single isolated rung. The single rung picture is extended pertubatively by switching on weak interactions along the chains.

### 6.2.1 The bands for the three-leg ladder

In a three-leg ladder with open boundaries in $y$-direction, the wave vector $k_y$ in $y$-direction is no longer a good quantum number. The three bands can therefore not be labeled by their $k_y$-vector, that does not exist, but as bonding, antibonding and nonbonding. In $x$ direction we still have periodic boundary conditions and therefore a well defined wave

vector. It is important to notice, that the Green's functions in real space (2.15) are now no longer translation invariant in $y$ direction, but that we have two different possibilities for the Green's function at $\tau = 0$, one with position $y$ in the middle of the ladder, and one with $y$ at the upper or lower leg.

In order to define the three bands, we solve the free particle in an open three-site system. The three eigenstates are

$$v_n = \begin{pmatrix} 1/\sqrt{2} \\ 0 \\ -1/\sqrt{2} \end{pmatrix}, \quad v_b = \begin{pmatrix} 1/2 \\ 1/\sqrt{2} \\ 1/2 \end{pmatrix}, \quad v_a = \begin{pmatrix} 1/2 \\ -1/\sqrt{2} \\ 1/2 \end{pmatrix}, \tag{6.1}$$

with energies $\epsilon = 0, \pm\sqrt{t}$. The indices $n, b, a$ stand for nonbonding, bonding, and antibonding, respectively. In a short form resembling a Fourier representation, one can write [136]

$$v_q = \frac{1}{\sqrt{2}} \begin{pmatrix} \sin(1k_y) \\ \sin(2k_y) \\ \sin(3k_y) \end{pmatrix}, \tag{6.2}$$

where $k_y = \frac{\pi}{4}, \frac{\pi}{2}, \frac{3\pi}{4}$ for $q = b, n, a$, respectively.

This leads to the following Green's functions for the three different bands:

$$\begin{aligned} G_n(k_x,\tau) = 1/2 \sum_x \Big[ & \exp(ikx) G\big((x, 2-2), \tau\big) + G\big((x, 0-0), \tau\big) - \\ & - G\big((x, 0-2), \tau\big) - G\big((x, 2-0), \tau\big)\Big] = \\ & = 1/2\Big[G\left(\big(k_x, 0-0\big), \tau\right) + G\big((k_x, 2-2), \tau\big) - \\ & - G\big((k_x, 0-2), \tau\big) - G\big((k_x, 2-0), \tau\big)\Big] \end{aligned} \tag{6.3}$$

$$\begin{aligned} G_b(k_x,\tau) = 1/4\Big[ & G\big((k_x, 0-0), \tau\big) + G\big((k_x, 2-2), \tau\big) + \sqrt{2}\Big(G\big((k_x, 0-1), \tau\big) + \\ & + G\big((k_x, 2-1), \tau\big)\Big) + G\big((k_x, 0-2), \tau\big) + G\big((k_x, 2-0), \tau\big) \\ & + \sqrt{2}\Big(G\big((k_x, 1-0), \tau\big) + G\big((k_x, 1-2), \tau\big)\Big) + 2G\big((k_x, 1-1), \tau\big)\Big] \end{aligned} \tag{6.4}$$

$$\begin{aligned} G_a(k_x,\tau) = 1/4\Big[ & G\big(\big(k_x, 0-0\big), \tau\big) + G\big((k_x, 2-2), \tau\big) - \sqrt{2}\Big(G\big((k_x, 0-1), \tau\big) + \\ & + G\big((k_x, 2-1), \tau\big)\Big) + G\big((k_x, 0-2), \tau\big) + G\big((k_x, 2-0), \tau\big) - \\ & - \sqrt{2}\Big(G\big((k_x, 1-0), \tau\big) + G\big((k_x, 1-2), \tau\big)\Big) + 2G\big((k_x, 1-1), \tau\big)\Big]. \end{aligned} \tag{6.5}$$

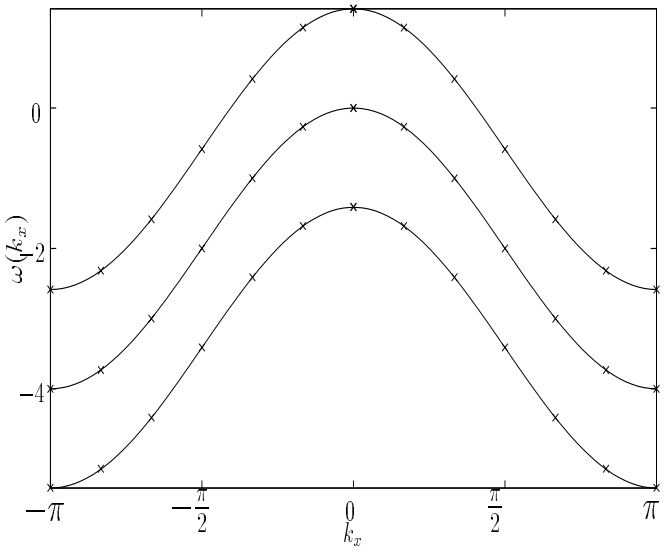


Figure 6.1: The dispersion of holes in a three-leg ladder, when the spins are ferromagnetically ordered. The crosses show the QMC data, produced by fitting the Green's function to an exponential. The lines show the three $2t\cos(kx) + \Delta$ bands, where $\Delta = 0, \pm\sqrt{2}$. For electrons, the sign of the dispersion changes, so that the minima are at $k_x = 0$.

Here $G\big((k_x, i-j), \tau\big)$ stands for $\sum_x \exp(ikx)\langle f_{(x,i)}(\tau) f^\dagger_{(0,j)}\rangle$, where $x$ is the coordinate along the chain, $i, j$ labeling the legs of the ladders, where leg 1 is in the middle. In principle one can simplify the above formulas, when the symmetries between the Green's functions $G\big((k_x, 1-0), \tau\big) = G\big((k_x, 1-2), \tau\big)$, $G\big((k_x, 0-1), \tau\big) = G\big((k_x, 2-1), \tau\big)$, $G\big((k_x, 0-0), \tau\big) = G\big((k_x, 2-2), \tau\big)$, and $G\big((k_x, 0-2), \tau\big) = G\big((k_x, 2-0), \tau\big)$ are used. To improve statistics and to obtain a smaller Trotter error (see Sec. 2.1.2, App. D), we do not use the symmetries, but we take all possible Green's functions in space. The Green's function $n$ is antisymmetric against exchange in $y$-direction, the two other ones are symmetric.

As a first check, we calculate the three Green's functions in the case $t_x = 0$ and a ferromagnetic background, leading to the three excitation energies at $\omega = \pm\sqrt{2}t_y$ and at $\omega = 0$. When $t_x$ is switched on, the three bands go over to three $2t_x\cos(k_x)$ bands, each one like holes in one dimension (see Fig. 6.1). Recall that the dispersion of free holes has the opposite sign of the one of free electrons. These results have been reproduced exactly by our algorithm.

### 6.2.2 The strong coupling limit

Like for the two-leg ladder it is helpful to consider the strong coupling limit. The discussion of the complete subsection is taken predominantly from a recent article by M. Y. Kagan *et al* [66]. The discussion is done in the electron picture.

#### The states on a single rung

For the single hole excitation spectrum on a single rung, the quantities, that have to be calculated are the ground state without holes (three electrons), and all states with one hole (two electrons). The ground state of a three-site Heisenberg antiferromagnet is a doublet with eigenstates given by

$$|\,\Psi_{i,0,\uparrow}\,\rangle = \frac{\sqrt{2}}{\sqrt{3}}\Big[-1/2(c^\dagger_{i,0,\uparrow}c^\dagger_{i,1,\uparrow}c^\dagger_{i,2,\downarrow}) + c^\dagger_{i,0,\uparrow}c^\dagger_{i,1,\downarrow}c^\dagger_{i,2,\uparrow} - 1/2(c^\dagger_{i,0,\downarrow}c^\dagger_{i,1,\uparrow}c^\dagger_{i,2,\uparrow})\Big]\,|\,v\,\rangle\,, \tag{6.6}$$

and its degenerate state $\Psi_{i,0,\downarrow}$ with opposite spin at all sites. The state $|\,v\,\rangle$ represents the vacuum, which is the state without electrons here. The energy of the Heisenberg ground state is $-3/2J_y$ per rung, or $-1/2J_y$ per site, and the states have odd parity with respect to reflection about the center leg.

For two electrons on a rung, there are two possibilities, given the quantization axis. The first one is two electrons with the same spin, what leads to the energies of free holes

$$\omega = \pm\sqrt{2}t_y,\ \omega = 0. \tag{6.7}$$

The other possibility are two electrons with opposite spin leading to the energies

$$\omega = \pm\sqrt{2}t_y,\ \omega = 0,\ \omega = -J_y,\ \omega = 1/2\big(-J_y \pm \sqrt{J_y^2 + 8t_y^2}\big). \tag{6.8}$$

The ground state energy is thus given by $\omega = 1/2\Big(-J_y - \sqrt{J_y^2 + 8t_y^2}\Big)$ with the ground state given by

$$|\,\Psi_{i,1}\,\rangle = \frac{1}{\sqrt{4+2\alpha_1^2}}\Big[c^\dagger_{i,0,\uparrow}c^\dagger_{i,1,\downarrow} - c^\dagger_{i,1,\downarrow}c^\dagger_{i,0,\uparrow} + \alpha_1 c^\dagger_{i,0,\uparrow}c^\dagger_{i,2,\downarrow} - \\ - \alpha_1 c^\dagger_{i,0,\downarrow}c^\dagger_{i,2,\uparrow} + c^\dagger_{i,1,\uparrow}c^\dagger_{i,2,\downarrow} - c^\dagger_{i,2,\downarrow}c^\dagger_{i,1,\uparrow}\Big]\,|\,v\,\rangle\,, \tag{6.9}$$

where $\alpha_{1,2} = -\frac{J_y \mp \sqrt{J_y^2+8t_y^2}}{2t_y}$. This state has even reflection parity.

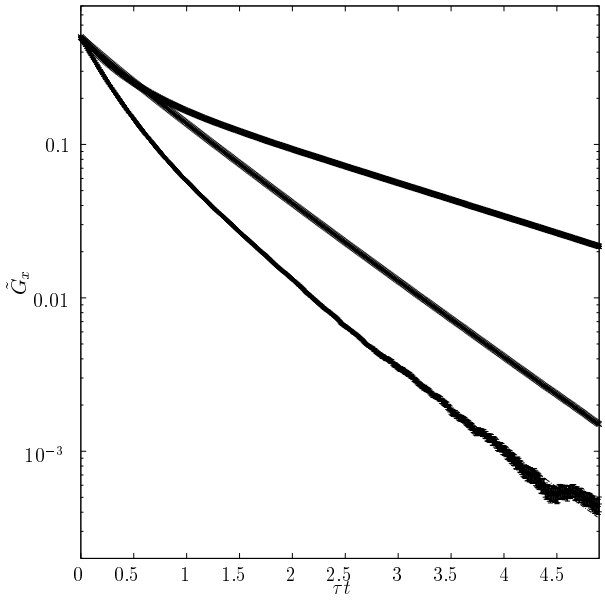


Figure 6.2: $\tilde{G}_x$ with $x = n, a, b$ from top to bottom for $Jy/t_y = 1$ and $J_x = t_x = 0$ and $\Delta\tau t_y = 0.01$. The Green's function can be fitted by $G_n = 1/4\exp(0.5x) + 1/8\exp(-1.5x) + 1/8\exp(-2.5x)$, $G_a = 9/32\exp(-0.086x) + 6/32\exp(-0.5x) + 1/32\exp(-2.91x)$ and $G_b = 2/32\exp(-0.086x) + 3/32\exp(-0.5x) + 5/32\exp(-1.5x) + 6/32 * \exp(-2.91x)$. The values in the exponentials are given by eq.(6.8 when $1.5J$ is added (the Heisenberg energy). The fits are given by full lines covered by the data points.

As a check, we reproduce the energies for the single rung (6.8) at $J = t$ by our QMC simulations (see Fig. 6.2). As the *Maximum Entropy* method has problems to resolve $\delta$-peaks exactly, we subtract the exponentials one by another from the Green's function as we did for the string excitations (see Sec. 4.3.3) in two dimensions, and for the better resolution of high-energy excitations (see Sec. 5.4) in the two-leg ladder. Here the result is exact, as the excitation energies are known, and we just have to resolve their weights, and check for consistence. We find, that the nonbonding band $n$ (at $J_y = t_y$) consists of excitations at $-0.5t_y$, $1.5t_y$, and $2.5t_y$, whereas the bonding band $b$ consist of $-\sqrt{2}t_y + 1.5t_y$, $0.5t_y$, and $\sqrt{2}t_y + 1.5t_y$ and the antibonding band $a$ has the contributions $-\sqrt{2}t_y + 1.5t_y$, $0.5t_y$, $1.5t_y$, and $\sqrt{2}t_y + 1.5t_y$ (see Fig. 6.3). The shift of the energy of eqs.(6.7,6.8) of $1.5t_y = 1.5J_y$ comes from the fact, that our reference energy is the Heisenberg ground-state energy with exactly this value.

As expected, the lowest excitation energy belongs to the antisymmetric band, as the lowest excitations changes the parity from odd ($|\,\Psi_{i,0,\sigma}\,\rangle$) to even ($|\,\Psi_{i,1}\,\rangle$).

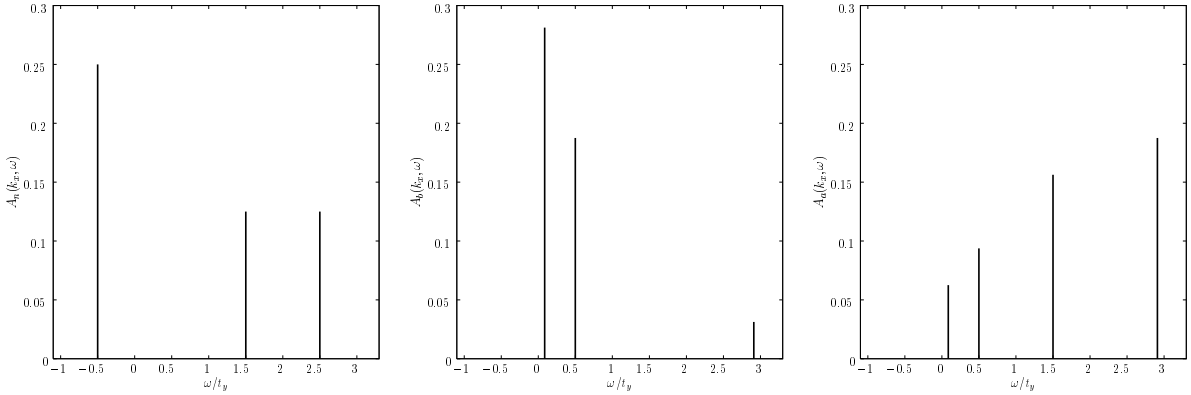

(a) Antisymmetric band $n$ (b) Symmetric band $b$ (c) Symmetric band $a$

Figure 6.3: Excitations at $J_y = t_y$ and $J_x = t_x = 0$ for the three bands.

**Effects of hopping $t_x \ll t_y, J_y$ along the chains**

The effective hopping along the chain for $t_x \ll t_y, J_y$ can now be derived, starting from the picture of weakly interacting rungs, by calculating

$$-t_x \sum_{a=(0,1,2),\sigma} c^\dagger_{i,a,\sigma} c_{i-1,a,\sigma} \,|\, \Psi_{i,1} \,\rangle \,|\, \Psi_{i-1,0} \,\rangle = t_{eff} \,|\, \Psi_{i-1,1} \,\rangle \,|\, \Psi_{i,0} \,\rangle \,, \tag{6.10}$$

where the states are given by eq.(6.6) and eq.(6.9) respectively. One finds, that the effective hopping $t_{eff}$ is given by

$$t_{eff} = \frac{3t_x}{4} \frac{\alpha_2}{\alpha_2 - \alpha_1} = \frac{3t_x}{8} \frac{J_y + \sqrt{J_y^2 + 8t_y^2}}{\sqrt{J_y^2 + 8t_y^2}}, \tag{6.11}$$

and therefore $t_{eff} < \frac{3}{4} t_x$.

An effective Hamilton operator for the hopping of the hole can now be obtained. Since for the low-energy physics the hopping of holes is equivalent to the hopping of states $|\, \Psi_{i,1} \,\rangle$ in a background of states $|\, \Psi_{i,0,\sigma} \,\rangle$, we can give an effective operator

$$\tilde{H}_{eff} = -t_{eff} \sum_{i,\sigma} P a^\dagger_{i,\sigma} a_{i-1} P, \tag{6.12}$$

where $a^\dagger_{i,\sigma}$ creates a state with a hole $|\, \Psi_{1,i} \,\rangle$ with simultaneous destruction of a state without holes $|\, \Psi_{0,i,\sigma} \,\rangle$, and $P$ projects the states to the physical Hilbert space, where two states $|\, \Psi_{i,1} \,\rangle$ cannot occupy the same site. The above Hamiltonian is equivalent to the Hubbard model (1.1) at $U = \infty$, or to the $t$-$J$ model (1.2) with $J = 0$ in one dimension. In this limit, the three-leg ladder thus falls into the universality class of a Luttinger liquid.

For low energies, the results for the one-dimensional $U = \infty$ Hubbard model [41,88,90] should describe the three-leg ladder with $J_x = 0$, $t_x \ll t_y, J_y$. As we have mentioned in

Chapter 3, this model can be well described by the simple charge-spin separation *Ansatz* (CSSA) [3, 40, 41] with $J_s = 0$ and $t_h = 2t_{eff}$. The parameters $J_y, t_y$ do not directly appear in the low-energy physics, but only in the effective hopping $t_{eff} = t_x f(\frac{J_y}{t_y})$.

**Effects of spin exchange $J_x$ along the chains**

We add an additional weak Heisenberg interaction along the chains with $J_x \ll J_y$. In this case the low-energy physics is solely governed by $J_x$ and the effective hopping along the chain is given by $t_{eff}$, as will be shown in the following.

Due to the large interactions $J_y$ the rungs form local states which are given by eq.(6.6) and by eq. (6.9), as above. The coupling on the rung, $J_y$ and $t_y$, then drops out of the low-energy physics. The spin exchange term between two rungs is given by

$$\begin{aligned}
\langle \Psi_{0,i,\sigma} | \langle \Psi_{0,i-1,\sigma} | J_x \sum_a \Big( \vec{S}_{i,a} \cdot \vec{S}_{i-1,a} - 1/4 \Big) | \Psi_{0,i,\sigma} \rangle | \Psi_{0,i-1,\sigma} \rangle &= 0 \\
\langle \Psi_{0,i,\sigma} | \langle \Psi_{0,i-1,-\sigma} | J_x \sum_a \Big( \vec{S}_{i,a} \cdot \vec{S}_{i-1,a} - 1/4 \Big) | \Psi_{0,i,-\sigma} \rangle | \Psi_{0,i-1,\sigma} \rangle &= +\frac{J_x}{2} \\
\langle \Psi_{0,i,-\sigma} | \langle \Psi_{0,i-1,\sigma} | J_x \sum_a \Big( \vec{S}_{i,a} \cdot \vec{S}_{i-1,a} - \frac{1}{4} \Big) | \Psi_{0,i,-\sigma} \rangle | \Psi_{0,i-1,\sigma} \rangle &= -\frac{J_x}{2}, \qquad (6.13)
\end{aligned}$$

so that the spin-spin interaction of two rungs $| \Psi_{0,i,\sigma} \rangle$ is exactly like that of a single Heisenberg chain. The hopping of states $| \Psi_{i,1} \rangle$ in the background of states $| \Psi_{0,j,\sigma} \rangle$ can be derived as above.

Finally one obtains a model as follows

$$H_{eff} = -t_{eff} \sum_i P a^\dagger_{i,\sigma} a_{i-1,\sigma} P + J_x \sum_i \Big( \tilde{\mathbf{S}}_i \cdot \tilde{\mathbf{S}}_{i-1} - 1/4 \tilde{n}_i \tilde{n}_j \Big). \qquad (6.14)$$

The operator $\tilde{\mathbf{S}}_i$ is the spin operator between two $S = 1/2$-rungs $| \Psi_{0,i,\sigma} \rangle$ given by $\tilde{\mathbf{S}}_\mathbf{i} = (1/2) \sum_{\alpha,\beta} a^\dagger_{i,\alpha} \vec{\sigma}_{\alpha,\beta} a_{i,\beta}$, and as above, $P$ projects the state to the physical one, where two states $| \Psi_{i,1} \rangle$ cannot site on the same site. The operator $\tilde{n}_i$ is the particle number operator for the states $| \Psi_{0,i,\sigma} \rangle$, and the term $-1/4 \tilde{n}_i \tilde{n}_j$ reduces to a constant in the case of half filling or doping with only one hole. This model is exactly the one-dimensional $t$-$J$ model (1.2). For the low-energy physics we thus expect very similar results for the three-leg ladder in the strong coupling limit and for one-dimensional systems (see Chapter 3), only the hopping should be rescaled from $t_x$ to the effective hopping $t_{eff}$. The main result for the single chain has been, that the spectral function can be well described by a charge-spin separation *Ansatz* (CSSA) given by eq.(3.1) on the overall energy scale.

This low-energy physics should be visible in the odd-parity channel of our results, as the low lying excitations of the hole change the parity of the rung and of the whole system, whereas the gapless excitations in the spin spectrum do not change parity [67].

When an electron is removed from a rung, which is in the (odd-parity) state $|\,\Psi_{i,0,\sigma}\,\rangle$ given by eq.(6.6), the excitations are as follows: The possibility with lowest energy is, that the hole goes into the even parity channel corresponding to the even-parity state $|\,\Psi_{i,1}\,\rangle$ given by eq.(6.9), changing the parity for the respective rung. Spin excitations with odd parity are not involved in that case. Spin excitations with even parity that are excited (e.g. due to momentum conservation for $k_x$) are gapless. The overall parity in this case changes from even to odd, as the number of rungs is even. In oder to remove an electron and retain the old parity, either the hole has to go into the odd parity channel, that costs additional energies $\sim t$, or, in case the hole goes to the even parity channel, one has to make an additional spin excitation with odd parity has to be produced, which has a spin gap $\sim J_y$.

At a first sight, the excitations with even parity thus correspond to a hole in an antiferromagnetic background, which is accompanied by a gapped spin excitation. These excitations are, at least at a first sight, very similar to those in the two-leg ladder. However, both the holes in the even and in the odd channel can interact with the gapless spin excitations with even parity. This leads to additional spin decay channels in the low-energy physics, that were absent in the two-leg ladder.

The main questions that arise are, up to which energies is the above low-energy picture correct, and can the isotropic case, like for the two-leg ladder, be well described by starting from the strong coupling limit. If the picture is valid, we expect that the low-energy physics for the odd parity channel resembles very much the chain systems, whereas, the overall distribution of spectral weight of the even parity excitations should be like the one of the two-leg ladder, with small corrections due to spin-hole interactions. The quasiparticle weight is a more delicate question, as the quasi one-dimensional spin excitation spectrum can interact with any parity. From this we conclude, that the quasiparticle weight should disappear in the thermodynamic limit for all parities in the spectral function.

## 6.3 The spectral function

In this section we discuss the spectral function both for the anisotropic strong coupling limit, and for the isotropic case.

In all cases, we give the complete spectral function (see Figs. 6.4, 6.5, and 6.6). We give the antisymmetric band $n$ and the two symmetric bands $b$ and $a$ in a separate figure, with the physical normalization of the area $\int_{-\infty}^{+\infty} d\omega A(\mathbf{k},\omega) = \pi/2$. Additionally, we give all three bands together in one figure, with the maximum of $A(\mathbf{k},\omega)$ for a fixed $\mathbf{k}$ normalized to 1, i.e we show $\frac{A(\mathbf{k},\omega)}{\max[A(\mathbf{k},\omega)]}$ as a function of $\omega/t$. In the first case, the distribution of weight can be better observed, whereas in the second case, it is easier to follow the overall structures. Especially it can be seen directly, at which $k$-points the bands cross each other. The unit of energy is $t \equiv t_x$. All energies are measured with respect to the Heisenberg ground state of the three-leg ladder, i.e. the Heisenberg ground state energy is fixed at $\omega/t = 0$.

### 6.3.1 The strong coupling limit

We first consider the strong coupling limit. Here we set $J_y/t_x = 1.6$, $t_y/t_x = 2$, and $J_x/t_x = 0.4$ (see Fig. 6.4). These parameters have already been used for the two-leg ladder in the strong coupling limit (see Sec. 5.3, Figs. 5.4 and 5.6 on pages 87f).

We start with the nonbonding band $n$, that -according to the strong coupling approximation in the previous section- should contain the low-energy physics, which is described by the effective model of eq.(6.14). The effective hopping can be derived from eq.(6.11), and is given by $t_{eff} = 0.48t_x$, the effective spin-exchange coupling remains $J_x$. For the antisymmetric band, we therefore expect to obtain similar results as for a hole in a single chain with $t_{eff}$ and $J_x$ (see Chapter 3).

The first point, that is in agreement with results in dimension, is the minimum of the dispersion at $k_x = \pi/2$. This has not been observed in the two-leg ladder at strong or isotropic coupling. The next question is the energy difference $\Delta$ between $k_x = 0$ and $k_x = \pi/2$, that is $J$ in the CSSA [41] for one dimension. Our result for the three-leg ladder is $\Delta = (0.4 \pm 0.1)t_x = J_x$ in perfect agreement with the one-dimensional CSSA.

We now compare the spectral function with the predictions of the CSSA for all values

of $k_x$ and $\omega/t$. As can be seen from Fig. 6.4, the lower edge is very well described by the CSSA for $0 \leq k_x \leq \pi/2$. For larger values of $k_x$, there are excitations at lower energies than predicted by CSSA. For the high-energy excitations, the CSSA breaks down completely. This is not surprising as the mapping of the three-leg ladder to an effective one-dimensional Hamilton operator is only reasonable for energies smaller than $t_y, J_y$. In this case, the excitations with high energies on the isolated rung are not accessible (see

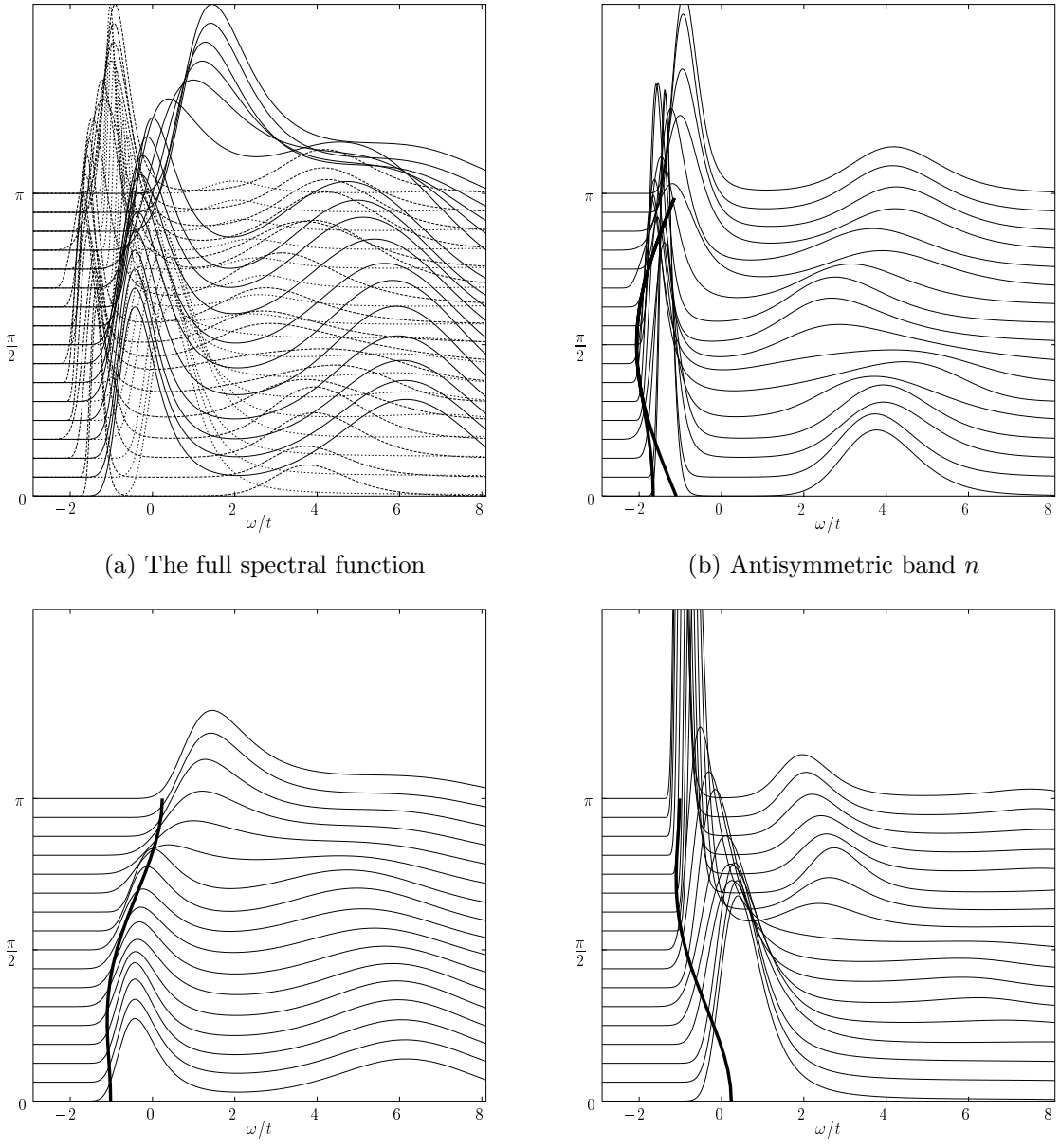


(a) The full spectral function

(b) Antisymmetric band $n$

(c) Symmetric band $b$

(d) Symmetric band $a$

Figure 6.4: The spectral function for $J_x/t_x = 0.4$, $J_y/t_x = 1.6$, $t_y/t_x = 2$, and $N = 32 \times 3$. The full lines represent the lower edge as obtained from the CSSA for a one-dimensional $t$-$J$ model with $J = J_x$, $t = t_{eff} = 0.48$ (b), and to the quasiparticle corresponding to $\epsilon_{1/2}$ as obtained by O. P. Sushkov for the isotropic two-leg ladder with $J = 0.4t$ (c,d).

eqs.(6.7,6.8)). These higher excitations have a gap of $3.74t_x$ and $5.88t_x$ respectively for the parameters we consider here. From our results, the peak maximum at high energies has a distance of about $\omega/t = 5$ to that of the low-energy spectrum. From this we conclude, that in the strong coupling limit, the low excitations of the nonbonding band are well described by the effective one-dimensional $t$-$J$ model, whereas the higher excitations can be understood as excitations on an isolated rung.

We now address the two symmetric bands. The first point, that emerges from the analytic calculations in the strong coupling limit is the difference in energy for the lowest excitation of the symmetric band to the one of the antisymmetric band. From eq.(6.8) one obtains $\sqrt{2}t_y - \frac{1}{2}\left(-J_y - \sqrt{J_y^2 + 8t_y^2}\right) = 0.89t_x$, which again is consistent with the data.

As we have seen in the previous section, there are some hints, that the excitation spectra of the two symmetric bands resemble that of a two-leg ladder. A comparison to the strong coupling limit of the two-leg ladder shows similarities, like the minima of the dispersions for the antibonding band at $k_x = 0$, but the overall structures of the symmetric bands in Fig. 6.4 at low energies resemble more the isotropic two-leg ladder at $J/t = 0.4$ (see Fig. 5.13). The symmetric bands in an anisotropic three-leg ladder are thus similar to the isotropic two-leg ladder for the considered values of $J, t$.

This similarity becomes more evident, when one uses the dispersions, that O. P. Sushkov [64] finds in his perturbational analysis of the two-leg ladder (see Sec. 5.3.2). The symmetric bands follow the dispersion of $\epsilon_{1/2}$ (eq.(5.12)) very well, where in the bonding case, we shift the dispersion $\epsilon_{1/2}$ by $k_x = \pi$. This shift can be identified with a gapless spin excitation having momenta $k_x = \pi$ and even parity (see App. C). In other words, the low-energy spectra of the bonding band and the antibonding band are shadows to each other, connected by a magnon. Different from the two-leg ladder, one cannot say, which band is the *original* one, as in the single rung limit (see Fig. 6.3), both excitations have the same minimal energy.

The high-energy excitations for the symmetric bands can be explained by the single rung limit. Excitations are, among others, expected at $\sqrt{2}t_y = 2.83t_x$ and $2\sqrt{2}t_y = 5.66t_x$ above the low-energy peak. In the antibonding band, we see numerical evidence for the first excitation, around $k_x = \pi$, whereas in the bonding band an excitation with a gap around $6t_x$ can be observed around $k_x = 0$.

Summarizing, the low-energy physics of the antisymmetric band of the three-leg ladder with strong coupling on the rung can be well described by the effective model (6.14) obtained pertubatively from the isolated rung limit. This effective model is equivalent to the one-dimensional $t$-$J$ model, that has been considered in Chapter 3. We have shown, that the *model of the model* in one dimension is given by a charge-spin separation *Ansatz*. The low-energy physics of the two symmetric bands one the other hand can be well described by another effective model, which is given by a $t$-$J$ two-leg ladder.

### 6.3.2 The isotropic case

We first consider the isotropic chain with $J/t = 0.4$. For these parameters, the effective hopping along the chain is, according to eq.(6.11), given by $t_{eff} = 0.43t$. In the case, that the isolated rung picture is still observable in the isotropic case, the three excitations in the antisymmetric band should be localized at $-1.23t + c$, $0.6t + c$ and $1.83t + c$, where $c$ is some constant due to the intra-chain hopping and intra-chain spin exchange[1]. For the two symmetric bands one has $-0.82t + c$, $0.2t + c$ and $2.01t + c$ (see eqs.(6.7,6.8)). The symmetric and the antisymmetric bands are thus only gapped by about $0.4t$, This can be taken as an upper energy bound for the validity of the effective Hamilton operator (6.14). The numerical results are presented in Fig. 6.5.

According to the strong coupling limit analysis, and to exact diagonalizations [67], the antisymmetric band $n$ is very similar to that of a one-dimensional $t$-$J$ model, where the dispersion obtained by exact diagonalizations is like the one of a one-dimensional $t$-$J$ model with the same parameters $t$ and $J$ (our QMC calculations for the same size of $8 \times 3$ lattice points are consistent with exact diagonalizations), whereas from the strong coupling limit one obtains an effective hopping of $t_{eff} = 0.43t$. The lower edge of the spectral function between $k_x = 0$ and $k_x = \pi/2$ should in both cases have the energy difference of $J = 0.4t$. This result is consistent with our numerical data, which gives $(0.3 \pm 0.2)t$. At $\pi/2 \leq k_x \leq \pi$, the CSSA in one dimension predicts a dispersion $\sim t$, what cannot be observed from our data (around $k_x = \pi$ one should notice, that the quality of the QMC data is rather poor, leading probably to the extremely flat peaks).

[1] When the isolated rung picture is valid, the dynamics along the rungs and along the chains are decoupled, and therefore, the constant $c$ is the same for all energy levels on the rung.

Overall, the effective Hamiltonian (6.14) works not so well like in the strong coupling case presented before. In the small $8 \times 3$ lattice of exact diagonalization, the correspondence works far better, but it is important to notice, that the spin excitations for this system have a large finite-size gap of $\Delta \approx 0.4J$.

When we consider the low-energy spectrum of the two symmetric bands, the bonding and the antibonding one, we first observe, that both bands are not well separated from

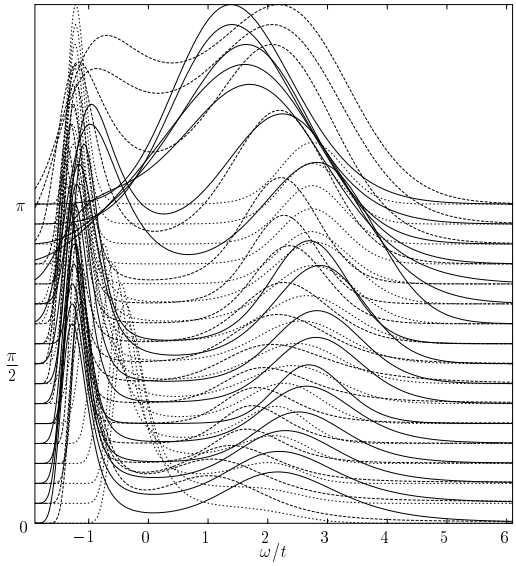


(a) The full spectral function

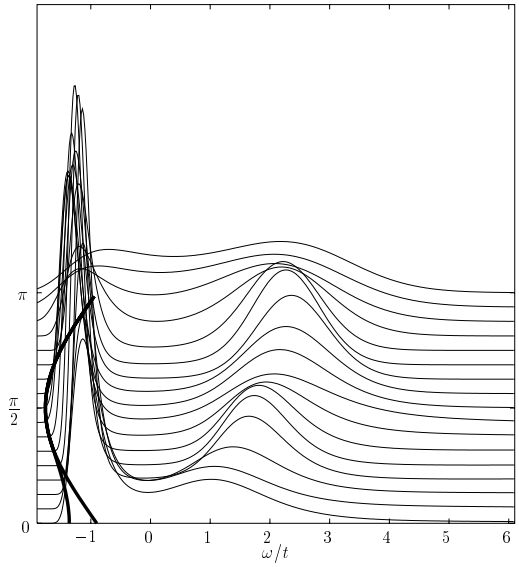


(b) Antisymmetric band $n$

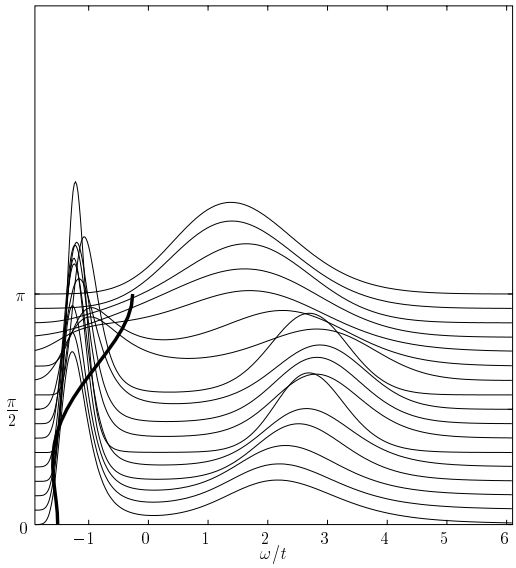


(c) Symmetric band $b$

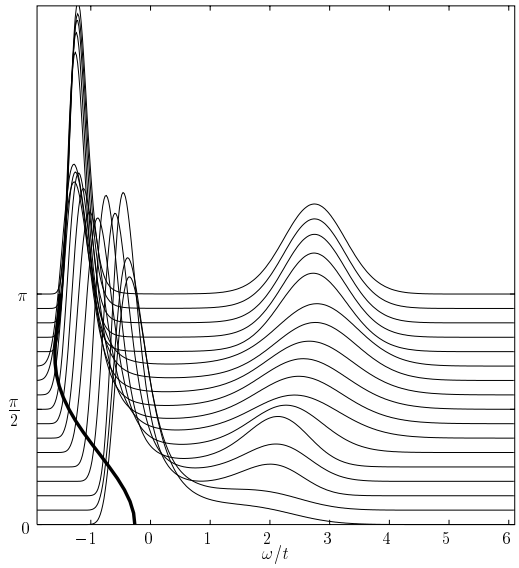


(d) Symmetric band $a$

Figure 6.5: The spectral function for $J/t = 0.4$ and $N = 32 \times 3$. The full lines represent the lower edge as obtained from the CSSA for a one-dimensional $t$-$J$ model with $J = J_x$, $t = t_{eff} = 0.43$ (b), and to the quasiparticle corresponding to $\epsilon_{1/2}$ as obtained by O. P. Sushkov [64] for the isotropic two-leg ladder with $J = 0.4t$ (c,d).

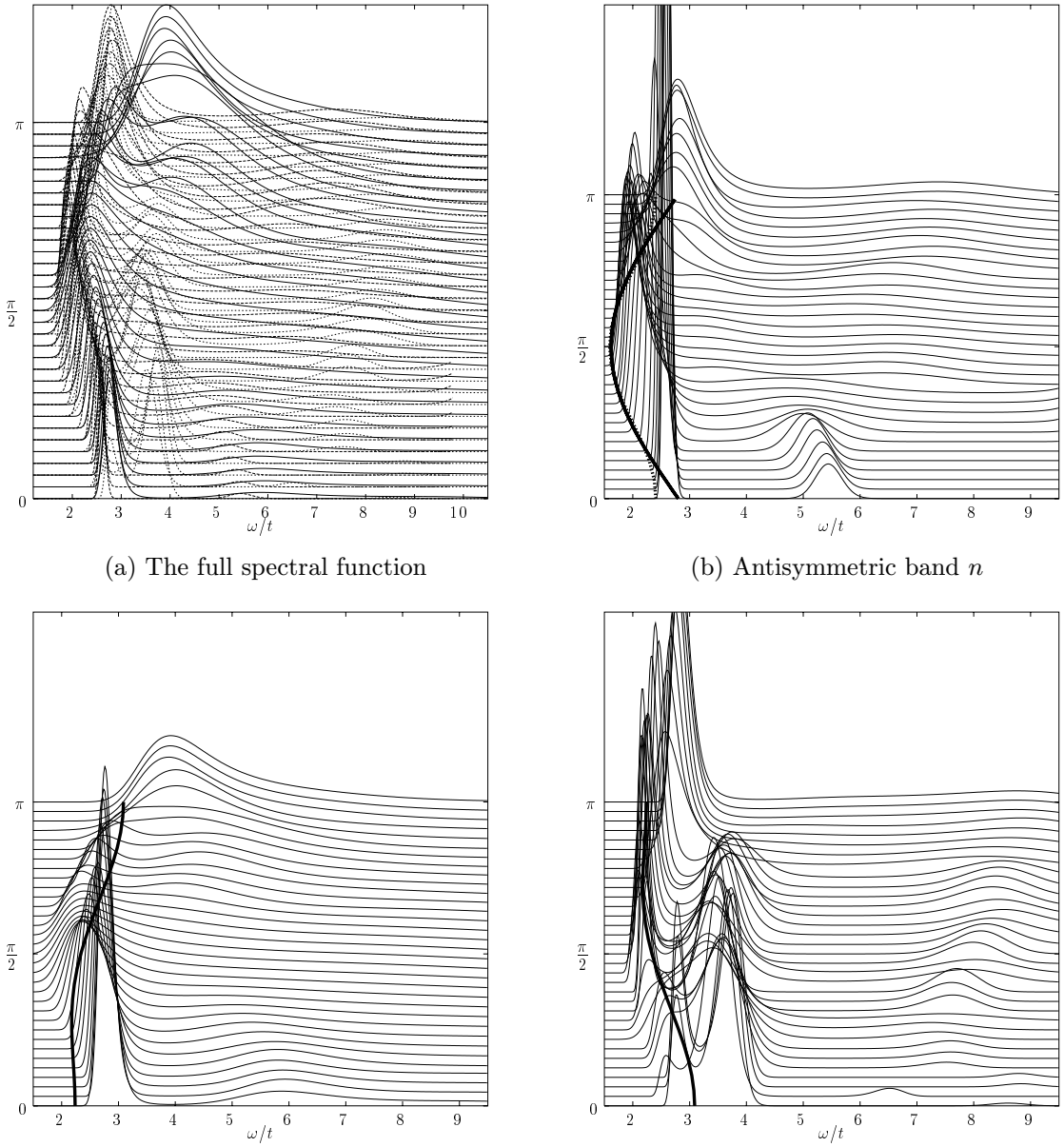


(a) The full spectral function

(b) Antisymmetric band $n$

(c) Symmetric band $b$

(d) Symmetric band $a$

Figure 6.6: The spectral function for $J/t = 2$ and $N = 64 \times 3$. The full lines represent the lower edge as obtained from the CSSA for a one-dimensional $t$-$J$ model with $J = J_x$, $t = t_{eff} = 0.59$ (b), and to the quasiparticle corresponding to $\epsilon_{1/2}$ as obtained by O. P. Sushkov [64] for the isotropic two-leg ladder with $J = 2t$ (c,d). In (b) we additionally give the dispersion of a Bethe-*Ansatz* holon [92] (dotted line).

the antisymmetric band in energy like in the strong coupling limit, but all three bands overlap. Given the resolution of our simulations $\approx 0.1t$, we cannot clarify exactly, which of the three bands includes the state with minimal energy. On the other hand, the two symmetric bands can be rather well described by the quasiparticle dispersion, that Sushkov obtains for the isotropic two-leg ladder. Especially in the antibonding band, the

fit works amazingly well.

The high-energy excitations for all three bands are gapped by about $4t$, and no significant relation to the single rung excitations can be observed. We therefore identify these excitations with incoherent processes that scale with $t$. A comparison of the antisymmetric band with the two-dimensional $t$-$J$ model at $J/t = 0.4$ shows a striking similarity of the spectral function around $\mathbf{k} = (\pi, 0)$ (see Fig. 4.11 on page 61) both at low and high energies.

When we consider the supersymmetric point $J = 2t$ (see Fig. 6.6), the first remarkable difference to the topologies discussed in the previous chapters is the absence of the single $\delta$-singularity at $\mathbf{k} = 0$. This can be understood quite easily, as the proof given in App. A is no longer applicable. None of the three bands' Green's functions (6.5) consists of a simple sum over the Green's functions in space (2.15), as it is the case for $k_x = k_y = 0$ in the previously discussed topologies. Remainders of the effect are however still visible, as all bands are extremely sharp around $k_x = 0$. For the supersymmetric point, the effective hopping from the strong coupling limit is given by $t_{eff} = 0.59 t_x$. We therefore expect both from the CSSA and from a general discussion of Luther-Emery models [9, 42, 43] (if the strong coupling limit is applicable), that the lower edge of the spectral function is only given by the holon dispersion. At least at $k_x < 3\pi/4$, the lower edge can be fitted quite well with the Bethe-*Ansatz* holons [92] for the supersymmetric point when the width of the dispersion is rescaled by $\frac{t_eff}{t}$. This is quite surprising, as the effective model (6.14) for the three-leg ladder is not at the supersymmetric point, as $\frac{J}{t_{eff}} = 3.77 \neq 2$.

The two symmetric bands are no longer described well by an effective two-leg ladder model. The minimal energies for all three bands are at $k_x = \pi/2$, where the bands $n$ and $b$ are degenerate at this point, and band $a$ is about $t$ higher in energy.

The higher excitations have little weight. At the $k$-points, where they can be resolved properly, they are again gapped by about $4t$.

As we have seen above, the nonbonding band in the isotropic three-leg ladder can be described by the effective one-dimensional model (6.14) as long as the energies of the bonding and the antibonding band are well separated. Therefore, the lower edge of the spectrum can be well described by the CSSA at the supersymmetric point $J/t = 2$ where this is the case, whereas at small values of $J/t = 0.4$, the effective model only works well around the minimum of the nonbonding band. The antibonding band, and

to some extend the bonding band, are well described by an effective two-leg ladder for small values of $J/t$ on the overall energy scale, whereas this is not the case at $J/t = 2$.

## 6.4 The quasiparticle weight

We consider the three-leg ladder at the supersymmetric point, i.e. $J/t = 2$, where the minimum of the dispersion is at $k_x = \pi/2$ for all three bands. Recall, that for that value, we have obtained large quasiparticle weights for two dimensions ($Z(\pi/2, \pi/2) = 50\%$) and for the two-leg ladder ($Z(\pi/2, 0) = 70\%$), whereas in the one-dimensional case, we obtained a vanishing quasiparticle weight. In Sec. 6.2.2 we derived a one-dimensional effective model (6.14) for the three-leg ladder. As we have shown in Sec. 3.5 on page 47, the quasiparticle weight in one dimension and $J/t = 2$ vanishes as $1/\sqrt{L}$ at wave vector $k = \pi/2$. For the three-leg ladder, we thus consider the same wave vector, and perform the finite-size scaling versus $1/\sqrt{L}$. We consider both the antisymmetric band $n$ and the two symmetric bands $a$ and $b$. The way the quasiparticle, given a specific system length, is obtained is exactly performed as in the previous chapters. The finite-size scaling for the

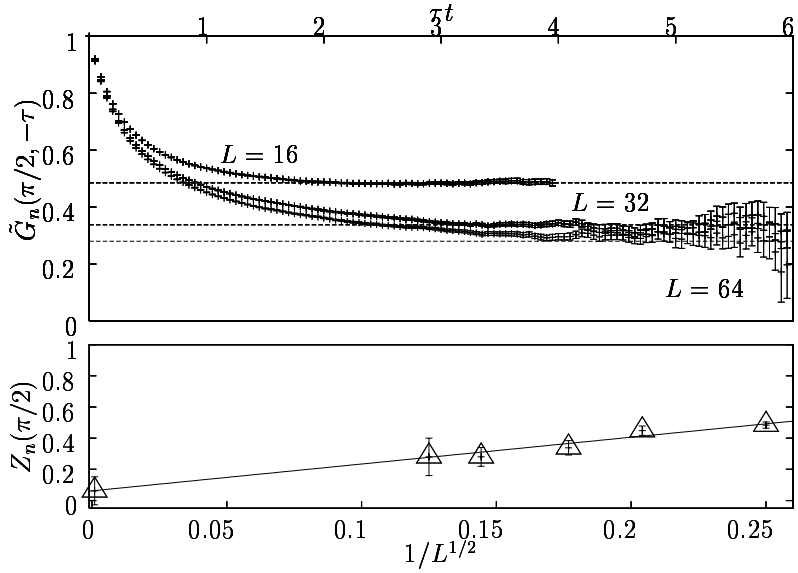


Figure 6.7: The quasiparticle weight for the antisymmetric band $n$. The upper figure shows the Green's function, rescaled by a single exponential to obtain a horizontal for $\tau t \to \infty$. The intersect of this horizontal is the quasiparticle weight $Z_n(\pi/2)$ for the respective system length $L$. The lower figure shows the finite-size scaling of the intersects. The line represents the result of the least-square fit.

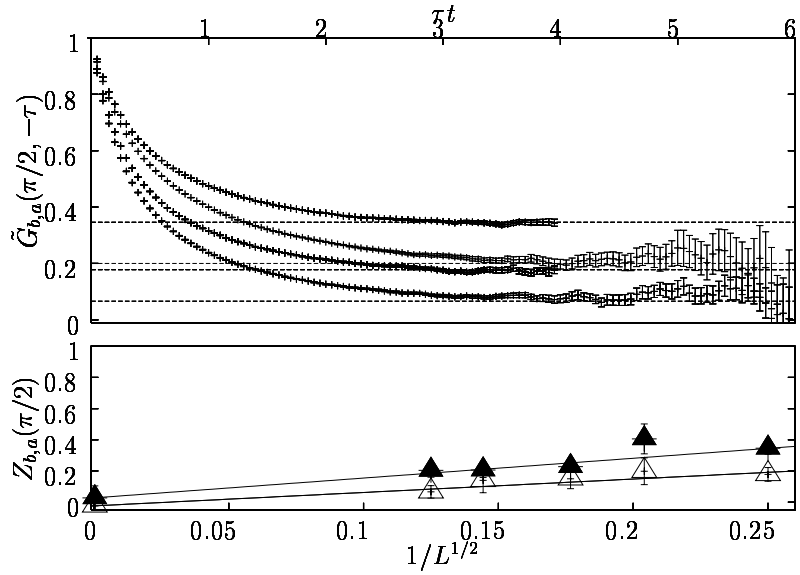


Figure 6.8: The quasiparticle weight for the symmetric bands $b$ and $a$. The upper figure shows the Green's function, rescaled by a single exponential to obtain a horizontal for $\tau t \to \infty$. The curves correspond to (from top to bottom) $L = 16$, $L = 64$ in the antibonding band, and $L = 16$, $L = 64$ in the bonding band. The intersect of the horizontal is the quasiparticle weight $Z_{b,a}(\pi/2)$ for the respective system length $L$. The lower figure shows the finite-size scaling of the intersects. The line represents the result of the least-square fit. Again, the upper curve represents band $a$, the lower one $b$.

antisymmetric band is given in Fig. 6.7, and the finite-size scaling for the two symmetric bands is given in Fig. 6.8.

A least square fit of $Z_n(L)$ versus $L^{-1/2}$ in the nonbonding band leads to the value $Z_n(\pi/2) = 0.06 \pm 0.09$ in the thermodynamic limit. For the two symmetric bands, we obtain $Z_b = -0.02 \pm 0.08$ and $Z_a = 0.03 \pm 0.07$, respectively.

Our results thus show, that the quasiparticle weight vanishes in the thermodynamic limit for all three bands. The three-leg ladder shows the properties of Luttinger liquid, which has a completely different scaling from that found in the two-leg ladder. At least for the bonding band, this result was already expected from the effective model (6.14), which predicts such a Luttinger liquid state. In the two symmetric bands, whose lower edges, at least in the strong-coupling limit, were well described by an effective two-leg ladder model, this result is to some extent surprising. We see, that although the overall spectral function cannot be described by the simple one-dimensional model, which is used in the nonbonding band, the existence of the gapless spin excitation spectrum alone

suffices for a vanishing quasiparticle weight in the quasi one-dimensional three-leg ladder.

# Chapter 7

# Summary and Conclusions

In this work, we developed a new quantum Monte Carlo algorithm capable of evaluating single particle Green's functions in imaginary time for the $t$-$J$ model at half filling. The algorithm consists of a combination of a loop algorithm, which has proven to be extremely successful for non-frustrated spin systems, and ideas from projector quantum Monte Carlo, such as integrating out the fermions. The algorithm is free of the minus-sign problem at half filling, and exact in the sense, that the systematic $\Delta\tau$-error and the statistical error from the Quantum Monte Carlo summation can be controlled by taking $\Delta\tau \to 0$ and the number of Monte Carlo steps $N \to \infty$.

These data can then be used to evaluate dynamical quantities, that are accessible by experiment with the help of the *Maximum Entropy* method. We further use this data to evaluate the quasiparticle weight and the lower edge of the spectral function directly.

The algorithm has been applied to four different topologies, the one-dimensional chain, the two-dimensional square lattice, the two-leg ladder, and the three-leg ladder. All these systems show a substantially different low- and high-energy behavior. Whereas this is not surprising in going from one to two dimension, the large differences between two- and three-leg ladders are not obvious from the beginning. Both systems are quasi-one-dimensional, but they show a substantially different spin excitation spectrum, namely a spin gap in the two-leg ladder, and its absence in the three-leg ladder.

In one dimension, the numerical results can be described by a simple charge spin separation *Ansatz*. This picture seems to be valid over the whole energy scale and for values of $J/t$ going from 0.33 to 2. At the supersymmetric point, the lower edge of the

spectral function is given very accurately by the holon dispersion, that is obtained from Bethe-*Ansatz*. We further show explicitly, that the quasiparticle weight vanishes as $1/\sqrt{L}$ with system size as predicted by analytical calculations.

In the two-dimensional case, we show, that self-consistent Born approximation gives accurate results for small $J/t$, whereas series expansion is very reliable for large values of $J/t$. We obtain flat bands in the spectrum around wave vector $\mathbf{k} = (\pi, 0)$, and a minimum of the dispersion at $\mathbf{k} = (\pi/2, \pi/2)$. The essential structures of the spectral function do not change much for $0.4 \leq J \leq 4$. Next to the low energy peak around $\mathbf{k} = (\pi/2, \pi/2)$, we can observe a resonance, which is identified with a string excitation. The distance in energy between the low energy peak and the string resonance scales as $J^{2/3}$ in agreement with self-consistent Born approximation. We finally demonstrate, that the quasiparticle weight in two dimensions is finite in the thermodynamic limit, and that its value is consistent with the self-consistent Born approximation for small values of $J/t$. At exactly half filling, the $t$-$J$ model in two dimensions is thus a Fermi liquid.

The last two chapters concentrate on two quasi-one-dimensional systems, the two-leg ladder and the three-leg ladder. For the first system it is known, that it has a rather large spin gap, whereas the second one has gapless spin excitations. At exactly half-filling, where charge excitations are absent, one thus expects the two-leg ladder to be a Fermi liquid, whereas the three-leg ladder should be described by a Luttinger liquid like the one dimensional $t$-$J$ model at half filling. For both ladder systems it is useful to consider the strong coupling limit (i.e the inter-chain coupling is larger than the intra-chain coupling) first. For the two-leg ladder, the strong coupling picture holds up to the isotropic case, whereas in the three-leg ladder, it fails to describe more than the lowest excitations in this case. The explicit calculation of the quasiparticle weight reveals, that in the two-leg ladder, the quasiparticle weight is large, whereas for the three-leg ladder, the results are consistent with a vanishing quasiparticle weight, as expected for a Luttinger liquid.

# Appendix A

# $A(k,\omega)$ at $k=0$ for the supersymmetric point

The QMC simulations have shown, that $A(k,\omega)$ shows a $\delta$-like excitation at $k=0$ for $J=2t$. The numerical data further show, that this $\delta$ excitation is quite robust, when going away from $J=2t$, or $k=0$. This $\delta$-excitation has already been found in an earlier work by S. Sorella [137], but to my knowledge it has never been exploited as a numerical benchmark. When considering eq.(2.22), one can see, that the $\delta$-excitation is produced by a single exponential form of the Green's function. In the following it will be proven analytically, that at $J/t=2$ the Green's function at $k=0$ is exactly given by

$$G(k=0,\tau)=\exp(-2d\tau t)/2, \tag{A.1}$$

where $d$ is the dimension in space. The factor $1/2$ originates from the constraint.

We consider the evolution of the one-hole imaginary time Green's function at an arbitrary time step in one dimension. The Green's function at $k=0$ is given by:

$$\begin{aligned} G(k=0,\tau+\Delta\tau) &= \sum_{\vec{\sigma}}\sum_{x} G(x,\tau+\Delta\tau,\vec{\sigma}) = \\ &\sum_{\vec{\sigma}} P(\vec{\sigma}) \sum_{x} \frac{\langle\, v \,|\otimes\langle\, \sigma_{n+1}\,|\, f_x e^{-\Delta\tau\tilde{H}}\ldots e^{-\Delta\tau\tilde{H}} f_0^{\dagger}\,|\,\sigma_{m,0}\,\rangle\otimes|\, v\,\rangle}{\langle\,\sigma_{n+1}\,|\,e^{-\Delta\tau H}\,|\,\sigma_{n+1}\,\rangle\ldots\langle\,\sigma_1\,|\,e^{-\Delta\tau H}\,|\,\sigma_0\,\rangle} = \\ &\sum_{\vec{\sigma}} P(\sigma) \sum_{x}\sum_{i} \\ &\qquad \frac{\langle\, v\,|\,\langle\,\sigma_{n+1}\,|\, f_x e^{-\Delta\tau\tilde{H}}\left[f_i^{\dagger}\,|\,\sigma_n\,\rangle\,|\, v\,\rangle\langle\, v\,|\,\langle\,\sigma_n\,|\, f_i\right]\ldots e^{-\Delta\tau\tilde{H}} f_0^{\dagger}\,|\,\sigma_{m,0}\,\rangle\,|\, v\,\rangle}{\langle\,\sigma_{n+1}\,|\,e^{-\Delta\tau H}\,|\,\sigma_{n+1}\,\rangle\langle\,\sigma_n\,|\,e^{-\Delta\tau H}\,|\,\sigma_{n-1}\,\rangle\ldots\langle\,\sigma_1\,|\,e^{-\Delta\tau H}\,|\,\sigma_0\,\rangle}. \end{aligned} \tag{A.2}$$

We introduce the abbreviation $U(x,i,\sigma_{n+2},\sigma_{n+1},\sigma_n)$ for the propagation in a single time step and define

$$U(x,i,\sigma_{n+2},\sigma_{n+1},\sigma_n)=\sum_j u(x,j,\sigma_{n+2},\sigma_{n+1})u(j,i,\sigma_{n+1},\sigma_n), \tag{A.3}$$

where $u(i,j,\sigma_{m+1},\sigma_m)$ corresponds to the propagation on one plaquette. With that we obtain:

$$\begin{aligned}
G(k=0,\tau+\Delta\tau) &= \sum_{\vec\sigma} P(\vec\sigma)\sum_x\sum_i G(i,\tau,\vec\sigma)U(x,i,\sigma_{n+1},\sigma_n)\\
&= \sum_{\vec\sigma} P(\vec\sigma)\sum_i\sum_{x(i)} G(i,\tau,\vec\sigma)U(x,i,\sigma_{n+1},\sigma_n)\\
&= \sum_{\vec\sigma} P(\vec\sigma)\sum_i\sum_{j(i)}\sum_{x(j)} G(i,\tau,\vec\sigma)u(x,j,\sigma_{n+2},\sigma_{n+1})u(j,i,\sigma_{n+1},\sigma_n)\\
&= \sum_{\vec\sigma} P(\vec\sigma)\sum_i G(i,\tau\sigma)\exp(-\Delta\tau t)\exp(-\Delta\tau t)
\end{aligned} \tag{A.4}$$

The value of the Green's function with the spin background $\vec\sigma$ at $\tau=0$ is given by $G(i,\tau=0,\vec\sigma)=\delta(i=0)$, when the constraint is fulfilled. In the case, that the constraint is violated we set $G(i,\tau=0,\vec\sigma)=0$. Therefore we arrive by induction at

$$G(k=0,\tau)=\frac{1}{2}\sum_{\vec\sigma} P(\vec\sigma)\exp(-2\tau t)=\exp(-2\tau t)/2. \tag{A.5}$$

It has still to be shown, that $\sum_x U(x,i,\sigma_{n+2},\sigma_{n+1},\sigma_n)$ reduces to $\exp(-\Delta\tau 2t)$ for all possible spin configurations. As can be seen from eq.(A.4) it is sufficient to consider the two partial time steps separately, i.e. to show $\sum_j u(j,i,\sigma_{n+1},\sigma_n)=\exp(-\Delta\tau t)$ and $\sum_x u(x,j,\sigma_{n+2},\sigma_{n+1})=\exp(-\Delta\tau t)$. We consider the first partial step[1], and first notice, that $j$ and $i$ have to be on the same plaquette for a non-vanishing propagator $u(j,i,\sigma_{n+1},\sigma_n)$. The exact values for $u(j,i,\sigma_{n+1},\sigma_n)$ can be seen in Table 2.1 on page 35. The case of all pseudospins $\uparrow$ has to be neglected, as in this case, no propagation occurs, as the constraint is violated. In the case of one pseudospin $\downarrow$, and one $\uparrow$, the propagation is either given by $\cosh(\Delta\tau t)/\big(\exp(\Delta\tau J/2)\cosh(\Delta\tau J/2)\big)$ or by $\sinh(\Delta\tau t)/\big(\exp(\Delta\tau J/2)\sinh(\Delta\tau J/2)\big)$. For $J=2t$ this reduces to $\exp(-\Delta\tau t)$ in both cases. The last possibility is to have only pseudospin $\downarrow$ on the plaquette. In this case we obtain

$$\sum_j u(j,i,\sigma_{n+1},\sigma_n)=\cosh(\Delta\tau t)-\sinh(\Delta\tau t)=\exp(-\Delta\tau t). \tag{A.6}$$

[1]The proof for the second partial step is exactly the same.

We thus showed, that $\sum_j u(j,i,\sigma_{n+1},\sigma_n) = \exp(-\Delta\tau t)$ for all possible spin backgrounds, and therefore

$$\sum_i U(x,i,\sigma_{n+2},\sigma_{n+1},\sigma_n) = \sum_{i,j} u(x,j,\sigma_{n+2},\sigma_{n+1})u(j,i,\sigma_{n+1},\sigma_n) = \\ = \exp(-\Delta\tau t)\exp(-\Delta\tau t) = \exp(-2\Delta\tau t) \quad \text{(A.7)}$$

The above approach can easily extended to higher dimensions on any bipartite lattice. The value of $\sum_x U(x,i,\sigma_{n+1},\sigma_n)$ in 2D is simply given by the one-dimensional case squared[2].

[2]In the case of $2t_x = J_x \neq J_y = 2t_y$ the Green's function is given by $\exp(-2\Delta\tau t_x)\exp(-2\Delta\tau_y)$. The isotropic two-leg ladder corresponds to a two-dimensional system with $J_y/J_x = t_y/t_x = 0.5$

# Appendix B

# The linear string potential

## B.1 The linear confining potential for the $t$-$J_z$ model

In the following we show, how one can derive a linear confining potential for a single hole in the $t$-$J_z$ model. We will closely follow the ideas of B. Shraiman and E. Siggia [56] based on the retraceable path approximation [95]. We start with the $t$-$J_z$ model

$$H_{t-J_z} = -t \sum_{<ij>} (\tilde{c}^{\dagger}_{i,\sigma} c_{j,\sigma} + H.c) + J_z \sum_{<ij>} S^z_i S^z_j, \tag{B.1}$$

where the sum runs over nearest neighbours only. Starting from a state with one hole, which is localized at one site in the Néel state, successive applications of the kinetic term create a series of states. These states can be labeled as a string of broken bonds $|\,\tau_1, \tau_2, \ldots, \tau_l\,\rangle$, where $\tau_{m+1} \neq \tau_m$ and ech $\tau_m$ indicates the direction of the hopping of the hole. In two dimension this is upwards, downwards, right and left (coordination number $z = 4$). We further define *raising* and *lowering* operator as

$$\begin{aligned} h^{\dagger}\,|\,\tau_1, \tau_2, \ldots, \tau_l\,\rangle &= 1/\sqrt{3} \sum_{\tau_{l+1} \neq \tau_l} |\,\tau_1, \tau_2, \ldots, \tau_l, \tau_{l+1}\,\rangle \\ h\,|\,\tau_1, \tau_2, \ldots, \tau_l\,\rangle &= 1/\sqrt{3}\,|\,\tau_1, \tau_2, \ldots, \tau_{l-1}\,\rangle\,, \end{aligned} \tag{B.2}$$

where $h\,|\,0\,\rangle = 0$ and $h^{\dagger}\,|\,0\,\rangle - 1/\sqrt{3} = \sum_{\tau_1} |\,\tau_1\,\rangle$. The kinetic energy is now given by $-\sqrt{3}t(h^{\dagger} + h)$, and a set of orthonormal states is defined as $|\,l\,\rangle = 1/2\sqrt{3}(h^{\dagger})^l\,|\,0\,\rangle$. When we exclude walks of the hole, where the path touches itself, the Hamiltonian (B.1) is

given by

$$
\begin{aligned}
H\,|\,0\,\rangle &= -2t\,|\,1\,\rangle + J_z\,|\,0\,\rangle \\
H\,|\,1\,\rangle &= -2t\,|\,0\,\rangle - \sqrt{3}t\,|\,2\,\rangle + 5/2J_z\,|\,1\,\rangle \\
H\,|\,l\,\rangle &= -\sqrt{3}t\big(|\,l-1\,\rangle + |\,l+1\,\rangle\big) + \big(3/2+l\big)J_z\,|\,l\,\rangle\,.
\end{aligned}
\tag{B.3}
$$

This equation can now either be solved numerically, leading to a ground state energy of $E = -2\sqrt{3} + 2.74J_z^{2/3}$ for $J_z \leq 1$ [56]. In the limit $J \to 0$ eq.(B.3) can be mapped on the problem of a particle in a linear potential. As the average length $l$ of the path of the hole will be long in this case, we can neglect the first two lines in eq.(B.3), and the term $3/2$ in the third line. We then obtain

$$
H\,|\,l\,\rangle = -\sqrt{3}t\big(|\,l-1\,\rangle - |\,l\,\rangle + |\,l+1\,\rangle - |\,l\,\rangle\big) - 2\sqrt{3}t\,|\,l\,\rangle + J_z l\,|\,l\,\rangle \tag{B.4}
$$

In the continuum limit, this can be written as ($x \geq 0$)

$$
H_{\mathrm{S}} = -t\frac{\partial^2}{\partial x^2} + J_z x - 2\sqrt{3}t. \tag{B.5}
$$

## B.2 The solutions of a linear potential

The quantum mechanical problem of a particle in a linear potential is solved in most basic textbooks. The solution of this problem is nevertheless not trivial, so that we give a short solution, following the textbook by R. W. Robinett [138].

When eq.(4.1,B.5) is compared to the textbook problem

$$
\frac{-\hbar^2}{2m}\frac{\partial^2}{\partial x^2}\Psi(x) + Fx\Psi(x) = E\Psi(x), \tag{B.6}
$$

one can identify $\hbar^2/2m$ with $t$ and $J_z$ with $F$. In a second step one defines auxiliary variables given by $\rho = \left(\frac{\hbar^2}{2mF}\right)^{1/3} = \left(\frac{t}{J_z}\right)^{1/3}$ and the classical turning point $\sigma = E/F = E/J_z$. Together with $x = \rho y + \sigma$, one finds the resulting differential equation

$$
\frac{\partial^2}{\partial y^2}\Psi(y) = y\Psi(y). \tag{B.7}
$$

This is the known Airy equation, with the solutions given by $A_i(y)$ and $B_i(y)$. The second solution diverges for $y, x \to \infty$ and is therefore discarded. This leads to the solutions in the original coordinate

$$
\Psi(x) = NAi\left(\frac{x-\sigma}{\rho}\right). \tag{B.8}
$$

The energy eigenvalues can be determined by $\Psi(0) = Ai(-\sigma/\rho) = 0$ due to the boundary condition $\Psi(0) = 0$ and are given by

$$E_i = a_i(tJ_z^2)^{1/3} = a_i \left(\frac{J_z}{t}\right)^{2/3} t, \tag{B.9}$$

where $a_1 = 2.33, a_2 = 4.09, a_3 = 5.52, a_4 = 6.79, \ldots$. This is the result found in the literature [54–56].

For us it is important to notice, that in the area $x < \sigma$ or $y < 0$ the solution is oscillatory, whereas for $y > 0$, there is an exponential decay $\sim 1/\sqrt{y}\exp(-2y^{3/2}/3)$. The typical lengthscale outside the classical area is given by $\rho^{3/2} = \left(\frac{t}{J_z}\right)^{1/2} \approx 1$. The classical turning point, that can be identified with the length of the string is $\sigma = \frac{a_i\left(\frac{J_z}{t}\right)^{2/3} t}{J_z} = a_i \left(\frac{t}{J}\right)^{1/3}$. The length of the shortest strings for $t \approx J$, as in our numerical simulations, is thus only about two to five lattice points.

# Appendix C

# Shadow bands from perturbation theory

In the following we will demonstrate, how the antibonding shadow band emerges from the bonding band by interaction with the spin background. We will closely follow the calculations by Kampf and Schrieffer [99], using the simplest possible assumptions for the spin susceptibility and the single-particle Green's function in the absence of interactions.

The Green's function of the bonding and antibonding bands emerging from the strong coupling limit are taken as the single particle propagators $G_0(\mathbf{k},\omega)$ in the problem, such that

$$G_0\big((k_x,k_y),\omega\big) = \begin{cases} G_b(k_x) & \text{if } k_y = 0 \\ G_a(k_x) & \text{if } k_y = \pi \end{cases} . \tag{C.1}$$

The pertubated system's Green's function is given by

$$G_1(\mathbf{k},\omega) = \Big[G_0^{-1}(\mathbf{k},\omega) - \Sigma_0(\mathbf{k},\omega)\Big]^{-1}, \tag{C.2}$$

with the self energy (see Fig. C.1)

$$\Sigma_0(\mathbf{k},\omega) = -i\alpha \int_{\mathbf{q}} \int_{\nu} d\mathbf{q} d\nu \chi(\mathbf{q},\nu) G_0(\mathbf{k}-\mathbf{q},\omega-\nu) \tag{C.3}$$

The parameter $\alpha$ is some (unknown) coupling constant in this context.

The susceptibility is taken to be peaked at the corners of the Brillouin zone $(\pi,\pi)$, were the spin gap is at its minimal value $\Delta$:

$$\chi(\omega,\mathbf{q}) = i\beta\delta\big(\omega-\Delta\big)\delta\big(\mathbf{q}-(\pi,\pi)\big). \tag{C.4}$$

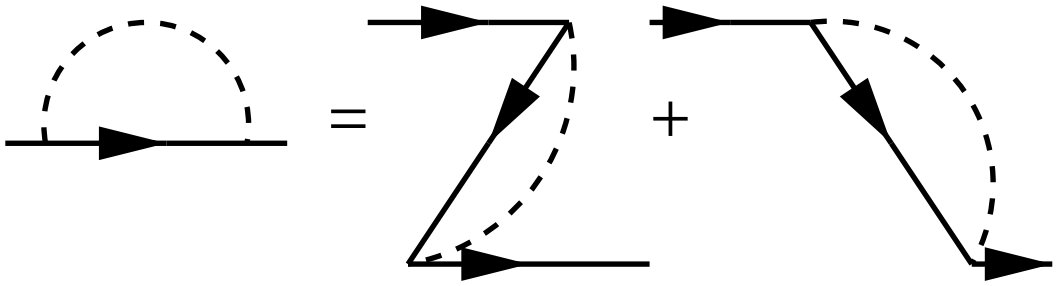

Figure C.1: First order contribution to the self-energy

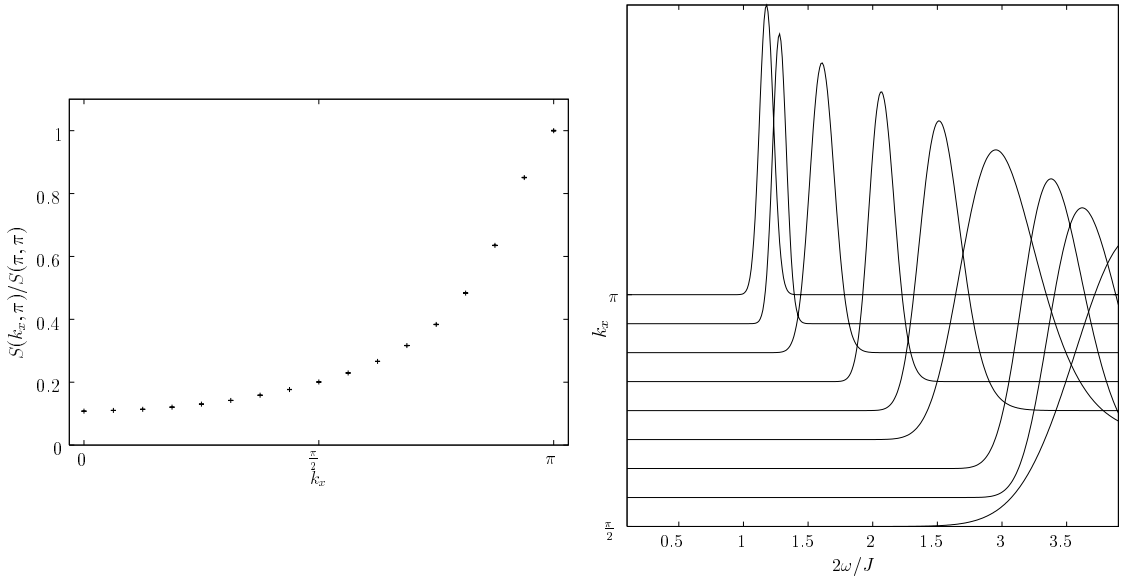


(a) Static structure factor $S\big(k_x,\pi\big)$

(b) Dynamic structure factor $S\big(k_x,\pi\big),\omega\big)/S\big((k_x,\pi)\big)$

Figure C.2: Dynamical spin structure factor $S(\mathbf{q},\omega)$ in a two-leg ladder and isotropic coupling. The dynamic structure factor has been normalized by the static one for clarity. The results were obtained by the *Maximum Entropy* method using the connection $NS(\mathbf{q},\tau) = \int_{-\infty}^{+\infty} \frac{e^{-\tau\omega}}{2\pi} S(\mathbf{q},\omega)$, where $N$ is the number of lattice points.

Again $\beta$ is some positive constant, with its exact value not relevant for this discussion. The choice of $\chi(\omega,\mathbf{q}) \sim \delta(\omega-\Delta)$ can be justified by our numerical results for the dynamical structure factor $S(\mathbf{q},\omega)$, that is peaked at this position (see Fig.C.2). From Fig. C.2.a one sees, that the static structure factor $S\big(k_x,\pi\big)$ is peaked in $\mathbf{k}$-space around $(\pi,\pi)$. The static structure factor for $(k_x,0)$ (not shown) is always much smaller than the one for $(k_x,\pi)$, and has its maximal value at $k_x=\pi$, where $S\big(k_x,0\big)/S\big(k_x,\pi\big) \approx 0.15$. The results we obtain are consistent with exact diagonalizations [131] on small lattices and analytical approaches [68,130]. At his point we notice, that the spin gap of $\Delta \approx 0.5J$

[57, 58, 117, 118, 124] is correctly reproduced.

In principle, the $\delta\big(\mathbf{q}-(\pi,\pi)\big)$-like excitation can only be justified for long-range antiferromagnetic ordering. This is not the case in the two-leg ladder, where we have some finite broadness, as can also be seen from our simulations, however, in view of the small width, the approximation can nevertheless be well justified.

For the self-energy we obtain finally

$$\begin{aligned}\Sigma_0(\mathbf{k},\omega) &= \alpha\beta \int\limits_{\mathbf{q}} \int\limits_{\nu} \delta(\nu-\Delta)\delta\big(\mathbf{q}-(\pi,\pi)\big) G_0\big((k_x-q_x,k_y-q_y),\omega-\nu\big) d\mathbf{q} d\nu \\ &= \alpha\beta G_0\big((k_x-\pi,k_y-\pi),\omega-\Delta\big). \end{aligned} \tag{C.5}$$

We now only consider the antibonding band, so we obtain

$$\begin{aligned} G_1\big((k_x,\pi),\omega\big) &= \Big[\omega-\epsilon_a(k_x)-\frac{\alpha\beta}{\omega-\Delta-\epsilon_b(\pi-k_x)+i\delta}\Big]^{-1} \\ &= \frac{\omega-\Delta-\epsilon_b(\pi-k_x)+i\delta}{\big(\omega-\epsilon_a(k_x)\big)\big(\omega-\Delta-\epsilon_b(\pi-k_x)+i\delta\big)-\alpha\beta}. \end{aligned} \tag{C.6}$$

The Green's function has two poles, that are located at

$$\begin{aligned} \omega_{1/2} &= \frac{\Delta+\epsilon_b(\pi-k_x)+\epsilon_a(k_x)}{2} \\ &\pm \frac{-\Delta-\epsilon_b(\pi-k_x)+\epsilon_a(k_x)}{2}\sqrt{1+\frac{4\alpha\beta}{\big[-\Delta-\epsilon_b(\pi-k_x)+\epsilon_a(k_x)\big]^2}} \\ &\approx \frac{\Delta+\epsilon_b(\pi-k_x)+\epsilon_a(k_x)}{2} \\ &\pm \frac{-\Delta-\epsilon_b(\pi-k_x)+\epsilon_a(k_x)}{2}\left[1+\frac{2\alpha\beta}{\big[-\Delta-\epsilon_b(\pi-k_x)+\epsilon_a(k_x)\big]^2}\right] \end{aligned} \tag{C.7}$$

In the last line, we assumed $\alpha\beta \ll \big[-\Delta-\epsilon_b(\pi-k_x)+\epsilon_a(k_x)\big]^2$ The first pole

$$\omega_1 = \epsilon_a(k_x)+\frac{\alpha\beta}{\epsilon_a(k_x)-\epsilon_b(\pi-k_x)-\Delta} \tag{C.8}$$

corresponds to the original antibonding band, that has been slightly shifted, whereas

$$\omega_2 = \epsilon_b(\pi-k_x)+\Delta-\frac{\alpha\beta}{\epsilon_a(k_x)-\epsilon_b(\pi-k_x)-\Delta} \tag{C.9}$$

corresponds to the shadow band. For $\alpha\beta/(\epsilon_a(k_x)-\epsilon_b(\pi-k_x)-\Delta) \to 0$ the shadow band is shifted exactly by the spin gap $\Delta$. When the effective coupling increases, the shadow band shifts to lower energies, as $\epsilon_a(k_x)-\epsilon_b(\pi-k_x)-\Delta > 0$, whereas the original antibonding band shifts to higher energies.

From eq.(C.6) it can further be seen, that the shadow band has vanishing weight as $\alpha\beta \to 0$. This is the result expected intuitively, as a vanishing of the susceptibility itself, or of the coupling between susceptibility and free Green's function leads to the vanishing of the related physical effect, namely the shadow band.

The same type of calculation can be done for the bonding band, just by exchanging the indices $a$ and $b$. One ends up with exactly the same results, only the energy shift due to the coupling $\alpha\beta$ is in the opposite direction.

# Appendix D

# The $\Delta\tau$-error in the three-leg ladder

The error due to the discretization of the imaginary time (*Trotter*-error, see eq.(2.2) on page 26), which was practically absent in one dimension, the two-leg ladder, and in two dimensions shows up in the three leg ladder. In the three-leg ladder, the translational symmetry along $y$-direction is broken, as we have open boundary conditions in that direction. In the following, we demonstrate the effects of this fact on the Green's functions given by

$$G(y_1 - y_2, k_x, \tau) = \sum_x \exp(ik_x x)\langle f_{(x,i)}(\tau) f^\dagger_{(0,j)}\rangle, \tag{D.1}$$

and the Green's functions corresponding to the three bands $G_l(k_x, \tau)$ (see eq.(6.5)). The Green's function $G(y_1 - y_2, k_x)$ are shown in Figs. D.1 and D.2 for $\Delta\tau t = 0.1$ and $\Delta\tau t = 0.01$ and no dynamics along the chain.

It can be immediately seen, that for $\Delta\tau t = 0.1$ Green's functions, which should be the same for symmetry reasons have different values in the simulations (especially $G(0-1,\tau)$, $G(2-1,\tau)$ and $G(1-0,\tau)$, $G(1-2,\tau)$). The problem seems to remain even for the very small value of $\Delta\tau t = 0.01$ for the symmetric pair $G(0-1,\tau)$ and $G(2-1,\tau)$. The resulting Green's functions $G_l(k_x)$ for the bands, which are the physically relevant ones, are shown in Fig. D.3. From the figure, we can see, that the $\Delta\tau$-error is not so drastic, when going to the relevant Green's functions. The bonding band, and the antibonding band seem to be unaffected by $\Delta\tau$ for the considered values, whereas for the antibonding one, the error can be reduced very much by taking into account all possible Green's functions, which can be derived from our simulations. This means, that we do not use the symmetries of

the system, but that we calculate all Green's functions[1].

A more realistic case can be seen in Fig. D.4, showing the Green's functions for a three-leg ladder with $L = 24$, $J = 1.2t$, $\beta t = 20$ , $\Delta\tau t = 0.025, 0.05$, and $\beta t = 40$, $\Delta\tau t = 0.05$. It can be seen very nicely, that the Green's functions lie on top of each other up to $4\tau t$, showing no sign of a $\Delta\tau$-error. Above $4\tau t$, $G_n\big((\pi/2, 0), \tau\big)$ for the system with small $\Delta\tau = 0.025$ deviates a little from the systems with $\Delta\tau = 0.05$. The physical results from these Green's function are nevertheless the same in the error bars. For the systems with $\Delta\tau t = 0.05$, the respective energy (slope of the Green's function) is $0.29t \pm 0.05t$,

[1]For example, we perform measurements both for $G(0-1,\tau)$ and $G(2-1,\tau)$, and use both Green's functions to calculated the physically relevant ones $G_a(\tau)$, $G_b(\tau)$ and $G_n(\tau)$.

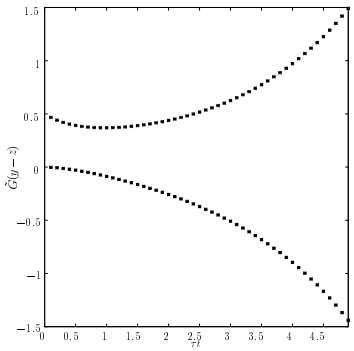

(a) $G(0-0,\tau)$, $G(2-2,\tau)$ and $G(2-0,\tau)$, $G(0-2,\tau)$ (lower curves)

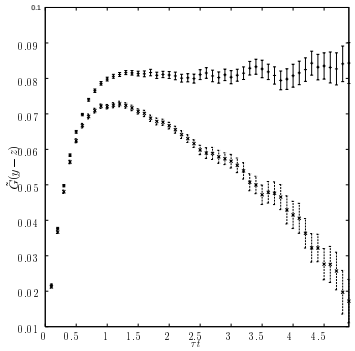

(b) $G(0-1,\tau)$, $G(2-1,\tau)$

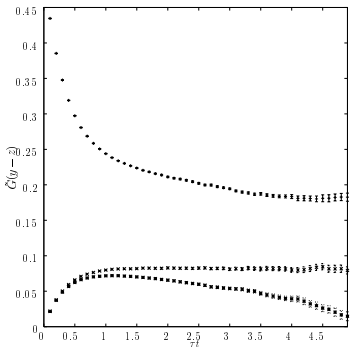

(c) $G(1-1,\tau)$ and $G(1-2,\tau)$, $G(1-0,\tau)$ (lower curves)

Figure D.1: $G(y-z,\tau)$ for all $y, z = 0, 1, 2$, $\Delta\tau t = 0.1$ and $J_y/t_y = 1, J_x = t_x = 0$

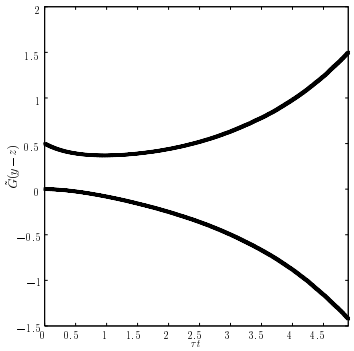

(a) $G(0-0)$, $G(2-2)$ and $G(2-0)$, $G(0-2)$ (lower curves)

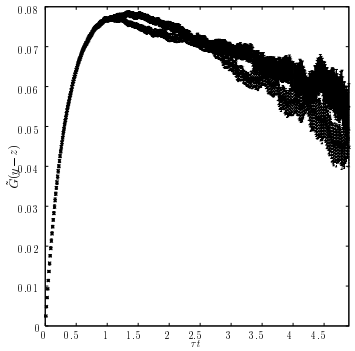

(b) $G(0-1)$, $G(2-1)$

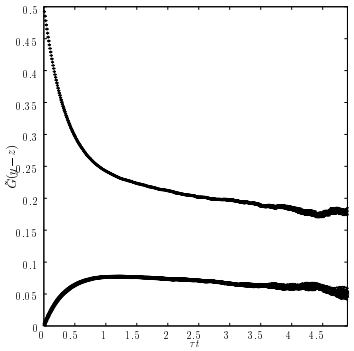

(c) $G(1-1)$ and $G(1-2)$, $G(1-0)$ (lower curves)

Figure D.2: $G(y-z)$ for all $y, z = 0, 1, 2$, $\Delta\tau t = 0.01$ and $J_y/t_y = 1, J_x = t_x = 0$

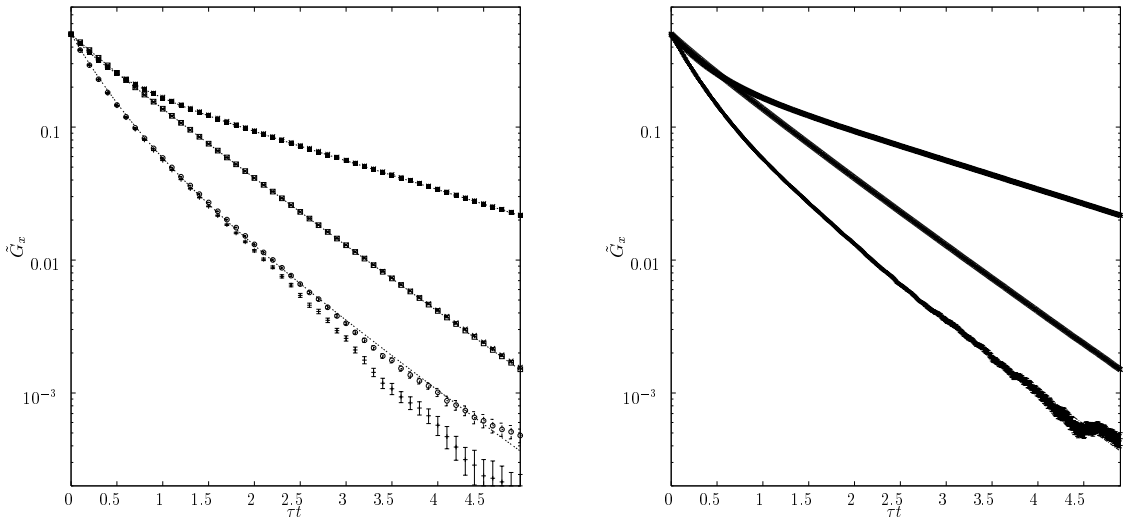


(a) $\Delta\tau t = 0.1$ (b) $\Delta\tau t = 0.01$

Figure D.3: Resulting $G_i$ ($G_n, G_b, G_a$ from to to bottom), where $i$ denotes the band for $\Delta\tau t = 0.1, 0.01$. For $\Delta\tau t = 0.1$ we show the results when all possible $G(y-z)$ are used to evaluate $G_i$ and the results, when analytically symmetric functions are replaced by a single $G(y-z)$ (see text).

the quasiparticle weight is $2 \times (0.18 \pm 0.02) = 0.36 \pm 0.04$, whereas for the system with $\Delta\tau t = 0.025$ these quantities are $0.24t \pm 0.05t$ and $0.33 \pm 0.04$. As an additional check, we calculate one Green's function at half the temperature of the two others, to demonstrate, that the system has already reached the ground state at $\beta t = 20$, $\beta J = 24$.

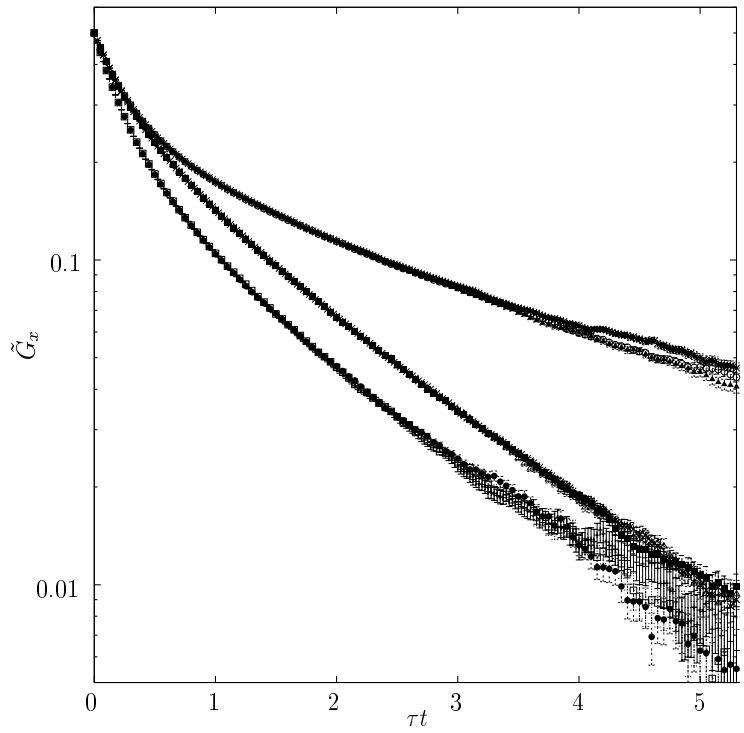


Figure D.4: Resulting $G_i$, where $i$ is $n$ (top curves), $b$ (middle curves) and $a$ (bottom curves). The system has $24 \times 3$ lattice points and $J/t = 1.2$. Two simulations were done at $\beta t = 20$, where $\Delta\tau t$ was set to 0.05 and 0.025 respectively. A third simulation was performed with $\beta t = 40$ and $\Delta\tau t = 0.05$. The results show, that for $\Delta\tau t = 0.05$ the $\Delta\tau$-error is in the statistical error bars, and that the inverse temperature of $\beta t = 20$ is sufficient to reach the ground state.

# Bibliography


[1] G. J. Bednorz and K. A. Müller, Z. Phys. B **64**, 188 (1986).

[2] J. Hubbard, Proc. R. Soc. London **A276**, 238 (1963).

[3] P. W. Anderson, Science **235**, 1196 (1987).

[4] J. E. Hirsch, Phys. Rev. Lett. **54**, 1317 (1985).

[5] D. J. Klein and W. A. Seitz, Phys. Rev. B **10**, 3217 (1974).

[6] W. Heisenberg, Z. Phys. **38**, 441 (1926).

[7] F. Zhang and T. M. Rice, Phys. Rev. B **37**, 3759 (1988).

[8] V. J. Emery, Phys. Rev. Lett. **58**, 2794 (1987).

[9] M. Grioni and J. Voit (unpublished).

[10] S. D. Kevan, *Angle-resolved Photoemission - Theory and current application* (Elsevier, Amsterdam, 1992).

[11] C. Kim *et al.*, Phys. Rev. Lett **77**, 4054 (1996).

[12] C. Kim *et al.*, Phys. Rev. Lett. **80**, 4245 (1998).

[13] T. Takahashi *et al.*, Phy. Rev. B **56**, 7870 (1997).

[14] B. O. Wells *et al.*, Phys. Rev. Lett. **74**, 964 (1995).

[15] S. LaRosa *et al.*, Phys. Rev. B **56**, R525 (1997).

[16] E. H. Lieb and F. Y. Wu, Phys. Rev. Lett. **20**, 1445 (1968).

[17] Z. N. C. Ha and F. D. M. Haldane, Phys. Rev. Lett **73**, 2887 (1994).

[18] F. F. Assaad and D. Würtz, Phys. Rev. B **50**, 136 (1991).

[19] F. F. Assaad, Ph.D. thesis, ETH Zürich, 1991.

[20] M. Brunner, *Quanten-Monte-Carlo-Simulationen des t-J-Modells* (Diplomarbeit, Universität Augsburg, Augsburg, 1996).

[21] B. Ammon *et al.*, Phys. Rev. B **58**, 4304 (1998).

[22] M. Brunner and A. Muramatsu, Phys. Rev. B **16**, R10100 (1998).

[23] W. von der Linden, Phys. Rep. **220**, 53 (1992).

[24] E. Y. Loh *et al.*, Phys. Rev. B **41**, 9301 (1990).

[25] R. N. Silver, D. S. Sivia, and J. E. Gubernatis, Phys. Rev. B **41**, 2380 (1990).

[26] E. T. Jaynes, in *The Maximum entropy Formalism*, edited by R. D. Levine and M. Tribus (MIT Press, Cambridge, 1978).

[27] M. Jarrell and J. Gubernatis, Phys. Rep. **269**, 133 (1996).

[28] F. F. Assaad and M. Imada, Eur. Phys. J. B **10**, 595 (1999).

[29] A. Muramatsu, in *Quantum Monte Carlo Methods in Physics and Chemistry*, edited by M. P. Nightingale and C. J. Umrigar (Kluwer Academic Press, Dordrecht, 1999).

[30] N. Bulut, D. J. Scalapino, and S. R. White, Phys. Rev. Lett. **73**, 748 (1994).

[31] R. Preuss, W. Hanke, and W. von der Linden, Phys. Rev. Lett **75**, 1344 (1995).

[32] E. Dagotto, Rev. Mod. Phys. **66**, 763 (1994).

[33] M. Boninsegni, Phys. Lett. A **188**, 330 (1994).

[34] H. G. Evertz, M. Marcu, and G. Lana, Phys. Rev. Lett **70**, 875 (1993).

[35] N. Kawashima, J. E. Gubernatis, and H. G. Evertz, Phys. Rev. B **50**, 136 (1994).

[36] M. Troyer and M. Imada, in *Computer Simulations in Condensed Matter Physics*, edited by D. Landau (Springer, Heidelberg, 1997), Vol. 10, p. 137.

[37] M. Troyer and S. Sachdev, Phys. Rev. Lett. **81**, 5418 (1998).

[38] G. Khaliullin, JETP Lett. **52**, 389 (1990).

[39] A. Angelucci, Phys. Rev. B **51**, 11580 (1995).

[40] G. Baskaran and P. W. Anderson, Phys. Rev B **37**, 580 (1988).

[41] H. Suzuura and N. Nagaosa, Phys. Rev. B **56**, 3548 (1997).

[42] J. Voit, Condens. Mat. **8**, L 779 (1996).

[43] J. Voit, Eur. Phys. J. B. **5**, 505 (1998).

[44] S. Sorella and A. Parola, Phys. Rev. Lett. **76**, 4604 (1996).

[45] M. Brunner, F. F. Assaad, and A. Muramatsu, cond-mat/9904150 (unpublished).

[46] K. von Szczepanski, P. Horsch, W. Stephan, and M.Ziegler, Phys. Rev. B **41**, 2017 (1990).

[47] E. Dagotto, R. Joynt, S. Bacci, and E. Gagliano, Phy. Rev B **41**, 9049 (1990).

[48] D. Poilblanc, H. Schulz, and T. Ziman, Phys. Rev. B **47**, 3268 (1993).

[49] P. Béran, D. Poilblanc, and R. B. Laughlin, Nuc. Phys. B **473**, 707 (1996).

[50] M. Boninsegni and E. Manousakis, Phys. Rev. B **45**, 4877 (1992).

[51] C. J. Hamer, Z. Weihong, and J. Otimaa, Phys. Rev. B **58**, 15508 (1998).

[52] G. Martinez and P. Horsch, Phys. Rev. B **44**, 317 (1991).

[53] Z. Liu and E. Manousakis, Phys. Rev. B **45**, 2425 (1992).

[54] L. N. Bulaevskii, E. L. Nagaev, and D. I. Khomskii, JETP **27**, 836 (1968).

[55] C. L. Kane, P. A. Lee, and N. Read, Phys. Rev. B **39**, 6880 (1989).

[56] B. Shraiman and E. Siggia, Phys. Rev. Lett. **60**, 740 (1988).

[57] E. Dagotto and T. M. Rice, Science **271**, 618 (1996).

[58] T. M. Rice, Z. Phys. B **103**, 165 (1997).

[59] E. Dagotto, cond-mat/9908250 (unpublished).

[60] A. V. Chubukov, Pis'ma Zh. Éksp. Teor. Fiz. **49**, 108 (1989), JETP Lett. 49, 129 (1989).

[61] S. Sachdev and R. Bhatt, Phys. Rev. B **41**, 9323 (1990).

[62] S. Gopalan, T. M. Rice, and M. Sigrist, Phys. Rev. B **49**, 8901 (1994).

[63] H. Endres *et al.*, Phys. Rev. B **53**, 5530 (1996).

[64] O. P. Sushkov, Phys. Rev. B **60**, 3289 (1999).

[65] J. Otimaa, C. J. Hamer, and Z. Weihong, cond-mat/9909280 (unpublished).

[66] M. Y. Kagan, S. Haas, and T. Rice, Physica C **318**, 185 (1999).

[67] T. M. Rice, S. Haas, and M. Sigrist, Phy. Rev. B **56**, 14655 (1997).

[68] O. P. Sushkov and V. N. Kotov, Phys. Rev. Lett. **81**, 1941 (1998).

[69] S. R. White and D. J. Scalapino, Phys. Rev. Lett. **69**, 2863 (1992).

[70] J. W. Negele and H. Orland, *Quantum many-particle sytems*, *Frontiers in Physics* (Addison-Wesley Publishing Company, Redwood City, 1988).

[71] H. F. Trotter, Proc. Am. Math. Soc. **10**, 545 (1959).

[72] R. Swendsen and J.-S. Wang, Phy. Rev. Lett. **58**, 86 (1987).

[73] M. Brunner and A. Muramatsu, *High Performance Computing in Science and Engineering'98* (Springer-Verlag, Berlin, 1999).

[74] B. B. Beard and U.-J. Wiese, Phy. Rev. Lett. **77**, 1087 (1996).

[75] C. Lavalle, M. Brunner, and A. Muramatsu (unpublished).

[76] R. M. Fye, Phys. Rev. B. **33**, 6271 (1986).

[77] N. V. Prokof'ev, B. V. Svistunov, and I. S. Tupitsyn, JETP **87**, 310 (1998).

[78] R. Brower, S. Chandrasekharan, and U.-J. Wiese, Physica A **3-4**, 520 (1998).

[79] W. von der Linden, Applied Physics A **60**, 155 (1995).

[80] C. H. Mak and D. Chandler, Phys. Rev. A **44**, 2352 (1991).

[81] R. Egger and C. H. Mak, Phys. Rev. B **50**, 15210 (1994).

[82] M. Winterstetter and U. Weiss, Chem. Phys. **209**, 455 (1996).

[83] A. Papoulis, *Probability and Statistics* (Prentice-Hall, Englewood Cliff, 1990).

[84] F. D. M. Haldane, J. Phys. C **14**, 2585 (1981).

[85] J. Voit, Rep. Prog. Phys. **58**, 977 (1995).

[86] V. Meden and K. Schönhammer, Phys. Rev. B **46**, 15753 (1992).

[87] K. Schönhammer and V. Meden, Phys. Rev. B **47**, 16205 (1993).

[88] S. Sorella and A. Parola, J. Phys. Condens. Matter **4**, 3589 (1992).

[89] A. Parola and S. Sorella, Phys. Rev. B **45**, 13156 (1992).

[90] K. Penc, K. Hallberg, F. Mila, and H. Shiba, Phys. Rev. Lett **77**, 1390 (1996).

[91] Z. Y. Weng, D. N. Sheng, and C. S. Ting, Phys. Rev B **52**, 637 (1995).

[92] P.-A. Bares and G. Blatter, Phys. Rev. Lett. **64**, 2567 (1990).

[93] Y. Kato, Phys. Rev. Lett **81**, 5402 (1998).

[94] F. D. M. Haldane, in *Correlation Effects in Low-Dimensional Electron Systems*, edited by A. Okiji and N. Kawakami (Springer Verlag, Berlin, 1994).

[95] W. F. Brinkman and T. M. Rice, Phys. Rev. B **2**, 1324 (1970).

[96] J. R. Schrieffer, X. G. Wen, and S. C. Zhand, Phys. Rev. B **39**, 11663 (1989).

[97] S. Sachdev, Phys. Rev. B **39**, 12232 (1989).

[98] R. Eder and K. W. Becker, Z. Phys. B **78**, 219 (1990).

[99] A. P. Kampf and J. R. Schrieffer, Phys. Rev. B **42**, 7967 (1990).

[100] R. B. Laughlin, Phys. Rev. Lett. **79**, 1726 (1997).

[101] A. V. Chubukov and D. K. Mork, Phys. Rev. B **57**, 5298 (1998).

[102] Z. Y. Weng, D. N. Sheng, and C. S. Ting, cond-mat/9908032 (unpublished).

[103] M. Boninsegni and E. Manousakis, Phys. Rev. B **46**, 560 (1992).

[104] P. W. Leung and R. J. Gooding, Phys. Rev. B **52**, 15711 (1995).

[105] J. Jaklic and P. Prevlosek, Phys. Rev B **55**, R7307 (1997).

[106] J. Jaklic and P. Prevlosek, Advances in Physics **49**, 1 (2000).

[107] F. Ronning *et al.*, Science **282**, 2067 (1998).

[108] S. A. Trugman, Phys. Rev. B **35**, 1597 (1988).

[109] V. Elser, D. Huse, B. Shraiman, and E. Siggia, Phys. Rev. B **41**, 6715 (1990).

[110] R. T. Scalettar, in *Quantum Monte Carlo Methods in Physics and Chemistry*, edited by M. P. Nightingale and C. J. Umrigar (Kluwer Academic Press, Dordrecht, 1999).

[111] M. Calandra, F. Becca, and S. Sorella, Phys. Rev. Lett. **81**, 5185 (1998).

[112] C. S. Hellberg and E. Manousakis, Phys. Rev. Lett. **78**, 4609 (1997).

[113] Q. F. Zhong and S. Sorella, Europhys. Lett. **21**, 629 (1993).

[114] L. Balents and M. P. A. Fisher, Phys. Rev. B **53**, 12133 (1996).

[115] D. Poilblanc, D. J. Scalapino, and W. Hanke, Phys. Rev. B **52**, 6796 (1995).

[116] T. F. A. Müller and T. M. Rice, Phys. Rev. B **58**, 3425 (1998).

[117] E. Dagotto, J. Riera, and D. J. Scalapino, Phys. Rev. B **45**, 5744 (1992).

[118] T. Barnes, E. Dagotto, and E. S. Swanson, Phys. Rev. B **47**, 3196 (1993).

[119] P. W. Anderson, Res. Bull. **8**, 153 (1973).

[120] R. Eder, Phys. Rev. B **57**, 12823 (1998).

[121] Z. Hiroi, M. Azuma, and Y.Bando, J. Solid State Chem. **95**, 230 (1991).

[122] M. Azuma *et al.*, Phys. Rev. Lett. **73**, 3463 (1994).

[123] T. Barnes and J. Riera, Phys. Rev. B **50**, 6817 (1994).

[124] S. R. White, R. M. Noack, and D. J. Scalapino, Phys. Rev. Lett. **73**, 886 (1994).

[125] J. Otimaa, R. R. Singh, and Z. Weihong, Phys. Rev. B **54**, 1009 (1996).

[126] V. N. Kotov, O. Kotov, and R. Eder, Phys. Rev. B **59**, 6266 (1999).

[127] A. W. Sandvik, cond-mat/9904218 (unpublished).

[128] J. Riera, D. Poilblanc, and E. Dagotto, Eur. Phy. J. B **7**, 53 (1999).

[129] G. B. Martins, C. Gazza, and E. Dagotto, Phys. Rev. B **59**, 13596 (1999).

[130] K. Damle and S. Sachdev, Phys. Rev. B **57**, 8307 (1998).

[131] M. Troyer, H. Tsunetsugu, and T. M. Rice, Phy. Rev. B **53**, 251 (1996).

[132] S. Haas and E. Dagotto, Phys. Rev. B **54**, R3718 (1996).

[133] K. Kojima *et al.*, Phys. Rev. Lett. **74**, 2812 (1995).

[134] N. D. Mermin and H. Wagner, Phys. Rev. Lett. **17**, 1133 (1966).

[135] B. Frischmuth, B. Ammon, and M. Troyer, Phys. Rev. B **54**, R3714 (1996).

[136] S. R. White and D. Scalapino, Phys. Rev. B **57**, 3031 (1998).

[137] S. Sorella, Phys. Rev. B **53**, 15119 (1996).

[138] R. W. Robinett, *Quantum Mechanics*, 1 ed. (Oxford University Press, New York, 1997).

[139] F. Gebhard, *The Mott metal-insulator transition: models and methods*, *Springer tracts in modern physics* (Springer Verlag, Berlin, 1997).

[140] I. S. Gradshteyn and I. M. Ryzhik, in *Table of Integrals, Series, and Products*, 5 ed., edited by A. Jeffrey (Academic Press, San Diego, 1965).

# Danksagung

An dieser Stelle möchte ich mich bei allen, die am Entstehen dieser Arbeit beteiligt waren herzlich bedanken.

Zunächst danke ich Herrn Prof. Dr. Alejandro Muramatsu für sein stetes Interesse am Fortgang dieser Arbeit und die vielen hilfreichen Diskussionen und Anregungen, die ein Gelingen erst möglich gemacht haben.
Weiter danke ich Herrn Prof. Dr. Ulrich Weiss für die freundliche Übernahme des Mitberichts.

Herrn Prof. Dr. Max Wagner danke ich für die freundlich Aufnahme an seinem Institut und Frau I. Poljak für ihre Freundlichkeit und Unterstützung im Papierkrieg.

Weiter danke ich Herrn Priv.-Doz. Dr. F.F. Assaad, dessen Wissen und Können, neben seinen Programmen, viel zu dieser Arbeit beigetragen haben, und den anderen Mitgliedern des Instituts, die stets für ein angenehmes Arbeitsklima sorgten.

Zum Schluss möchte ich mich bei meiner Familie und besonders bei meiner Frau Barbara bedanken.

# Curriculum Vitae

| | |
|---|---|
| Surname: | Brunner |
| First name: | Michael |
| Nationality: | German |
| Date of birth: | February 3$^{\text{rd}}$, 1972 |
| Place of birth: | Würzburg, Germany |
| Marital status: | married with Barbara Brunner |
| Military service: | Exemption from military service due to service at the *Bayerisches Rotes Kreuz* from 1991-1998 |

| | |
|---|---|
| 1978-1982: | Primary school: Grundschule *Auf der Schanz*, Ingolstadt |
| 1982-1991: | Secondary school: *Christoph-Scheiner-Gymnasium*, Ingolstadt and *Descartes-Gymnasium*, Neuburg an der Donau |
| 1991-1996: | University: Diploma at Universität Augsburg.<br>Diploma work: "Quanten-Monte-Carlo-Simulationen des $t$-$J$-Modells".<br>Supervisors: Prof. A.Muramatsu and Priv. Doz. K.-H. Höck |
| 1996-1999 | PhD work at Universität Stuttgart:<br>"Single hole dynamics in the $t$-$J$ model".<br>Supervisors: Prof. A.Muramatsu and Prof. U. Weiss |